Evaluation of Biopolymer Treatment Effects on Overtopping Erosion and Breach Development in Earthen Embankments Using Numerical Models

by

Brock Martin Huner

A thesis submitted to the Graduate Faculty of
Auburn University
in partial fulfillment of the
requirements for the Degree of
Master of Science

Auburn, Alabama
August 8, 2026

Keywords: headcut, parameters, sensitivity, progression, simulations

Approved by

Jack Montgomery, Ph.D., P.E., Chair, Alice H. and John M. Ozier Associate Professor
J. Brian Anderson, Ph.D., P.E., Elton Z. and Lois G. Huff Professor
Ali Khosravi, Ph.D., P.E., Assistant Professor

Abstract

This study evaluated the ability of existing overtopping breach models to represent the effects of biopolymer treatment on earthen embankment erosion and breach development. Two full-scale experimental datasets were used: the Kang et al. (2021) overtopping test and the ERDC Breland et al. experiment. The behavior of treated and untreated embankments was simulated using WinDAM C and DLBreach. The study compared predicted breach initiation, headcut migration, breach widening, and hydraulic control behavior with observed responses. Models were found to be generally more successful at reproducing the final breach width than at reproducing the full erosion history. Biopolymer treatment consistently improved erosion resistance by delaying initiation and slowing breach progression, but this effect was only partially represented in the models through calibrated parameter adjustments. A Dakota sensitivity analysis showed that the dominant controlling parameter varied by model: AC governing the WinDAM C energy model, k_d governing the WinDAM C stress model, and Manning's n most strongly influencing DLBreach. Pearson and Spearman results generally agreed and showed both linear and nonlinear parameter relationships. Overall, the results indicate that current breach models can approximate some end-state behavior of biopolymer-treated embankments, but they remain limited in their ability to represent the full sequence of overtopping failure, especially headcut migration.

Artificial Intelligence (AI) Use Disclosure Statement

In preparing this thesis, the following Artificial Intelligence (AI) tools were used: Perplexity AI and Grammarly. These tools were used primarily to check grammar and spelling throughout this thesis. The author acknowledges full responsibility for the intellectual content of this work and has ensured that all AI-assisted sections have been reviewed and revised for accuracy and appropriate academic style. All AI-generated content was reviewed and validated for relevance, appropriateness, and accuracy before incorporation into the final document to maintain the scholarly integrity of this research.

Digital Accessibility Use Disclosure Statement

In the preparation of this thesis, the following digital accessibility tools were used to ensure this document complies with federal requirements: Microsoft Word Accessibility Assistant. The author acknowledges full responsibility for the intellectual content of this work and has made a good faith effort to comply with digital accessibility requirements in publishing, wherein the nature of the content does not significantly change in order to do so. Furthermore, all content has been reviewed and revised to meet these requirements prior to final publication.

Acknowledgments

First and foremost, I give all glory and honor to God, my ultimate Provider and Sustainer. His grace has allowed me the opportunity to study at Auburn University, to grow in knowledge, and to be surrounded by such excellent faculty, staff, and fellow students. Anything I have accomplished in this work is only because He has allowed it.

I would like to express my deepest gratitude to my advisor, Dr. Jack Montgomery, for his unwavering support, guidance, and patience throughout this process. He has challenged me to be the best engineer I can be and has invested in my growth both technically and professionally. The lessons he has taught me are ones I will carry with me throughout my career as an engineer.

I am profoundly thankful for my wife, Mae Mae, whose constant encouragement, understanding, and love have carried me through the many long days and late nights of graduate school. I am equally grateful to my family – my Mom, Dad, Pop, Nan, my sister Hannah, and my brother Brady – for their steadfast support, love, and prayer. Their belief in me, from childhood to this moment, has been a foundational blessing in my life. They have sacrificed and supported me so that I could pursue my true dream, and I will always be indebted to them for that.

I also want to lovingly acknowledge the memory of my grandmother, Gan Gan, and my Uncle Jeff, who both passed away during my time in graduate school but remain very present in my heart. Uncle Jeff, an Auburn graduate himself, played a significant role in helping me through my undergraduate studies and was one of the most intelligent people I have ever known. Their influence, love, and example have helped guide me from a young boy to the man I am today.

I am sincerely grateful to the United States Army Corps of Engineers for funding this master’s program and providing the financial support that made this work possible. Their investment in my education and in this research has been a tremendous blessing and privilege.

Above all, I thank the Lord for ordering my steps, for surrounding me with people who care deeply about me, and for reminding me that His purposes are greater than any academic, professional, or personal achievement.

Table of Contents

Abstract 2
Artificial Intelligence (AI) Use Disclosure Statement 3
Digital Accessibility Use Disclosure Statement 4
Acknowledgments 5
Table of Contents 7
List of Tables 9
List of Figures 10
List of Abbreviations 18
CHAPTER 1: Introduction 20
1.1 Background 20
1.2 Objectives 22
1.3 Scope of Work 24
1.4 Organization of Thesis 24
CHAPTER 2 25
Background and Literature Review 25
2.1 Overtopping Failure of Earthen Embankments 25
2.2 Erosion Mechanics of Cohesive Soils 30
2.3 Effects of Biopolymer Treatment on Erosion Resistance 35
2.4 Modeling Headcut Progression Due to Overtopping of Earthen Embankments 39
2.5 Sensitivity Studies 42
2.6 Summary 46
CHAPTER 3: Research Methods 48
3.1 Modeling Approaches 48
3.2 Kang et al. (2021) Experiment 62
3.3 Breland et al. (2025) Experiment 66
3.4 Summary 78
CHAPTER 4 80
Results 80
4.1 Kang et al. (2021) Experiment Results 81
4.2 Breland et al. (2025) – Blind Prediction 90
4.4 Breland et al. (2025) – Breach Experiment 110
4.5 Breland et al. (2025) – Combined Overtopping-plus-Breach Simulations 123

4.6 Breland et al. (2025) – Simulated Breach Progression Comparison 145
4.7 Sensitivity Analysis Using Dakota 147
4.8 Summary 151
CHAPTER 5: Discussion 153
5.1 Parameter Selection and Calibration 153
5.2 Simulation Results 154
5.3 Sensitivity Analysis 156
5.4 Implications for Biopolymer-Treated Embankments 157
CHAPTER 6 159
Conclusions and Recommendations 159
6.1 Summary 159
6.2 Conclusions 161
6.3 Recommendations for Future Work 163
REFERENCES 164
APPENDIX 186

List of Tables

Table 1. Table of input parameters, including symbol, source program, modeled quantity or function, and units. 55
Table 2: Retardance classes of various vegetal covers and their corresponding retardance curve index values (USDA 2021). 57
Table 3: Stem densities of tested grass types along with their associated vegetal cover factors (USDA 2021). 58
Table 4. Table of interested output parameters for this study, including which program, the definition, and the units. 62
Table 5: Key Model Parameter Values for Untreated Correlation Simulation. 65
Table 6: Lab-observed vegetation and soil input parameters for WinDAM C and DLBreach (untreated vs. treated). 70
Table 7. Correlated vegetation and soil input parameters for WinDAM C and DLBreach (untreated vs. treated). 71
Table 8. Best-fit vegetation and soil parameters for WinDAM C: untreated vs. treated (overtopping-plus-breach experiment). 71
Table 9. Parameter ranges used in the WinDAM-C Energy Model, WinDAM-C Stress Model, and DLBreach simulations. 76
Table 10. Linear correlation matrix between each model's input parameters and output response, with positive values indicating a direct relationship and negative values indicating an inverse relationship. 148
Table 11. Non-linear correlation matrix between each model's input parameters and output response, with positive values indicating a direct relationship and negative values indicating an inverse relationship. 149

List of Figures

Figure 1. Different stages of headcut progression from physical models of breaching: (left) longitudinal profile view adapted from Hanson et al. (2005) and (right) cross-sectional elevation view adapted from Zhou et al. (2019). 27
Figure 2. (a) Post-overtopping condition of the downstream spillway at Y16 Dam, Georgia, illustrating complete loss of surface cover but preservation of embankment integrity due to RCC armoring (Hansen and Fitzgerald 2016). (b) Placement of articulated concrete block mats over geotextile on the downstream slope of Strahl Lake Dam, Indiana (photo by Contech Construction Products, Inc.). (c) Downstream slope of Dam Svartevatn, Norway, protected by interlocking placed riprap (Hiller 2017). (d) Earth dam with well-established vegetative cover on the downstream slope (García-Asensio and Ayuga 2017). . 29
Figure 3. Changes in erosion resistance of (a) soft marine clay (data from Kwon et al. 2020) and (b) kaolinite (data from Kwon et al. 2023a) with increasing amounts of treatment with XG as measured with an EFA. 36
Figure 4. Representative JET results from Walshire et al. (2024) showing the critical shear stress and erodibility coefficient of Vicksburg Silt, and the modification of these parameters under a 1% biopolymer treatment. 37
Figure 5. Unconfined compressive strengths of biopolymer-treated silt as a function of biopolymer concentration (a), and corresponding failure envelopes of sand at 2% biopolymer concentration (b), both after 5 weeks of curing, as reported by Ayeldeen et al. (2016). 38
Figure 6. WinDAM C simulation illustrates the temporal progression of headcut migration and breach widening at matched time intervals for the embankment overtopping scenario. 51
Figure 7. Simultaneous progression of headcut migration and breach widening during overtopping as modeled by DLBreach (Wu 2016). 53
Figure 8. Embankment cross sections for the two embankments (after Kang et al. 2021). 63
Figure 9. Overtopping performance of the treated and untreated embankments (after Kang et al. 2021). 64
Figure 10. Post-overtopping condition of the embankment, illustrating the treated (a) and untreated (b) sections. 67
Figure 11. Observed headcut migration (a), lateral expansion, and deepening (b) with duration of overtopping for treated and untreated plots during the breach experiment (Breland et al. 2025). 68
Figure 12. Water surface elevation versus time during the overtopping experiment (Breland et al. 2025). 72
Figure 13. Water surface elevation versus time during the full breach experiment (Breland et al. 2025). 73
Figure 14. Water surface elevation versus time during combined overtopping and full breach experiments (Breland et al. 2025). 74

Figure 15. Simulation results from the WinDAM C energy-based model for the untreated embankment using parameter values derived from empirical correlations. 82
Figure 16. Simulation results from the WinDAM C stress-based model for the untreated embankment using (a) parameter values derived from empirical correlations and (b) best-fit parameter values obtained via calibration. 83
Figure 17. Simulation results from DLBreach for the untreated embankment using (a) parameter values derived from empirical correlations and (b) best-fit parameter values obtained via calibration. 84
Figure 18. Simulation results from the WinDAM C energy-based model for the treated embankment using (a) parameter values derived from empirical correlations and (b) best-fit parameter values obtained via calibration. 85
Figure 19. Simulation results from the WinDAM C stress-based model for the treated embankment using (a) parameter values derived from empirical correlations and (b) best-fit parameter values obtained via calibration. 86
Figure 20. Simulation results from DLBreach for the treated embankment using (a) parameter values derived from empirical correlations and (b) best-fit parameter values obtained via calibration. 87
Figure 21. Evolution of headcut progression obtained from simulation for (a) untreated and (b) treated embankment cases. 88
Figure 22. Evolution of breach widening progression obtained from simulation for (a) untreated and (b) treated embankment cases. 89
Figure 23. Evolution of breach deepening obtained from simulation for (a) untreated and (b) treated embankment cases. 90
Figure 24. Comparison of blind-predicted upstream water surface elevations from WinDAM C energy model simulations using (a) lab-observed and (b) correlated input parameter sets for the untreated embankment against ERDC (2025) experimental measurements. 91
Figure 25. Comparison of blind-predicted headcut progression from WinDAM C energy model simulations using (a) lab-observed and (b) correlated input parameter sets for the untreated embankment against Breland et al. (2025) breach experiment measurements. 91
Figure 26. Comparison of blind-predicted breach widening progression from WinDAM C energy model simulations using (a) lab-observed and (b) correlated input parameter sets for the untreated embankment against Breland et al. (2025) breach experiment measurements. 92
Figure 27. Comparison of blind-predicted hydraulic control progression from WinDAM C energy model simulations using (a) lab-observed and (b) correlated input parameter sets for the untreated embankment against Breland et al. (2025) breach experiment measurements. 92
Figure 28. Comparison of blind-predicted upstream water surface elevations from WinDAM C stress model simulations using (a) lab-observed and (b) correlated input parameter sets for the untreated embankment against ERDC (2025) experimental measurements. 93
Figure 29. Comparison of blind-predicted headcut progression from WinDAM C stress model simulations using (a) lab-observed and (b) correlated input parameter sets

for the untreated embankment against Breland et al. (2025) breach experiment measurements. 94
Figure 30. Comparison of blind-predicted breach widening progression from WinDAM C stress model simulations using (a) lab-observed and (b) correlated input parameter sets for the untreated embankment against Breland et al. (2025) breach experiment measurements. 94
Figure 31. Comparison of blind-predicted hydraulic control progression from WinDAM C stress model simulations using (a) lab-observed and (b) correlated input parameter sets for the untreated embankment against Breland et al. (2025) breach experiment measurements. 95
Figure 32. Comparison of blind-predicted upstream water surface elevations from DLBreach simulations using (a) lab-observed and (b) correlated input parameter sets for the untreated embankment against ERDC (2025) experimental measurements. 96
Figure 33. Comparison of blind-predicted headcut progression from DLBreach simulations using (a) lab-observed and (b) correlated input parameter sets for the untreated embankment against Breland et al. (2025) breach experiment measurements. 96
Figure 34. Comparison of blind-predicted breach widening progression from DLBreach simulations using (a) lab-observed and (b) correlated input parameter sets for the untreated embankment against Breland et al. (2025) breach experiment measurements. 97
Figure 35. Comparison of blind-predicted hydraulic control progression from DLBreach simulations using (a) lab-observed and (b) correlated input parameter sets for the untreated embankment against Breland et al. (2025) breach experiment measurements. 97
Figure 36. Sensitivity analysis results showing the impact of the RCI on breach initiation timing for untreated Breland et al. (2025) WinDAM C stress simulations (blind prediction), highlighting how variations in RCI affect the onset of embankment erosion. 100
Figure 37. Sensitivity analysis results showing the impact of VCF on breach initiation timing for untreated Breland et al. (2025) WinDAM C stress simulations (blind prediction), highlighting how variations in VCF affect the onset of embankment erosion. 102
Figure 38. Comparison of blind-predicted upstream water surface elevations from WinDAM C energy model simulations using (a) lab-observed and (b) correlated input parameter sets for the treated embankment against ERDC (2025) experimental measurements. 103
Figure 39. Comparison of blind-predicted headcut progression from WinDAM C energy model simulations using (a) lab-observed and (b) correlated input parameter sets for the treated embankment against Breland et al. (2025) breach experiment measurements. 104
Figure 40. Comparison of blind-predicted breach widening progression from WinDAM C energy model simulations using (a) lab-observed and (b) correlated input parameter sets for the treated embankment against Breland et al. (2025) breach experiment measurements. 104

Figure 41. Comparison of blind-predicted hydraulic control progression from WinDAM C energy model simulations using (a) lab-observed and (b) correlated input parameter sets for the treated embankment against Breland et al. (2025) breach experiment measurements. 105
Figure 42. Comparison of blind-predicted upstream water surface elevations from WinDAM C stress model simulations using (a) lab-observed and (b) correlated input parameter sets for the treated embankment against ERDC (2025) experimental measurements. 106
Figure 43. Comparison of blind-predicted headcut progression from WinDAM C stress model simulations using (a) lab-observed and (b) correlated input parameter sets for the treated embankment against Breland et al. (2025) breach experiment measurements. 106
Figure 44. Comparison of blind-predicted breach widening progression from WinDAM C stress model simulations using (a) lab-observed and (b) correlated input parameter sets for the treated embankment against Breland et al. (2025) breach experiment measurements. 107
Figure 45. Comparison of blind-predicted hydraulic control progression from WinDAM C stress model simulations using (a) lab-observed and (b) correlated input parameter sets for the treated embankment against Breland et al. (2025) breach experiment measurements. 107
Figure 46. Comparison of blind-predicted upstream water surface elevations from DLBreach model simulations using (a) lab-observed and (b) correlated input parameter sets for the treated embankment against ERDC (2025) experimental measurements. 108
Figure 47. Comparison of blind-predicted headcut progression from DLBreach model simulations using (a) lab-observed and (b) correlated input parameter sets for the treated embankment against Breland et al. (2025) breach experiment measurements. 108
Figure 48. Comparison of blind-predicted breach widening progression from DLBreach model simulations using (a) lab-observed and (b) correlated input parameter sets for the treated embankment against Breland et al. (2025) breach experiment measurements. 109
Figure 49. Comparison of blind-predicted hydraulic control progression from DLBreach model simulations using (a) lab-observed and (b) correlated input parameter sets for the treated embankment against Breland et al. (2025) breach experiment measurements. 109
Figure 50. Comparison of breach experiment headcut progression from WinDAM C energy model simulations using (a) lab-observed and (b) correlated input parameter sets for the untreated embankment against Breland et al. (2025) breach experiment measurements. 111
Figure 51. Comparison of breach experiment breach widening progression from WinDAM C energy model simulations using (a) lab-observed and (b) correlated input parameter sets for the untreated embankment against Breland et al. (2025) breach experiment measurements. 112
Figure 52. Comparison of breach experiment hydraulic control progression from WinDAM C energy model simulations using (a) lab-observed and (b) correlated

input parameter sets for the untreated embankment against Breland et al. (2025) breach experiment measurements. ... 112
Figure 53. Comparison of breach experiment headcut progression from WinDAM C stress model simulations using (a) lab-observed and (b) correlated input parameter sets for the untreated embankment against Breland et al. (2025) breach experiment measurements. ... 113
Figure 54. Comparison of breach experiment breach widening progression from WinDAM C stress model simulations using (a) lab-observed and (b) correlated input parameter sets for the untreated embankment against Breland et al. (2025) breach experiment measurements. ... 113
Figure 55. Comparison of breach experiment hydraulic control progression from WinDAM C stress model simulations using (a) lab-observed and (b) correlated input parameter sets for the untreated embankment against Breland et al. (2025) breach experiment measurements. ... 114
Figure 56. Comparison of breach experiment headcut progression from DLBreach simulations using (a) lab-observed and (b) correlated input parameter sets for the untreated embankment against Breland et al. (2025) breach experiment measurements. ... 115
Figure 57. Comparison of breach experiment breach widening progression from DLBreach simulations using (a) lab-observed and (b) correlated input parameter sets for the untreated embankment against Breland et al. (2025) breach experiment measurements. ... 115
Figure 58. Comparison of breach experiment hydraulic control progression from DLBreach simulations using (a) lab-observed and (b) correlated input parameter sets for the untreated embankment against Breland et al. (2025) breach experiment measurements. ... 116
Figure 59. Comparison of breach experiment headcut progression from WinDAM C energy model simulations using (a) lab-observed and (b) correlated input parameter sets for the treated embankment against Breland et al. (2025) breach experiment measurements. ... 117
Figure 60. Comparison of breach experiment breach widening progression from WinDAM C energy model simulations using (a) lab-observed and (b) correlated input parameter sets for the treated embankment against Breland et al. (2025) breach experiment measurements. ... 117
Figure 61. Comparison of breach experiment hydraulic control progression from WinDAM C energy model simulations using (a) lab-observed and (b) correlated input parameter sets for the treated embankment against Breland et al. (2025) breach experiment measurements. ... 118
Figure 62. Comparison of breach experiment headcut progression from WinDAM C stress model simulations using (a) lab-observed and (b) correlated input parameter sets for the treated embankment against Breland et al. (2025) breach experiment measurements. ... 119
Figure 63. Comparison of breach experiment breach widening progression from WinDAM C stress model simulations using (a) lab-observed and (b) correlated input parameter sets for the treated embankment against Breland et al. (2025) breach experiment measurements. ... 119

Figure 64. Comparison of breach experiment hydraulic control progression from WinDAM C stress model simulations using (a) lab-observed and (b) correlated input parameter sets for the treated embankment against Breland et al. (2025) breach experiment measurements. 120
Figure 65. Comparison of breach experiment headcut progression from DLBreach model simulations using (a) lab-observed and (b) correlated input parameter sets for the treated embankment against Breland et al. (2025) breach experiment measurements. 121
Figure 66. Comparison of breach experiment breach widening progression from DLBreach model simulations using (a) lab-observed and (b) correlated input parameter sets for the treated embankment against Breland et al. (2025) breach experiment measurements. 121
Figure 67. Comparison of breach experiment hydraulic control progression from DLBreach model simulations using (a) lab-observed and (b) correlated input parameter sets for the treated embankment against Breland et al. (2025) breach experiment measurements. 122
Figure 68. Comparison of combined overtopping-plus-breach experiment upstream water surface elevations from WinDAM C energy model simulations using (a) lab-observed, (b) correlated, and (c) best-fit input parameter sets for the untreated embankment against ERDC (2025) and Breland et al. (2025) experimental measurements. 126
Figure 69. Comparison of combined overtopping-plus-breach experiment headcut progression from WinDAM C energy model simulations using (a) lab-observed, (b) correlated, and (c) best-fit input parameter sets for the untreated embankment against Breland et al. (2025) breach experiment measurements. 127
Figure 70. Comparison of combined overtopping-plus-breach experiment breach widening progression from WinDAM C energy model simulations using (a) lab-observed, (b) correlated, and (c) best-fit input parameter sets for the untreated embankment against Breland et al. (2025) breach experiment measurements. 128
Figure 71. Comparison of combined overtopping-plus-breach experiment hydraulic control progression from WinDAM C energy model simulations using (a) lab-observed, (b) correlated, and (c) best-fit input parameter sets for the untreated embankment against Breland et al. (2025) breach experiment measurements. 129
Figure 72. Comparison of combined overtopping-plus-breach experiment upstream water surface elevations from WinDAM C stress model simulations using (a) lab-observed, (b) correlated, and (c) best-fit input parameter sets for the untreated embankment against ERDC (2025) and Breland et al. (2025) experimental measurements. 131
Figure 73. Comparison of combined overtopping-plus-breach experiment headcut progression from WinDAM C stress model simulations using (a) lab-observed, (b) correlated, and (c) best-fit input parameter sets for the untreated embankment against Breland et al. (2025) breach experiment measurements. 132
Figure 74. Comparison of combined overtopping-plus-breach experiment breach widening progression from WinDAM C stress model simulations using (a) lab-observed, (b) correlated, and (c) best-fit input parameter sets for the untreated embankment against Breland et al. (2025) breach experiment measurements. 133

Figure 75. Comparison of combined overtopping-plus-breach experiment hydraulic control progression from WinDAM C stress model simulations using (a) lab-observed, (b) correlated, and (c) best-fit input parameter sets for the untreated embankment against Breland et al. (2025) breach experiment measurements. 134
Figure 76. Comparison of combined overtopping-plus-breach experiment upstream water surface elevations from WinDAM C energy model simulations using (a) lab-observed, (b) correlated, and (c) best-fit input parameter sets for the treated embankment against ERDC (2025) and Breland et al. (2025) experimental measurements. 136
Figure 77. Comparison of combined overtopping-plus-breach experiment headcut progression from WinDAM C energy model simulations using (a) lab-observed, (b) correlated, and (c) best-fit input parameter sets for the treated embankment against Breland et al. (2025) breach experiment measurements. 137
Figure 78. Comparison of combined overtopping-plus-breach experiment breach widening progression from WinDAM C energy model simulations using (a) lab-observed, (b) correlated, and (c) best-fit input parameter sets for the treated embankment against Breland et al. (2025) breach experiment measurements. 138
Figure 79. Comparison of combined overtopping-plus-breach experiment hydraulic control progression from WinDAM C energy model simulations using (a) lab-observed, (b) correlated, and (c) best-fit input parameter sets for the treated embankment against Breland et al. (2025) breach experiment measurements. 139
Figure 80. Comparison of combined overtopping-plus-breach experiment upstream water surface elevations from WinDAM C stress model simulations using (a) lab-observed, (b) correlated, and (c) best-fit input parameter sets for the treated embankment against ERDC (2025) and Breland et al. (2025) experimental measurements. 141
Figure 81. Comparison of combined overtopping-plus-breach experiment headcut progression from WinDAM C stress model simulations using (a) lab-observed, (b) correlated, and (c) best-fit input parameter sets for the treated embankment against Breland et al. (2025) breach experiment measurements. 142
Figure 82. Comparison of combined overtopping-plus-breach experiment breach widening progression from WinDAM C stress model simulations using (a) lab-observed, (b) correlated, and (c) best-fit input parameter sets for the treated embankment against Breland et al. (2025) breach experiment measurements. 143
Figure 83. Comparison of combined overtopping-plus-breach experiment hydraulic control progression from WinDAM C stress model simulations using (a) lab-observed, (b) correlated, and (c) best-fit input parameter sets for the treated embankment against Breland et al. (2025) breach experiment measurements. 144
Figure 84. Final log-residual summary of simulated headcut progression and breach width for untreated and biopolymer-treated embankments across the correlated and best-fit simulation cases. 147
Figure 85. Heatmap of relative parameter sensitivity effects from the Dakota sensitivity analysis for the WinDAM C energy-based model, WinDAM C stress-based model, and DLBreach model, showing the relative response changes in breach metrics between the minimum and maximum tested parameter values. 149

Figure 86. Lollipop plots of relative parameter sensitivity effects from the Dakota sensitivity analysis for the WinDAM C energy-based model, WinDAM C stress-based model, and DLBreach model, illustrating the magnitude and direction of output response changes associated with increasing and decreasing input parameter values....... 150
Figure 87. WinDAM C overtopping erosion progression: (a) erosion initiation starting with headcut advance, (b) headcut progression coincident with slight widening, (c) mature stage with headcut migration and gradual lateral expansion (blue = overtopping/widening, red = headcut, dashed = removed embankment)........ 186

List of Abbreviations

AC – Advance Coefficient

ADCP – Acoustic Doppler Current Profiler

ASCE – American Society of Civil Engineers

ASTM – American Society for Testing and Materials

EFA – Erosion Function Apparatus

ERDC – U.S. Army Corps of Engineers Engineer Research and Development Center

ERF – Electrostatic Repulsion Force

FEMA – Federal Emergency Management Agency

JET – Jet Erosion Test

k_d – Erodibility Coefficient

K_h – Erodibility Index

K_b – Particle Size Number

K_d – Interparticle Bond Shear Strength Number

MDD – Maximum Dry Density

n – Manning's Roughness Coefficient

NRCS – Natural Resources Conservation Service

OMC – Optimum Moisture Content

Pa - Pascal

pcf – Pounds per Cubic Foot

PI – Plasticity Index

psf – Pounds per Square Foot

RCC – Roller-Compacted Concrete

RCI – Retardance Curve Index

s_u – Undrained Shear Strength

SPT – Standard Penetration Test

SHRF – Surface-Hydration Repulsion Force

τ_c – Critical Shear Stress

VCF – Vegetal Cover Factor

vDWAF – van der Waals Attraction Force

XG – Xanthan Gum

UCS – Unconfined Compressive Strength

USACE – U.S. Army Corps of Engineers

USDA – United States Department of Agriculture

UCS – Unconfined Compressive Strength

CHAPTER 1: Introduction

1.1 Background

Overtopping of earthen dams and levees poses severe risks to human life, infrastructure, and ecosystems, with historical failures resulting in catastrophic loss of life, substantial property damage, and long-term environmental degradation from sediment-laden floodwaters (Sacramento County 2025; FEMA 2012). Case histories clearly illustrate these severe consequences, including: the 1991 Belci Dam disaster in Romania resulted in 25 fatalities and extensive infrastructure destruction after heavy rainfall led to overtopping and eventual breach (Sharma et al. 2013); in 1982, the Tous Dam in Spain was overtopped after unprecedented rainfall overwhelmed the spillway capacity and gate failures prevented emergency drawdown, resulting in eight deaths and the evacuation of over 100,000 people, with economic losses exceeding $400 million (Alcrudo and Mulet 2007); and the 2005 Taum Sauk Upper Reservoir failure was triggered by overtopping induced by instrumentation and operational errors, causing rapid embankment breach within minutes, extensive downstream flooding, and regulatory reforms (Rodgers et al. 2010).

Numerous studies have investigated the potential of numerical and physically based models to capture breaches in earthen dams caused by overtopping. Early work on earth-dam failure focused on breach geometry, reservoir release, and the hydraulic controls on peak discharge, including the physically based BREACH model developed by Fread (1988) and the dimensionless breach-discharge relations of Walder and O’Connor (1997). Froehlich (2008) later expanded this foundation by developing empirical relations for final breach width, side-slope ratio, and breach formation time from a large database of embankment dam failures. More recent models use physically based approaches that integrate broad-crested weir hydraulics, excess shear stress frameworks for erosion, and trapezoidal breach evolution governed by slope stability analyses (Chang and Zhang 2010; Dong et al. 2021; Song et al. 2024; Zhang et al. 2024). These newer models are especially useful for landslide dams and coarse, noncohesive deposits, where surface erosion dominates, and model response is highly sensitive to gradation, spatial variability, and erosion-rate limits.

Mitigating erosion from overtopping requires either preventing or slowing erosion. There are various options for this, including soft and hard protection systems intended to delay erosion initiation, reduce flow velocities, or increase the time to failure during extreme events (Hanson and Hunt 2007; Morán et al. 2026). Riprap remains a widely used protective measure because it can provide effective resistance to small overtopping flows, although its performance depends on slope, median stone size, layer thickness, and rock shape (Abt and Johnson 1991; Wahl 2016). On steep slopes, a substantial portion of the flow may move through the riprap layer rather than solely over its surface, making interstitial flow an important design consideration (Wahl 2016). Vegetation can also provide some protection by reducing velocity and reinforcing the surface soil, but it is generally suitable only for limited overtopping intensities and durations (Hanson and Hunt 2007; Morán et al. 2026). Where greater protection is needed, systems such as gabions, articulated concrete blocks, reinforced rockfill, and roller-compacted concrete offer higher erosion resistance, although at higher cost and with more restrictive application limits (Morán et al. 2026).

Biopolymer-based soil treatments are a recent development that can enhance interparticle bonding, elevating the critical shear stress and undrained shear strength while reducing erodibility (Walshire et al. 2024; Kwon et al. 2020). These modifications shift erosion patterns from rapid surface scour to delayed headcut-dominated progression with narrower final breaches, necessitating novel parameterizations for biopolymer effects in heterogeneous embankment soils. To assess the viability of biopolymer treatment, this research identifies critical soil parameters governing failure metrics (timing and extent) and informs more effective design protocols.

While numerous studies have examined overtopping erosion and breach development in earthen embankments, the specific response of current breach-prediction models to biopolymer treatment effects has not been evaluated in a full-scale experimental context. This study addresses that gap by assessing whether established numerical models can represent the influence of biopolymer treatment on overtopping-induced erosion, breach initiation, and breach progression. In particular, the work compares model performance for treated and untreated embankments, evaluates agreement with observed breach evolution, and examines how well the models capture the time-dependent effects of treatment on erosion resistance. By doing so, this thesis extends existing breach modeling approaches to a newly studied treatment condition and provides insight into both the strengths and limitations of current predictive methods for biopolymer-treated embankments.

1.2 Objectives

The focus of the research presented herein is to evaluate current tools for modeling overtopping-induced erosion of biopolymer-treated earthen embankments. Two commonly used overtopping models are considered: WinDAM C (Temple et al. 2005; Hanson et al. 2005) and DLBreach (Wu 2013, 2016). While these tools have similar capabilities, they use different approaches, and neither has been used to simulate biopolymer treatments. The simulation results are compared with observations from two near full-scale overtopping experiments conducted by Kang et al. (2021) at the Andong River Experiment Center in South Korea and Breland et al. (2025) at the Engineer Research and Development Center (ERDC) in Vicksburg, Mississippi. Through this work, this study aims to provide guidance on incorporating the effects of biopolymer treatment into current analysis and design practices for flood control on earthen embankments.

The specific objectives of this study include the following:

- Evaluate how well WinDAM C and DLBreach capture breach development for biopolymer-treated and untreated earthen embankments subjected to overtopping.
- Quantify the effects of biopolymer treatment on key breach metrics, including headcut migration rate, breach width, and hydraulic control elevation.
- Develop and validate parameter estimation methods for incorporating biopolymer treatment effects into breach model inputs.
- Use Dakota uncertainty quantification software to conduct sensitivity analyses and identify which soil and erosion parameters have the greatest influence on overtopping breach predictions in both modeling platforms.

1.3 Scope of Work

To accomplish the objectives of this study as outlined in Section 1.2, the following tasks were performed:

1. Evaluate previous overtopping experiments on biopolymer-treated embankments performed and documented by Kang et al. (2021) and Breland et al. (2025).
2. Develop simulations of these experiments using the WinDAM C and DLBreach programs.
3. Compare the simulation outputs to observations to understand the performance of each program.
4. Evaluate the influence of different input parameters through a correlation analysis using Dakota (Adams et al. 2009).

1.4 Organization of Thesis

This thesis is organized into six chapters. Chapter 1 presents the introduction, problem statement, and research objectives. Chapter 2 provides background on overtopping processes, traditional remediation approaches, the mechanics of erosion in cohesive soils, and current knowledge of biopolymer effects on soil properties related to erosion. Chapter 3 describes the modeling approach, including model descriptions (WinDAM C and DLBreach), input parameter and output metric descriptions for both models, descriptions of the experiments, and an overview of the Dakota sensitivity framework. Chapter 4 presents simulation results for both experiments, organized by model and treatment condition. Chapter 5 discusses the interpretation of results, model performance, and implications for practice. Chapter 6 provides conclusions and recommendations for future research.

CHAPTER 2

Background and Literature Review

This background and literature review describes the current state of practice in the areas of overtopping and erosion of cohesive soils in earth embankments.

2.1 Overtopping Failure of Earthen Embankments

When an earthen embankment is overtopped, the water begins eroding the crest and downstream face. The erosion rate is controlled by topography, soil properties, vegetation type and height, and the presence of structures or riprap on the embankment face or crest. Studies show that the erodibility of cohesive soils depends on physical factors such as particle size distribution, bulk density, water content, temperature, and plasticity, as well as geochemical factors like clay mineralogy and organic matter content, which together govern the balance between hydraulic driving forces and resistive forces such as gravity, friction, cohesion, and adhesion (Grabowski et al. 2011; Chen et al. 2022; Hanson and Robinson 1993; Hanson and Hunt 2007; Regazzoni et al. 2008). Vegetation can substantially increase erosion resistance by reinforcing the near-surface zone through roots and binding soil between root networks, although its effectiveness depends on root density, species, and cover continuity (Mozer et al. 2025; Gyssels et al. 2005; de Baets et al. 2020). Conversely, where the embankment face is bare, overtopping flows more readily initiate surface erosion, headcut development, and eventual breach (Zhao et al. 2015; Wu 2011).

Approaches to analyze overtopping-induced erosion are commonly categorized as being applicable to either cohesive or noncohesive soils. This categorization is performed based on defining the characteristics of cohesive sediments, which are strong interparticle attractions manifesting in two principal forms: cohesion (electrochemical bonding between fine particles) and adhesion (binding by additional substances, such as organic polymers or iron oxides, via cation bridging or polymerization) (Grabowski et al. 2011; Chen et al. 2022). This study will focus on overtopping of cohesive earthen dams and levees, where failure is a progressive process characterized by distinct stages of erosion and breach development (Hanson et al. 2005). Stage 1 is the initiation stage, during which surface erosion begins on the downstream slope, leading to rill development and the formation of a distinct overfall or headcut (Figure 1a; Hanson et al. 2005). Stage 2 is the headcut stage, during which headcut migration occurs upslope toward the crest as plunge-pool scour deepens and destabilizes the vertical face (Figure 1b). Stage 3 is the lateral widening stage, where the headcut breaches the dam crest, allowing reservoir water to accelerate erosion and rapidly enlarge the breach channel (Figure 1c). Stage 4 is the equilibrium stage, in which the embankment has fully breached, and water can flow freely through the breach (Figure 1d).

Complementing this framework, Zhou et al. (2019) showed through large-scale flume tests that overtopping-induced breach evolution can be divided, after breach initiation (Figure 1e), into three hydrodynamic stages: (1) an initial headcut erosion process, where erosion migrates from the downstream crest toward the upstream crest (Figure 1f), (2) an accelerated erosional process, marked by rapid increases in velocity, outflow discharge, and sediment entrainment (Figure 1g), and (3) an attenuating erosional process, where stream power declines and erosion rates taper (Figure 1h).

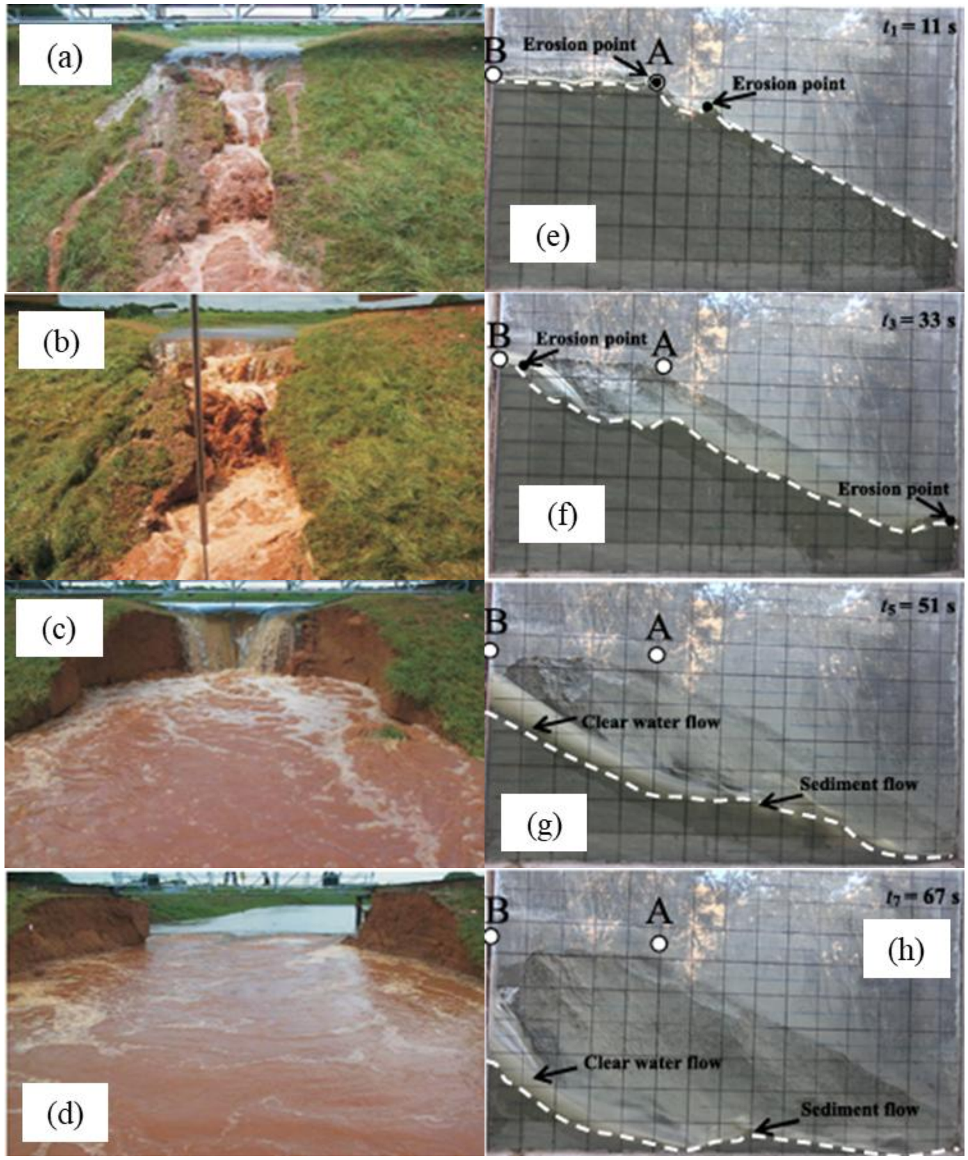

Figure 1. Different stages of headcut progression from physical models of breaching: (left) longitudinal profile view adapted from Hanson et al. (2005) and (right) cross-sectional elevation view adapted from Zhou et al. (2019).

2.1.1 Mitigation Efforts

Traditional mitigation strategies for overtopping-induced erosion include RCC armoring, precast concrete blocks, riprap, and vegetation. The objective of these treatments is to prevent or reduce erosion by providing a protective, erosion-resistant surface over the more vulnerable earth material (Cooper et al. 2014). RCC (Figure 2a) is a durable and dense material placed in horizontal layers on dam slopes to resist erosion from overtopping flows (Hansen and Fitzgerald 2016). Precast concrete blocks (Figure 2b) can be used to form a flexible, hard surface to safely convey overtopping flow without eroding the underlying soil. They accommodate minor subgrade changes while resisting hydraulic forces when properly installed over filtered drainage layers (Hepler et al. 2012). Riprap (Figure 2c) consists of layers of large, angular rock laid on embankment slopes to resist erosion by reducing flow velocity and shear stress on the soil. Properly designed riprap, particularly when provided with adequate toe support, can significantly delay or prevent breach initiation during overtopping events (Wahl 2016). Vegetation (Figure 2d) reduces erosion by slowing water flow through aboveground leaves and stalks and by strengthening soil structure via roots, with effectiveness increasing as vegetation matures (Zhou et al. 2024).

Biopolymer-based soil stabilization has emerged as a scalable and environmentally friendly alternative for erosion control (Larson et al. 2019; Chang et al. 2016). Biopolymers are naturally occurring macromolecules synthesized by microbial activity. These biogenic polymers facilitate interparticle bonding within soil matrices, thereby enhancing the mechanical integrity of the treated soil (Kwon et al. 2020). Small-scale overtopping experiments have demonstrated that biopolymer-treated embankments delay breach initiation and reduce peak outflow rates compared to untreated controls (Czapiga et al. 2024). Biopolymer treatment also enhances vegetal growth by improving soil moisture retention, creating a synergistic, erosion-resistant system (Larson et al. 2019; Zhang and Liu 2023). Compared to cement mitigation techniques, biopolymer treatments may decrease carbon emissions by 85% (Rasheed et al. 2023).

Despite the demonstrated advantages of biopolymer treatments for overtopping protection, several barriers remain to their widespread adoption. The first is a lack of full-scale experimental studies assessing their performance under realistic loading conditions. The recent large-scale overtopping tests conducted by Kang et al. (2021) and the USACE (Breland et al. 2025) have started to fill this gap. The second is that there are no established methodologies for incorporating biopolymer effects into breach analyses.

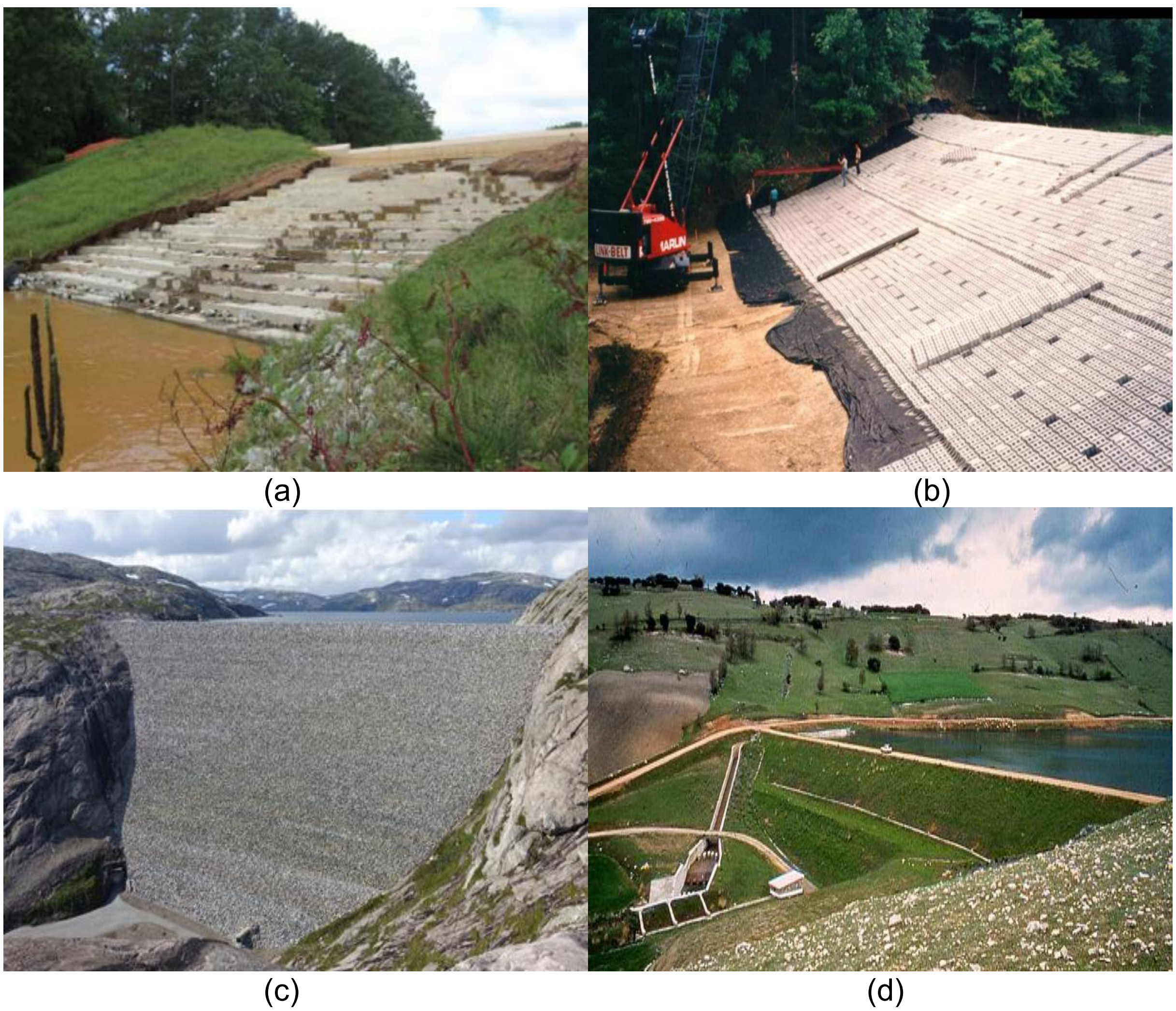

Figure 2. (a) Post-overtopping condition of the downstream spillway at Y16 Dam, Georgia, illustrating complete loss of surface cover but preservation of embankment integrity due to RCC armoring (Hansen and Fitzgerald 2016). (b) Placement of articulated concrete block mats over geotextile on the downstream slope of Strahl Lake Dam, Indiana (photo by Contech Construction Products, Inc.). (c) Downstream slope

of Dam Svartevatn, Norway, protected by interlocking placed riprap (Hiller 2017). (d) Earth dam with well-established vegetative cover on the downstream slope (García-Asensio and Ayuga 2017).

2.2 Erosion Mechanics of Cohesive Soils

Erosion of cohesive sediment is a complex phenomenon influenced by the soil's physical, chemical, and structural properties. Erosion occurs when fluid-transmitted forces, such as boundary layer shear stress and turbulence, exceed the cumulative resistive forces at the bed surface. The magnitude of these resistive forces depends on aggregate stability, pore-water chemistry, mineralogy, organic matter, structural arrangement, and compaction (Winterwerp and van Kesteren 2004; Sanford 2008). Critical control factors additionally include bed shear strength, interparticle bonding, and sediment consolidation state, which together govern the threshold and rate of erosion for cohesive beds (Ali and Setia 2015; Grabowski et al. 2011).

Cohesive sediments, pervasive in both aquatic and geotechnical environments, commonly erode as aggregates under low bed shear stresses, whereas noncohesive soils such as sands are governed mainly by particle weight, buoyancy, drag, and lift, so erosion proceeds by displacement of individual grains, with critical shear stress and scour evolution controlled primarily by grain size, density, and packing as described by Shields-type frameworks and jet scour studies (Chen et al. 2022; Chen et al. 2018; di Nardi et al. 2022). In cohesive soils, fine clay- and silt-sized particles interact through physicochemical forces and form flocs and higher-order aggregates, so the threshold and rate of erosion depend on aggregate structure, consolidation, and internal bonding rather than grain size alone (Forsberg et al. 2018; Yu et al. 2022; Thomaz et al. 2022). The breakdown or stabilization of these aggregates is determined by the interplay of interparticle forces: Electrostatic Repulsion Force (ERF), van der Waals Attraction Force (vDWAF), and Surface-Hydration Repulsion Force (SHRF) (Calero et al. 2017; Hu et al. 2015; Li et al. 2013; Xu et al. 2015; Yu et al. 2017). ERF arises from overlapping electric double layers, vDWAF from electromagnetic molecular attraction, and SHRF from interactions between clay surfaces and water molecules (Low 1987; van Oss 2006). Stable soil aggregates are crucial for enhancing permeability and mitigating soil erosion (Yu et al. 2020).

The erodibility of cohesive sediment is commonly described in terms of an erosion threshold and an erosion rate, both of which are influenced by sediment properties such as gravity, friction, cohesion, and adhesion (Grabowski et al. 2011). The key parameters used to quantify this behavior are critical shear stress (τ_c), which defines the hydrodynamic condition required to initiate sediment loss, and the erodibility coefficient (k_d), which measures the mass of sediment removed per unit time per unit shear stress applied to the soil (Forsberg et al. 2018; Li et al. 2022; Mehta et al. 1989; Sanford & Maa 2001). Because these properties and processes vary with soil structure, fines content, and loading history, cohesive-soil erodibility is highly variable in space and time, and measurement is complicated by the dynamic interplay of sediment properties (Black et al. 2002; Grabowski et al. 2011). Both parameters are described in more detail in the following sections of this chapter.

Once erosion initiates on a cohesive embankment, the rate at which the breach develops is determined by the rate of migration of the vertical scarp upstream, known as the headcut (Temple & Moore 1994). Among breach processes, headcut advance is considered one of the most complex and least understood phenomena (Temple & Moore 1994). Experimental research has demonstrated that geometric and hydraulic factors, including upstream slope gradient, headcut drop height, and unit flow discharge, substantially affect the rate of headcut migration (Bennett 1999; Bennett et al. 2000; Zhang et al. 2018; Shan et al. 2023). Steeper slopes and higher drops generally accelerate upstream advance (Bennett 1999). Recent findings emphasize the significance of vegetation: grass cover with fine roots can reduce both total soil loss and headcut retreat by up to 85% compared to bare soils (Guo et al. 2019).

The rate of headcut migration is sensitive to texture, clay content, mineral composition, vertical joints, bulk density, water content, and other physicochemical characteristics that modulate the soil's erodibility (Nazari Samani et al. 2010; Sanchis et al. 2008; Vanmaercke et al. 2016; Guo et al. 2020; Shan et al. 2023). For example, densely compacted soils with higher clay fractions and lower water content tend to resist headcut migration more strongly, whereas loosely packed, wetter soils experience more rapid erosion (Shan et al. 2023). Interestingly, some studies have found that flow velocity at the brink of a headcut is not a significant predictor of soil loss compared to these intrinsic properties (Guo et al. 2021). For overtopping, the rate at which the headcut will move can be either correlated with undrained shear strength (s_u) (stress-based approach) or specified using a headcut advance rate (energy-based approach), which may be a single parameter or determined based on other soil properties (Hanson et al. 2011).

2.2.1 Critical Shear Stress

τ_c is the hydraulic stress threshold at which soil detachment and erosion are initiated and is widely recognized as a crucial parameter for modeling cohesive sediment erosion (Briaud et al. 2001; Chen et al. 2022; Kulesza et al. 2024). In cohesive sediments, τ_c is influenced by numerous factors, including bed density, mineral and particle-size composition, organic content, salinity, temperature, pH, and sodium absorption ratio (Wu and Perera 2015). Although no single unifying equation can predict τ_c, soil properties, laboratory tests, and field measurements help identify key erosion-related characteristics. Experimental studies have shown that τ_c correlates strongly with dry density and may scale approximately linearly with compressive or vane shear strength. In fine-grained soils, τ_c generally increases with plasticity index and undrained shear strength (Arulanandan et al. 1980; Bonilla and Johnson 2012; Shan et al. 2015; Kulesza and Karim 2021; Kulesza et al. 2024) with reported values on the order of 0-5 N/m² (Owen 1975; Thorn and Parsons 1980; Nicholson and O'Connor 1986; Kamphuis and Hall 1983; Briaud et al. 2001; Kulesza et al. 2024).

2.2.2 Erodibility Coefficient

k_d quantifies the rate of erosion once applied shear stress exceeds τ_c and is typically expressed as the rate of mass loss per unit area per unit excess shear stress (Forsberg et al. 2018; Mehta et al. 1989; Sanford & Maa 2001). After τ_c is exceeded, particle movement and transport through rills or headcuts accelerate in soils with high k_d, whereas more resistant soils with lower k_d erode more slowly (Lee et al. 2021; Hanson et al. 2011). Experimental work has shown that k_d often decreases with increasing shear strength, reflecting the greater resistance of more consolidated, clay-rich materials. Fine content and stress history, as captured by indices such as the void index, can impart substantial variability in k_d and surface erosion behavior (Mehta and Parchure 2000; Kulesza et al. 2024). Because both k_d and τ_c can evolve over time with changes in consolidation, moisture, and chemistry, accounting for their spatiotemporal variability is critical. Erosion models that assume fixed values may introduce significant seasonal errors in predicted erosion rates (Briaud et al. 2001; Lee et al. 2021).

2.2.3 Undrained Shear Strength

The s_u of cohesive sediments can be correlated with resistance to erosion, though research has produced mixed conclusions about the strength of this relationship. Early studies, such as Sundborg (1956), suggested that the cohesive force opposing grain detachment is directly proportional to the sediment's measured s_u. Other investigations have highlighted the dual importance of both the active fluid forces and the passive resistance provided by s_u in controlling erosion rates (Abdel-Rahman 1963). Furthermore, experiments have observed an inverse correlation between measured s_u and soil loss rate, indicating that higher s_u is often associated with lower soil loss rates (Shaikh et al. 1988).

The mechanical and hydraulic behavior of cohesive soils depends significantly on drainage conditions. According to Winterwerp et al. (2012), surface erosion is mainly a mechanical process that occurs under drained conditions, whereas mass erosion (headcut) typically occurs under undrained conditions. At the macroscale, soil behavior is largely governed by drainage, with undrained shear strength typically higher than drained shear strength in denser or overconsolidated soils (Winterwerp et al. 2012). When flow-induced stress becomes sufficiently large, it can exceed the local s_u, resulting in the removal of lumps of material from the bed, a process commonly observed as headcut advance (Winterwerp et al. 2012). Supporting this, field and laboratory measurements suggest that s_u can serve as a useful proxy for assessing soil erodibility under hydraulic loading (Harris and Whitehouse 2015).

2.3 Effects of Biopolymer Treatment on Erosion Resistance

Biopolymers can enhance the overtopping erosion resistance of cohesive soils by interparticle bonding and pore clogging, thereby increasing soil cohesiveness and improving its resistance to hydrodynamic forces (Chang et al. 2020; Ayeldeen et al. 2016). Biopolymers can also enhance vegetation growth and root reinforcement, which are vital components of overtopping resistance (Wang et al. 2023; Ni et al. 2023; Arabani et al. 2024). The next sections provide a brief review of the observed effects of biopolymer treatment on erosion parameters for cohesive soils

2.3.1 Critical Shear Stress and Erodibility Coefficient

Kwon et al. (2020) performed EFA tests on a soft marine soil mixed with either 1% and 2% XG. Their results (Figure 3) show that biopolymer-treated soils exhibit higher τ_c (as indicated by the delayed onset of erosion) and a reduced k_d (shown by the erosion rate after initiation). They found that τ_c increased by ~800% with 1% XG, while k_d decreased by ~80%. Further treatment with 2% XG led to additional improvements, but not at the same rate as the initial treatment (Figure 3a). Similar results were seen with tests on XG-treated kaolinite clay (Kwon et al. 2023a) (Figure 3b). These enhancements are attributed to biopolymers forming cohesive networks that bind soil particles, as well as clogging pores and forming hydrogels that absorb shear energy (Ayeldeen et al. 2016).

Walshire et al. (2024) documented JET performed on two natural clayey soils (Brabston Clay and Vicksburg Silt) treated with biopolymers. Vicksburg Silt is a lean clay and highly erodible, whereas Brabston Clay is a fat clay and exhibits moderate erosion resistance. The soils were both treated with 1% biopolymer, and the JET results showed that the treatment reduced $τ_c$ by approximately 4 times in the Vicksburg Silt but increased $τ_c$ in the Brabston Clay. Similarly, k_d decreased by ~83% for biopolymer-treated Vicksburg Silt but increased for Brabston Clay. The Brabston Clay does not fit the pattern observed in other studies, but this may be partially attributed to Brabston Clay being fairly resistant to erosion before testing. It is unclear why the treatment increased erodibility, but this demonstrates that soil type is important when assessing potential improvements.

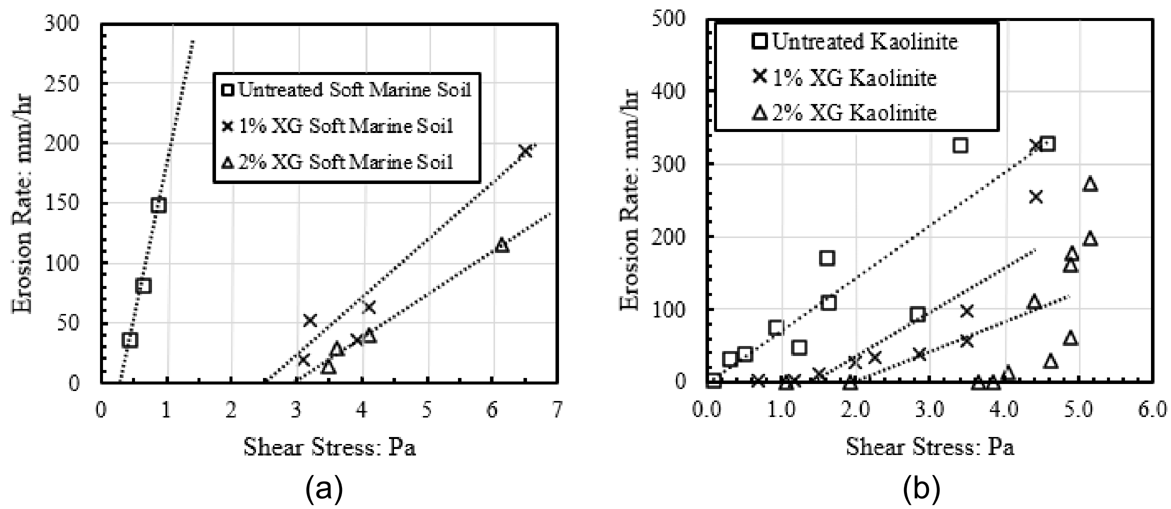

Figure 3. Changes in erosion resistance of (a) soft marine clay (data from Kwon et al. 2020) and (b) kaolinite (data from Kwon et al. 2023a) with increasing amounts of treatment with XG as measured with an EFA.

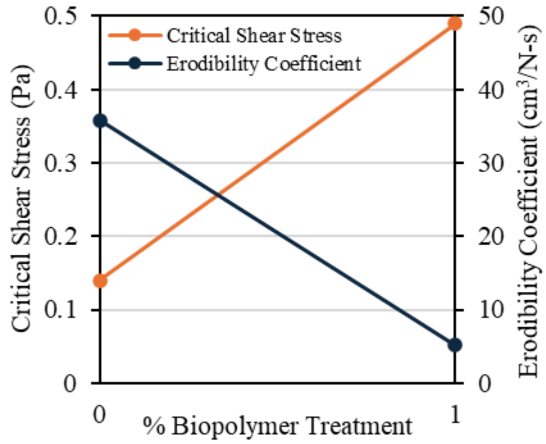

Figure 4. Representative JET results from Walshire et al. (2024) showing the critical shear stress and erodibility coefficient of Vicksburg Silt, and the modification of these parameters under a 1% biopolymer treatment.

2.3.2 Undrained Shear Strength

Studies utilizing direct shear and unconfined compression tests (Ayeldeen et al. 2016) demonstrate that biopolymer-treated soils exhibit significant increases in s_u parameters relative to untreated controls, with the extent of improvement influenced by both the type of biopolymer and its concentration. For silt, the UCS increased markedly with the addition of biopolymers: untreated silt exhibited a UCS of nearly 75 kPa, rising to 338 kPa with 2% xanthan gum, 570 kPa with 2% modified starch, and 840 kPa with 2% guar gum after five weeks of curing (Figure 5a). In sand specimens, incorporation of 2% guar gum by weight increased cohesion from 0 kPa in untreated samples to 447 kPa after one week of curing. Similarly, treatments with 2% modified starch and 2% xanthan gum produced cohesion values of 309 kPa and 218 kPa, respectively, under identical curing conditions (Figure 5b).

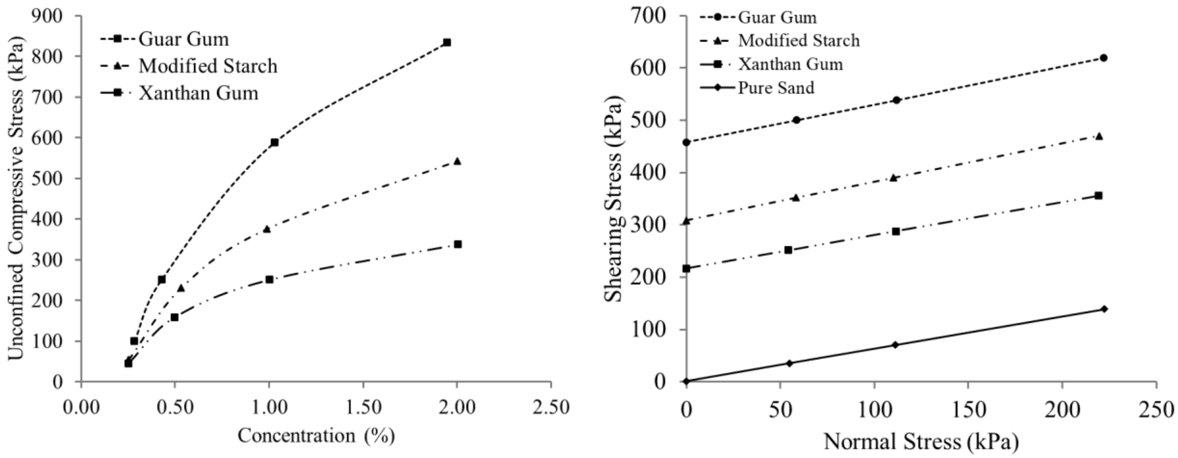

(a) (b)

Figure 5. Unconfined compressive strengths of biopolymer-treated silt as a function of biopolymer concentration (a), and corresponding failure envelopes of sand at 2% biopolymer concentration (b), both after 5 weeks of curing, as reported by Ayeldeen et al. (2016).

2.3.3 Headcut Advance

The application of biopolymers to cohesive soils has been shown to substantially alter the fundamental properties that control both erosion resistance and headcut advance rate, but the author is unaware of any studies that directly measure these effects. Biopolymer treatments enhance soil structure at the particle scale by increasing interparticle cohesion, filling pore spaces, and forming a gel-like or hydrogel matrix that physically binds soil particles together, thereby reducing their susceptibility to detachment and flow-induced migration (Kwon et al. 2023a; Kumar et al. 2025). In undrained conditions, even low dosages (1-3% by weight) of lignin, xanthan gum, or guar gum have been observed to double or triple the measured soil cohesion, substantially raise peak and residual strengths, and suppress pore water flow by reducing permeability (Bagheri et al. 2024; Kumar et al. 2025). These improvements translate into increased resistance to both surface erosion and slope failure, with treated soils exhibiting smaller, shallower headcut formation and significantly slower upstream migration under flume and rainfall simulation tests (Kumar et al. 2025; Kwon et al. 2023a, 2023b; Czapiga et al. 2024).

2.4 Modeling Headcut Progression Due to Overtopping of Earthen Embankments

Headcut erosion is widely recognized as a central mechanism in the failure and enlargement of cohesive embankments because it controls the upstream extension of erosion once a distinct scarp or overfall has formed (Zhao et al. 2012; Stein and LaTray 2002). The literature shows that headcut advance is not only a theoretical erosion problem, but one that has been repeatedly observed to produce measurable upstream retreat, discrete collapse events, and rapid changes in breach development under overtopping conditions (Stein and LaTray 2002; Zhao et al. 2012). At the same time, previous studies have approached the problem through both energy- and stress-based frameworks, reflecting the fact that headcut migration is governed by the coupled interactions among hydraulic forcing, scour development, soil resistance, and episodic mass failure (Temple & Moore 1994; Hanson et al. 2001; Hunt et al. 2021; Shan et al. 2023).

Energy-based methods relate the advance rate to the energy dissipated at the headcut brink during flow, typically incorporating material resistance via a headcut erodibility index (Temple & Moore 1994). These models have proven field-applicable and offer an explicit representation of headcut migration mechanisms, but their performance depends heavily on calibration data (Temple and Moore 1994; Hanson et al. 2011; Shan et al. 2023). Material-dependent coefficients may be estimated from historic site performance or laboratory detachment tests, and model development continues to benefit from broader testing and parameter studies that clarify how soil properties influence migration rate (Hanson et al. 2011; Shan et al. 2023).

Stress-based models, by contrast, treat headcut migration as a series of mass failures that occur when hydraulic stresses exceed the soil's mechanical resistance, often represented through undrained shear strength (Hanson et al. 2001; Hunt et al. 2021; Shan et al. 2023). These formulations use total unit weight, headcut geometry, and measured soil strength to predict episodic block collapses, which is a common feature of cohesive embankment failure (Hanson et al. 2001). Their main advantage is that they rely on measurable soil parameters, but their applicability can be limited because the governing mechanisms vary substantially with soil type, compaction, and moisture condition, making it difficult to apply a single uniform model across different dam fills (Shan et al. 2023).

Stein and LaTray (2002) provided one of the key mechanistic foundations for this interpretation by developing a headcut migration model that combines cantilever mass failure of an overlying cohesive layer with scour-hole development in the underlying erodible material. Their results showed that the model reproduced observed retreat behavior of stratified soils with an average error of about 40 percent. Stein and Tray (2002) also found that retreat was nearly linear over time in the tested cases, supporting the idea that headcut migration can proceed as a repeating sequence of scour and failure events rather than as a smooth, continuous process. At the same time, their results showed that prediction error increased when scour-hole geometry became harder to characterize accurately, indicating that model performance was strongly tied to how well the erosional cavity shape was represented (Stein and LaTray 2002).

Later work extended these ideas into the context of cohesive embankment breach modeling. Zhao et al. (2012) described headcut development on a breach slope as a mixed process of particle erosion and mass failure and proposed a moment-equilibrium-based method for simulating headcut migration in overtopping-induced cohesive embankment breaches. Their formulation explicitly linked headcut advance to toe erosion and block instability, emphasizing that migration occurs when toe erosion removes sufficient support for a potential failure block (Zhao et al. 2012). Zhao et al. (2012) also validated the model against 14 laboratory tests and reported that predicted migration rates were generally slightly lower than measured values, although the agreement was considered reasonable given the variability of the materials. That result is significant because it shows that physically based headcut models can reproduce the overall trend and timing of erosion development even when they do not match every measured point exactly (Zhao et al. 2012).

Allen et al. (2018) synthesized a broader body of work on headcut advance and distinguished between mechanistic models and empirical models. They noted that mechanistic models commonly build on physically based representations of mass, momentum, and energy transfer near the scour hole, including the jet-impingement and undercutting concepts developed by earlier studies, such as Stein and LaTray (2002). By contrast, empirical approaches generally relate headcut retreat to more easily measured variables such as drainage area, rainfall, discharge, headcut height, and soil resistance factors (Allen et al. 2018; Rengers and Tucker 2014). Allen et al. (2018) found that a simplified headcut advance model could predict long-term gully headcut growth with reasonable accuracy across contrasting landscapes, even though it relied on relatively few input variables. Their results showed that the model performed better for some gullies than others, with stronger agreement where vegetation and channel conditions were more favorable and larger errors where local disturbances or denser vegetation complicated the retreat pattern (Allen et al. 2018). Allen et al. (2018) also found that sensitivity to input parameters varied substantially, with root-cover effects and erodibility-related terms exerting a stronger influence on predictions than headcut height in some cases.

Overall, the literature suggests that headcut progression is best understood as a variable, staged process in which model usefulness depends less on perfect numerical matching and more on whether the predicted results agree with observed behavior in a physically reasonable way (Zhao et al. 2012; Allen et al. 2018; Rengers and Tucker 2014).

2.5 Sensitivity Studies

The previous discussion highlighted significant uncertainties in many of the input parameters for the erosion models under consideration. To quantify this, this study uses a formal sensitivity analysis to understand how uncertainty in model inputs propagates into model outputs. Saltelli et al. (2004) define sensitivity analysis as the study of how uncertainty in a model's output can be apportioned to different sources of uncertainty in the model's inputs, providing a foundation for model evaluation studies. Frey and Patil (2002) similarly explain that sensitivity analysis can help identify critical inputs, prioritize additional data collection or research, and support model verification and validation. In environmental and hydraulic modeling, these objectives are especially important because models often include many uncertain parameters, nonlinear behavior, and threshold responses, which complicate the interpretation of simulation results (Song et al. 2015).

A common distinction in literature is between local and global sensitivity analysis methods (Saltelli et al. 2004; Frey and Patil 2002). Saltelli et al. (2004) explains that local sensitivity analysis has traditionally been defined in terms of derivatives that measure the effect of a given input on a given output at a specified point in parameter space. They also caution that local methods are often used inappropriately when the factors vary over finite ranges, because these methods do not adequately account for multidimensional averaging or interaction effects across the full domain of interest (Saltelli 1999). Frey and Patil (2002) make a similar point, explaining that nominal or local methods are most valid for linear models and can be misleading for nonlinear models in which interactions among inputs are important. For that reason, global methods are generally preferred when the goal is to understand uncertainty spread across the full space of plausible parameter values rather than only near a nominal point (Pianosi et al. 2016).

Saltelli et al. (2004) further argues that an effective global sensitivity method should account for the scale and shape of the input distributions, include multidimensional averaging, remain model-independent, and be capable of capturing interaction effects. This perspective is especially relevant to computational hydraulics and breach modeling, because uncertainty may arise not only from parameter magnitudes but also from assumptions about ranges, distributions, and model structure (Wahl 2001; Neilson and Cao 2019). Frey and Patil (2002) also emphasize that no single sensitivity method is universally best, and that the most appropriate method depends on the model form, the analysis objective, and the computational effort that can be afforded.

Saltelli et al. (2004) distinguishes between settings such as factor prioritization, factor fixing, variance cutting, and factor mapping. The choice of methods should match the question being asked in the study design. For example, if the goal is to identify non-influential parameters that can be fixed without materially affecting output uncertainty, screening-oriented methods are appropriate. If the goal is instead to quantify the share of total response uncertainty attributable to each parameter and its interactions, variance-based methods are more appropriate (Saltelli et al. 2004). Frey and Patil (2002) make a similar point by noting that sensitivity analysis may be conducted to identify key inputs, understand model behavior, support validation, or evaluate the robustness of model-based conclusions, and each purpose may favor a different analytical technique.

Parameter sweep methods are used when the same model must be run repeatedly across many combinations of input values to explore how the model response changes across the parameter space (Bach 2021; Smanchat et al. 2013). A parameter sweep is commonly defined as a collection of independent tasks, each executed with a different set of parameters, so that the total workflow can be parallelized across available resources (Casanova et al. 1999). This makes parameter sweeps especially useful for computational studies where the underlying model is expensive to evaluate, and the analyst wants to inspect broad behavioral trends rather than compute a single calibrated answer (Samples et al. 2005).

Grid-based parameter sweeps are also closely linked to workflow scheduling because each parameter combination often corresponds to one or more simulation runs that must be dispatched, monitored, and collected efficiently (Huedo et al. 2004;

Smanchat et al. 2013). Huedo et al. (2004) showed that parameter sweep applications are naturally suited to heterogeneous distributed environments because the tasks are largely independent, but they also noted that file sharing, transfer cost, and resource variability strongly affect performance. Casanova et al. (1999) similarly emphasized that the main scheduling challenge is not task dependence but the efficient assignment of many independent experiments to heterogeneous resources under changing load conditions. In other words, the computational problem is not a single simulation, but the orchestration of many simulation instances across a space of parameter values (Casanova et al. 1999; Huedo et al. 2004).

The use of multidimensional parameter-space exploration has also become common in fields where model evaluations are expensive, and the objective is to understand how outputs vary over a large space of physically meaningful parameters (Arguelles et al. 2023; Evers and Linsen 2022). Arguelles et al. (2023) describes a strategy for efficiently exploring multidimensional parameter spaces by reducing the number of expensive simulations needed to build a predictive view of the model response, which reflects the same motivation behind parameter sweeps in simulation studies. Evers and Linsen (2022) similarly frame multidimensional analysis to represent how parameter combinations influence output behavior across a large space, reinforcing the idea that a grid or sweep is often used for interpretability rather than solely for statistical estimation.

Dakota provides a software framework that operates these sensitivity and uncertainty analysis concepts by coupling iterative analysis methods to an external simulation model (Adams et al. 2009; https://snl-dakota.github.io/docs/6.22.0/users/index.html). Dakota describes uncertainty quantification as the process of characterizing uncertain inputs, propagating them through a computational model, and performing a statistical assessment of the resulting outputs. In this framework, uncertain inputs are mapped through the simulation model, enabling the estimation of statistics, intervals, and other output metrics from repeated model evaluations. Dakota's multidimensional parameter study evaluates models on an n-dimensional grid, formed by partitioning each uncertain variable into equally spaced intervals between its lower and upper bounds, then running the model at each resulting grid point (Adams et al. 2022). This makes the method a structured parameter sweep rather than a random sampling approach, so it is especially useful for exploring response surfaces, thresholds, and combined effects across a small to moderate number of uncertain inputs (Adams et al. 2022).

In breach modeling workflow, Dakota does not replace the governing hydraulic, erosion, or breach simulator. Instead, it manages the repeated execution of that simulator under systematically varied input conditions. In the WinDAM C implementation described by Neilsen and Cao (2019), Dakota was used to define variables, interfaces, models, and iterators, so that sampled input values could be passed automatically to the simulation model and the resulting outputs collected for post-processing. This type of architecture is well-suited to dam safety studies because it enables large ensembles of breach or erosion simulations to be executed in a controlled, reproducible manner for parameter studies, uncertainty propagation, and sensitivity analysis (Neilsen et al. 2015).

2.6 Summary

This chapter reviewed the physical mechanisms, experimental findings, mitigation measures, and modeling approaches relevant to overtopping-induced breach formation of cohesive earth embankments, with emphasis on headcut initiation, upstream migration, and the roles of soil properties and vegetation in controlling erosion resistance. The review shows that cohesive-soil breach evolution is governed by τ_c, k_d, s_u, and geomorphic/hydraulic drivers (slope, drop height, unit discharge), while new treatments such as biopolymer stabilization can substantially increase τ_c and s_u and reduce k_d, but lack full-scale validation and standardized approaches to incorporate them into breach models.

CHAPTER 3: Research Methods

3.1 Modeling Approaches

A wide range of numerical programs and modeling frameworks has been developed to simulate dam breaching and associated failure mechanisms, including overtopping and internal erosion scenarios (Peeters et al. 2011; Chenyi et al. 2025; Cook et al. 2015). Prominent examples include WinDAM C, DLBreach, EMBREA, BEED, FIREBIRD BREACH, DSS-WISE, and BASEBreach. These tools differ substantially in their physical representations, computational complexity, data requirements, and suitability for specific dam types and failure processes. Existing models span a spectrum from empirical and parametric approaches to fully physically based, process-driven simulations. While some platforms, such as FIREBIRD BREACH and DSS-WISE, emphasize advanced hydrodynamics or large-scale flood mapping, they do not explicitly account for differences between cohesive and cohesionless soils, limiting their applicability for earthen embankment breach analysis (Morris et al. 2012; Al-Hamdan et al. 2021).

Empirical methods rely on statistical analyses of historical dam failure data to estimate key breach parameters, including breach width, formation time, and peak outflow (Wahl 1998). Widely used empirical relationships include those developed by MacDonald and Langridge-Monopolis (1984), Froehlich (1995), and the U.S. Bureau of Reclamation (1988). Building on these relationships, parametric models provide an efficient means of predicting breach characteristics by incorporating empirically derived equations (West et al. 2018). Due to their computational efficiency and minimal data requirements, parametric models are well-suited for rapid assessments (Wahl 1998), with DAMBRK and FLDWAV serving as common examples.

In contrast, physically based numerical models simulate overtopping-induced breach processes by coupling hydraulic flow, sediment transport, and soil erosion (Hunt et al. 2021; Wu 2016). These models typically represent breach geometry using simplified cross-sectional shapes, such as trapezoids, and compute outflow discharge using modified broad-crested weir equations that account for upstream slope effects (Zhang et al. 2025). Many of these models have been validated against laboratory and field observations involving cohesive and noncohesive, homogeneous and composite embankments, demonstrating strong agreement in predicting breach width, outflow hydrographs, and failure timing (Wu 2013; Zhang et al. 2025). Representative examples include WinDAM C, DLBreach, and EMBREA.

Complementing these approaches, risk models provide a probabilistic framework for estimating the likelihood of dam overtopping by incorporating uncertainties in key variables such as reservoir water level, flood magnitude, wind conditions, and dam geometry (Sun et al. 2012). These models support dam safety management by enabling quantitative risk assessments and informing emergency planning decisions.

Based on an evaluation of available modeling approaches, WinDAM C and DLBreach were selected for this study. Both models offer robust, user-friendly interfaces and incorporate physically based erosion processes appropriate for homogeneous earthen embankments. Additionally, they allow for detailed investigation of soil erodibility parameters and the temporal evolution of breach geometry, making them well-suited to the objectives of this research.

3.1.1 WinDAM C

WinDAM C (Visser et al. 2024; https://www.nrcs.usda.gov/resources/tech-tools/windam-version-1115) is a modeling software developed by the USDA-NRCS to simulate erosion and breach processes in earthen embankments subjected to overtopping or internal erosion events (Hunt et al. 2021). The model routes an external hydrograph through a reservoir system, supporting one principal and up to three auxiliary or emergency spillways. For determining erosion resistance, WinDAM C incorporates dam surface protection options such as bare soil, vegetation, or riprap, and uses erodibility parameters to simulate headcut development and breach progression. The software requires geometric parameters (crest width, slope), hydraulic conditions (inflow hydrograph, reservoir levels), and soil properties (grain-size distribution, Atterberg Limits, τ_c, k_d, and s_u). WinDAM C uses both the Temple/Hanson energy-based model and the Hanson/Robinson stress-based model to capture headcut migration. The Temple/Hanson model requires an advanced coefficient (AC), whereas the Hanson/Robinson model requires input parameters including γ_T and s_u. Validation of WinDAM C has included comparison with physical model tests of overtopping and internal erosion scenarios (Hanson et al. 2005).

WinDAM C represents overtopping erosion using a staged sequence. In the model, Stage 1 is defined by vegetation failure and initial soil exposure, controlled by the vegetal cover factor, retardance curve index, and critical shear stress. In Stage 2, WinDAM C simulates progressive lowering of the downstream crest, with the downcutting rate controlled by k_d, while a headcut forms and begins to migrate in response to either the AC in the energy-based formulation or the combination of γ_T and

s_u in the stress-based formulation. In Stage 3, the model initiates breach widening, again governed by k_d, once the eroded downstream crest intersects the embankment's downstream toe, signaling that the breach will enlarge laterally as erosion continues. Finally, Stage 4 continues headcut retreat and breach widening until the embankment is entirely eroded.

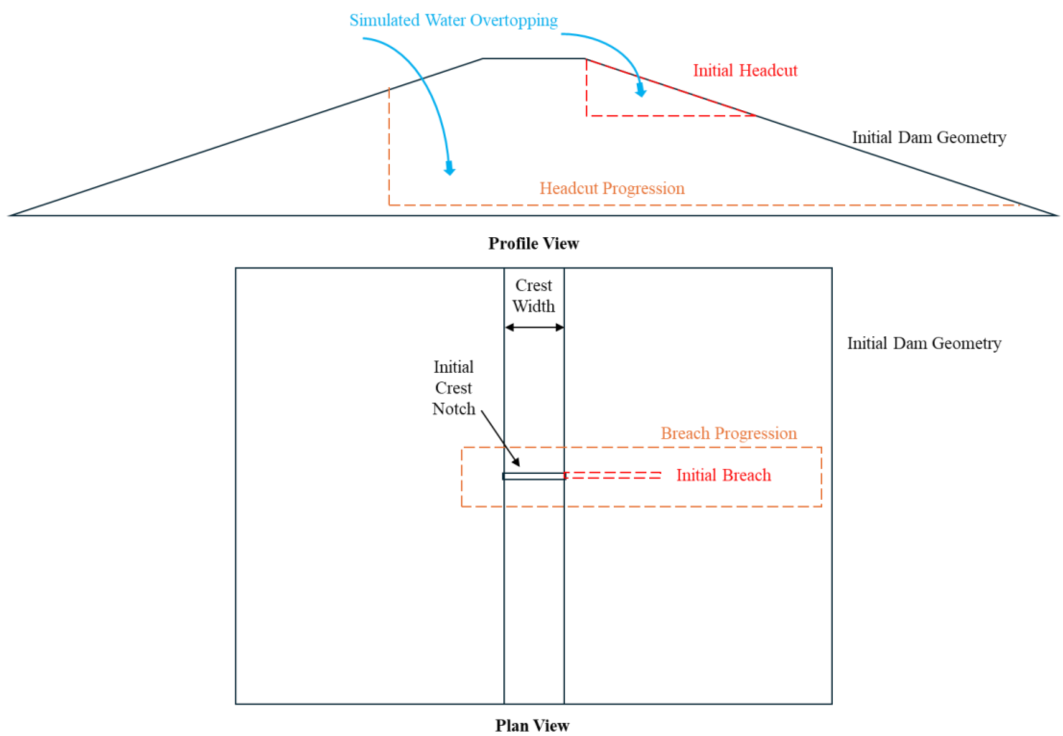

Figure 6. WinDAM C simulation illustrates the temporal progression of headcut migration and breach widening at matched time intervals for the embankment overtopping scenario.

3.1.2 DLBreach

The DLBreach model (Wu 2016; https://webspace.clarkson.edu/~wwu/DLBreach.html) is a simplified physically based numerical tool for simulating dam and levee breach processes due to overtopping or piping, accommodating different embankment types, including non-cohesive, cohesive, and clay-core structures. The model is intended for bare-soil embankments and does not account for vegetation presence or effects. The model represents embankments with a trapezoidal cross-section and offers both one-directional (dams/levees) and two-directional (coastal structures) breach simulations, incorporating physical erosion processes and key hydrodynamic feedback among breach formation, flow, sediment transport, and breach morphology evolution. It divides breaching into intensive and general evolution phases, applying a broad-crested weir equation for supercritical breach flows and wind forcing for subcritical flows during the general evolution phase. Erosion processes differ for non-cohesive and cohesive embankments and can include surface erosion, headcut migration, and composite core erosion. The breach side slopes are dynamically modeled using stability theory, and morphological changes are allocated based on slope stability and sediment supply. DLBreach offers several options for modeling headcut erosion, as well as surface and clay-core erosion. The clay core simulation combines surface erosion and headcut erosion at the clay core. DLBreach also specifies sediment as cohesive or non-cohesive to utilize detachment rate equations or sediment transport equations. DLBreach requires a single text input file specifying all geometric, hydraulic, and sediment parameters with broad support for custom inflow, outflow, spillway, and gate controls. Upstream/downstream storage routing is based on user-provided stage-area and stage-storage curves, or on power-law approximations. Outputs include time series of breach discharge, breach evolution (including widths and elevations), water levels, cumulative volumes, and sediment fluxes, which are validated against laboratory and historical field case data (Wu 2016).

DLBreach does not explicitly describe the headcut-erosion sequence in the user manual for cohesive embankments, but the model outputs, governing equations, and schematic graphics together clarify how overtopping erosion is represented. Failure initiation is assumed to begin at the downstream toe, where headcutting develops and migrates upstream. As this headcut retreats, the program also assumes a vertical downstream face that widens simultaneously according to

$$\Delta b = a_c \, n_{loc} \, \Delta x \qquad (1)$$

where Δb is the breach widening rate (m/hr), a_c is a proportionality coefficient taken as 0.165, n_{loc} indicates whether erosion occurs only on the downstream slope face (n_{loc} = 1) or on both downstream and upstream faces (n_{loc} = 2), and Δx is the headcut advance rate, representing the rate at which the downstream toe migrates upstream (m/hr). Although Δb and Δx are not directly reported, Δb can be inferred from the time series of breach width in the model output, to then solve for Δx, while concurrent overtopping erosion at the crest progressively lowers the dam crest elevation.

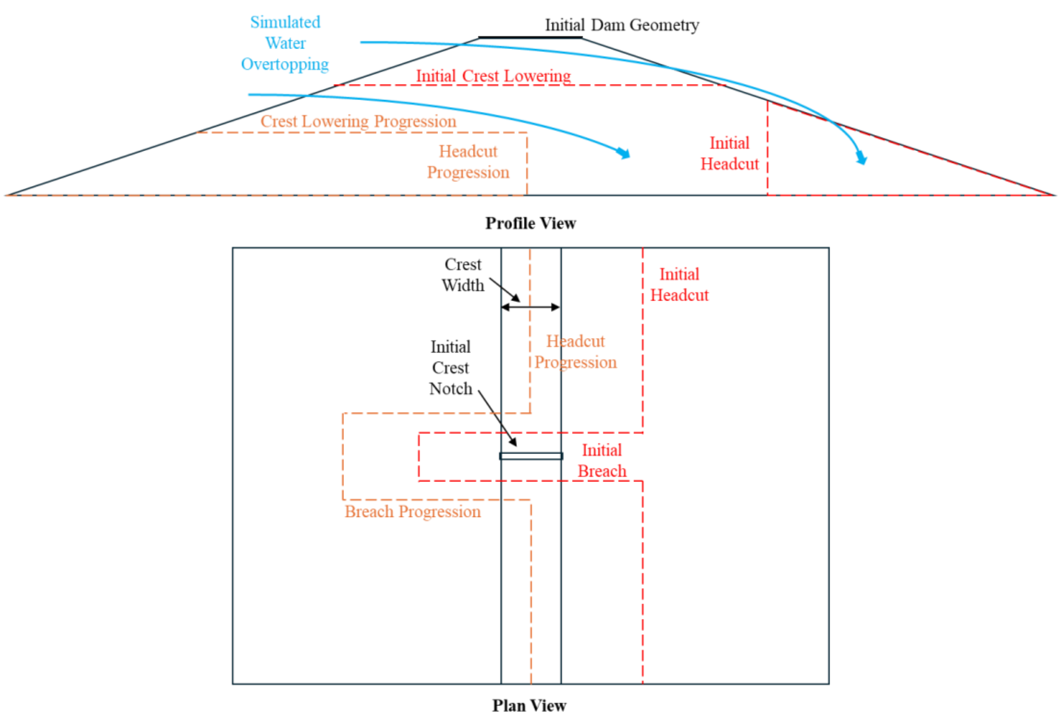

Figure 7. Simultaneous progression of headcut migration and breach widening during overtopping as modeled by DLBreach (Wu 2016).

3.1.3 Input Properties

Modeling in WinDAM C and DLBreach requires a set of essential input parameters to accurately simulate overtopping-induced erosion, summarized in Table 1.

Table 1. Table of input parameters, including symbol, source program, modeled quantity or function, and units.

Parameter Name	Symbol	Program	Use	Units
Embankment Height	H	WinDAM C and DLBreach	Defines the height of embankment being modeled	WinDAM C - ft DLBreach - m
Embankment Length	L	WinDAM C and DLBreach	Defines the length along the centerline of the crest of the dam	WinDAM C - ft DLBreach - m
Crest Width	W	WinDAM C and DLBreach	Defines the width between upstream and downstream crest	WinDAM C - ft DLBreach - m
Side Slopes	S	WinDAM C and DLBreach	Defines the slope ratio of the upstream and downstream embankments	WinDAM C - H:V DLBreach - V:H
Erodibility	k_d	WinDAM C and DLBreach	Rate at which soil detaches once erosion begins	WinDAM C - ft^3/lb-hr DLBreach - cm^3/N-s
Critical Shear Stress	τ_c	WinDAM C and DLBreach	Influences timing of breach initation	WinDAM C - psf DLBreach - Pa
Advanced Coefficient	AC	WinDAM C (Energy Model)	Affects the progression of dam headcut erosion resulting from overtopping water flow	$(ft/hr)/(ft/s^{1/3})$
Total Unit Weight	γ_T	WinDAM C (Energy Model)	Driving force for mass failure of the headcut	pcf
Undrained Shear Strength	s_u	WinDAM C (Stress Model)	Resistance of mass failure to headcut	psf
Cohesion	c	DLBreach	Affects embankment stability for breach side slopes and headcut	Pa
Failure Mode		DLBreach	Decides whether erosion is due to overtopping or piping	1-Overtop 2-Piping
Erosion Mode		DLBreach	Defines whether erosion is surface, headcut, or combination (clay core)	1-Surface Erosion 2-Headcut 3-Clay Core
Manning's n	n	WinDAM C and DLBreach	Represents resistance of soil to water flow	WinDAM C - applied to effective stress equation to the erodible boundary DLBreach - input is a direct measurement
Retardance Curve Index	RCI	WinDAM C	Represents resistance of vegetation to water flow	Unitless
Maintenance Code		WinDAM C	Describes the uniformity of cover for the vegetation along the surface of the embankment	1-Uniform 2-Minor Discontinuities 3-Major Discontinuities
Initial Breach		WinDAM C and DLBreach	Initial notch in the downstream crest	WinDAM C - manually defined when creating the dam crest profile DLBreach - direct input
Breach Location		DLBreach	Describes whether breaching starts in the middle of the embankment length or off to one side	1-breach on one side 2-breach in the middle
Dam Base Elevation		WinDAM C and DLBreach	Defines the datum of the dam being modeled	WinDAM C - ft DLBreach - m
Sediment Type		DLBreach	Determines whether to use sediment transport or detachment rate equations in erosion analysis	1-noncohesive (sediment transport) 2-cohesive (detachment rate)
Particle Diameter	d_{50}	WinDAM C and DLBreach	Affects the resistance of soil to erosion and breach iniation	WinDAM C - in DLBreach - m
Plasticity Index	PI	WinDAM C	Affects breach iniation	Unitless
Vegetal Cover Factor	VCF	WinDAM C	Value that limits the erosion effective stress due to vegetation	Unitless
Friction Angle	φ	DLBreach	Affects embankment stability for breach side slopes and headcut	$\tan(\varphi)$
Headcut Model		DLBreach	Determines which headcut advance rate equation will be utilized for analysis	1-USDA NRCS 1997 2-Temple 1992 3-Temple et al. 2005
Reservoir Stage Storage		WinDAM C and DLBreach	Specification of reservoir volume or area with rising water level elevation	WinDAM C - Imperial DLBreach - SI
Initial Upstream and Downstream Water Level		DLBreach	Specify the water elevation upstream and downstream of the dam before analyses	m
Hydrograph Inflow		WinDAM C and DLBreach	Describes the water inflow discharge with time during simulation	WinDAM C - hr, cfs DLBreach - hr, cms
Spillway Option		WinDAM C	Select if principal spillway is present	
Downstream Tailwater Outflow/Elevation		WinDAM C and DLBreach	Describes the outflow of water past the embankment	WinDAM C - Imperial DLBreach - SI
Auxiliary Spillway Option		WinDAM C	Select if auxiliary spillways are present	

Several of the parameters listed in the table, specifically the VCF, RCI, n, AC, k_d, and τ_c, warrant additional clarification due to their substantial influence on predicted erosion outcomes and their derivation via empirical relationships. Unlike purely geometric or directly measured properties, these parameters incorporate complex interactions between soil, hydraulic, and vegetative characteristics or rely on laboratory-to-field extrapolation. As these parameters are central to simulating embankment erosion processes in both WinDAM C and DLBreach, further explanations of their physical meanings, sources, and applicability are provided below.

3.1.3.1 Retardance Curve Index

The RCI is a vegetation-based roughness index that represents the cumulative flow resistance created by stem height, stem density, and vegetation type (Temple et al. 1987). In WinDAM C, RCI is used to characterize the hydraulic resistance of vegetated surfaces. Manning’s n is related to this resistance through the vegetation-retardance formulation rather than being treated as an independent input (USDA 2021). In this way, Manning’s n is embedded within the RCI concept as the hydraulic expression of vegetation effects on flow resistance (Temple et al. 1987). This means that RCI represents the vegetated condition, while Manning’s n is the flow-resistance quantity that translates that vegetation into hydraulic behavior (USDA 2021). For flow resistance specification, WinDAM C links RCI to Manning’s n through a regression model expressed:

$$n = e^{RCI\left[0.01331(n^2)(q) - 0.09541(n)(q) + 0.297\right] - 4.16} \quad (2)$$

where $0.0025RCI^{2.5} \leq q \leq 36$, where q is the unit discharge over the headcut (cfs/ft) (USDA 2014). For bare soil, this vegetation-based relationship is not used, and

WinDAM C applies a fixed roughness value (n = 0.02) for exposed embankment surfaces (USDA 2014). Analytical estimation of RCI employs the relation shown (Temple 1982):

$$RCI = 2.5(h\sqrt{M})^{1/3} \tag{3}$$

where h is vegetal stem length (ft) and M is stem density (stems/ft²). Empirically derived RCI values for typical grass species are categorized into retardance classes (A–E), as detailed in Table 2.

Table 2: Retardance classes of various vegetal covers and their corresponding retardance curve index values (USDA 2021).

RCI	Retardance Class	Covers Tested	Condition
10.000	A	Weeping Lovegrass	30" tall
		Reed Canarygrass	36" tall
7.640	B	Bromegrass	Mowed 12-15" tall
		Bermudagrass	12" tall
		Native Grass Mixture	Unmowed
		Tall Fescue	18" tall
		Sericca Lespedeza	19" tall
		Orchardgrass	20" tall
		Reed Canarygrass	12-15" tall
		Blue Grama	13" tall
5.600	C	Bahiagrass	6-8" tall
		Bermudagrass	Mowed 6" tall
		Redtop	15-20" tall
		Grass-Legume Mixture	6-8" tall
		Cenntipedegrass	6" tall
		Kentucky Bluegrass	6-12" tall
4.440	D	Bermudagrass	Mowed 2.5" tall
		Red Fescue	12-18" tall
		Buffalo Grass	3-6" tall
		Grass-Legume Mixture	4-5" tall
		Kentucky Bluegrass	Mowed 2" tall
2.880	E	Bermudagrass	Mowed 0-1.5" tall

3.1.3.2 Vegetal Cover Factor

The VCF is an empirical parameter describing the potential of the vegetal cover to dissipate turbulent currents in the immediate vicinity of the hydraulic stress boundary (Temple 1980). Within WinDAM C, the effective hydraulic shear stress acting on the soil surface is adjusted as described by (USDA 2014):

$$\tau_e = \tau_o(1 - VCF)(\frac{n_s}{n})^2 \tag{4}$$

where τ_e is the effective stress on the erodible boundary, τ_o is the gross hydraulic stress on the spillway surface, n_s is the soil grain roughness of the erodible boundary, and n is the gross roughness (Manning's n) for the spillway (USDA 2014). Typical VCF values range approximately from 0.5 to 0.9 for various grasses, as illustrated in Table 3.

Table 3: Stem densities of tested grass types along with their associated vegetal cover factors (USDA 2021).

VCF	Covers Tested	Stem Density (stem/ft^2)
0.900	Bermudagrass	500
	Centipedegrass	500
	Buffalo Grass	400
0.870	Kentucky Bluegrass	350
	Blue Grama	350
	Bromegrass	210
0.750	Native Grass Mixture	200
	Weeping Lovegrass	350
	Reed Canarygrass	250
0.500	Sericca Lespedeza	300

3.1.3.3 Manning's n

DLBreach requires the direct input of n, which encapsulates flow resistance due to surface roughness and bed irregularities. Within DLBreach, n is approximated relative to sediment median grain size (d_{50}, m):

$$n = A_n d_{50}^{1/6} \tag{5}$$

where A_n is an empirical coefficient reflecting bedform development and sediment characteristics, ranging typically from 10 to 20 (Wu 2007). For cohesive sediments, Wu (2016) recommends using a fixed value n = 0.016. DLBreach has been validated specifically with this value, and the manual's examples use it exclusively. Although DLBreach permits other Manning's n values, users must explicitly specify n in the input file rather than relying on Equation 5.

3.1.3.4 Erodibility Index

In DLBreach, lateral breach widening is dynamically represented as a function proportional to the computed headcut migration rate. Calculation of K_h for the derivation of AC follows the procedures outlined by Moore et al. (1994):

$$K_h = M_s * K_b * K_d * J_s \tag{6}$$

where M_s is the material strength number, K_b is the particle size number (1 for intact soil), K_d is the discontinuity or interparticle bond shear strength number, and J_s is the relative ground structure number (1 for intact soil). M_s was estimated either by correlating with standard penetration test (SPT) blowcount or by using the UCS equation stated in USDA (2001). UCS could be estimated using this equation from Kormu et al. (2022):

$$UCS = -3105 + 1625 * MDD + 40.9 * OMC \tag{7}$$

where MDD is the maximum dry density (g/cm^3) and OMC is the optimum moisture content. K_d is evaluated as a function of the residual friction angle.

3.1.3.3 Advance Coefficient

The AC parameter was determined according to the procedures outlined by USDA (2001, 2014), briefly summarized below. For the analysis presented here, the USDA

(2014) formulation was adopted to ensure consistency and comparability of simulation results:

$$\frac{dx}{dt} = AC[(qH)^{\frac{1}{3}} - A_0] \tag{8}$$

$$\mathrm{AC} = \begin{cases} -0.79 lnK_h + 3.04 & K_h < 18.2 \\ 0.75 & K_h \geq 18.2 \end{cases} \tag{9}$$

$$A_0 = \begin{cases} 0 & K_h < 0.01 \\ [189K_h^{\frac{1}{2}} e^{-\frac{3.23}{\ln(101K_h)}}]^{1/3} & K_h \geq 0.01 \end{cases} \tag{10}$$

The governing equations (8, 9, and 10) relate the headcut advance rate (dx/dt, ft/hr), headcut erodibility index (K_h), unit discharge over the headcut (q, $ft^3/s/ft$), and overfall height (H, ft) to the AC.

3.1.4 Output Parameters

Output parameters from WinDAM C and DLBreach provide complementary descriptions of the overtopping-plus-breach processes, but only a subset is directly relevant to the objectives of this study. Here, attention is focused on a core group of hydrologic and geometric outputs that characterize breach initiation timing, reservoir response, and breach development, with the understanding that both models compute additional internal variables that are not explicitly analyzed. Time to erosion initiation and the corresponding upstream and downstream water surface elevations (WinDAM C: Water Surface Elevation and Tailwater Elevation; DLBreach: zs_upstr and zs_downstr) describe the hydraulic conditions under which overtopping transitions into active erosion. Breach geometry is tracked through head cut position, head cut base elevation, breach width (WinDAM C: Width; DLBreach: B_bottom and B_top), and the hydraulic control or breach bottom elevation (WinDAM C: Hydraulic Control; DLBreach: zb_breach), which together quantify the progression and deepening of the breach. Flow response is represented by unit discharge through the breach (WinDAM C: Unit Discharge; DLBreach: Qbreach) and total overtopping discharge, as well as the cumulative volume of water exiting the reservoir (DLBreach: Vol_watout). In DLBreach, the eroded breach area (Areabreach) provides an additional measure of erosion extent that excludes the original notch. These selected outputs are emphasized because they most directly link model predictions to physically observable quantities (breach onset, breach size, and outflow) used for comparison with experimental data and for assessing the relative performance of WinDAM C and DLBreach.

Table 4. Table of interested output parameters for this study, including which program, the definition, and the units.

WinDAM C Output Name	DLBreach Output Name	Definition	Units
Time	Time	Time erosion initiates	hr
Water Surf. Elevation	zs_upstr	Upstream water elevation during erosion	WinDAM C – ft DLBreach - m
Head Cut Station		Distance coordinate for head cut erosion into the embankment	WinDAM C - ft
Head Cut Base Elev.		Elevation of the bottom of the head cut	WinDAM C - ft
Tailwater Elevation	zs_downstr	Downstream water elevation during erosion	WinDAM C - ft DLBreach - m
Width	B_bottom; B_top	Notes the width of the breach	WinDAM C - ft DLBreach - m
Unit Discharge	Qbreach	The discharge coming through the breach	WinDAM C - $ft^3/(ft\text{-}s)$ DLBreach - m^3/s
Overtop Discharge		Total discharge coming over the top of the embankment	WinDAM C - ft^3/s
Hydraulic Control	zb_breach	Elevation of the bottom of the breach	WinDAM C – ft DLBreach - m
	Areabreach	The eroded area of the breach (excluding the original notch)	DLBreach - m^2
	Vol_watout	Total volume of water that has overtopped the embankment	DLBreach - m^3

3.2 Kang et al. (2021) Experiment

Kang et al. (2021) conducted full-scale overtopping experiments at the Andong River Experiment Center in South Korea to evaluate the erosion resistance of levees reinforced with a polysaccharide-based biopolymer blend. The study examined a treated and untreated embankment constructed from clayey sand soil. The d_{50} was 0.49 mm for the treated embankment and 0.47 mm for the untreated embankment. Both untreated and treated cases had plasticity indexes of 8. The embankments were 2.5 m high and 15 m long, with a 4 meter-wide crest and 2:1 (H:V) side slopes (Figure 8). The embankments were compacted to 92% relative compaction (γ_d = 1.9 g/cm^3). The treated embankment was sprayed with the biopolymer mixture to create a 5 cm-thick layer on its surface. Vegetation was established on both embankments before testing, so the primary difference was the biopolymer treatment.

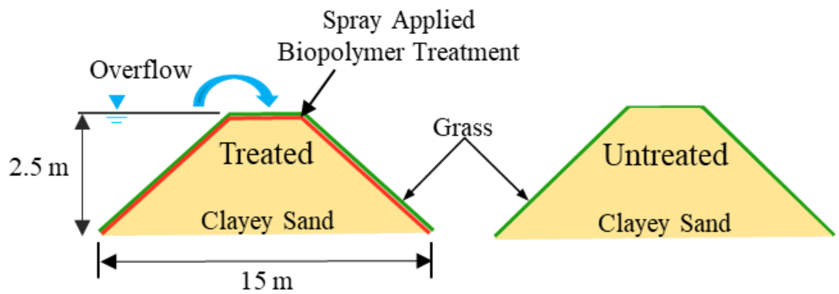

Figure 8. Embankment cross sections for the two embankments (after Kang et al. 2021).

Testing was performed by raising the water level behind the test embankment until overtopping occurred. The overflow volume was monitored using acoustic Doppler current profilers (ADCP), while surface erosion and breach development were quantified from drone imagery, which was post-processed to measure the percentage of pixels showing erosion. The results from the testing of the treated and untreated embankments are shown in Figure 9. The time to reach 20% surface loss was longer in the biopolymer-reinforced embankment (55 minutes) than in the untreated embankment (21 minutes). Similarly, the treated embankment required 63 minutes to reach an overflow discharge of 25 m^3/s, compared to only 23 minutes for the untreated case. This demonstrates that the biopolymer treatment successfully enhanced the embankment's erosion resistance.

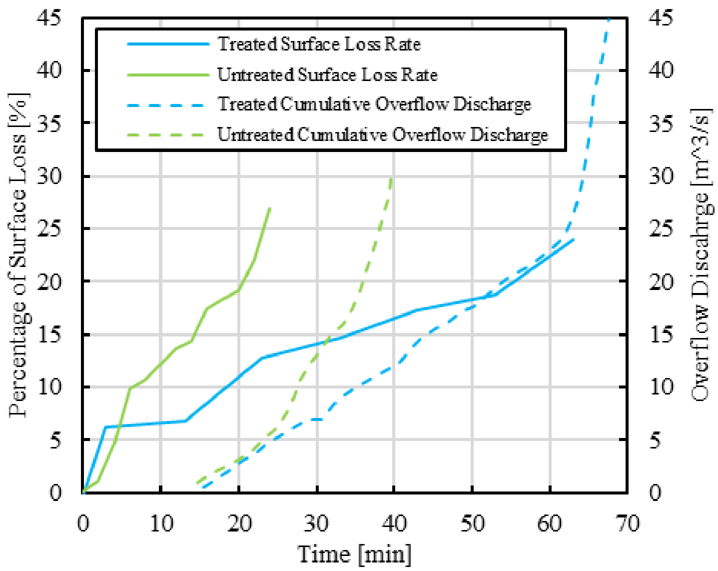

Figure 9. Overtopping performance of the treated and untreated embankments (after Kang et al. 2021).

3.2.1 Untreated Simulations

For the untreated embankment scenario, model input parameters were selected based on field conditions and published recommendations. Erodibility parameters, k_d and τ_c, were calculated using correlations from USDA (2014):

$$k_d = \frac{5.66 * \gamma}{\gamma_d} \exp[-0.121 * c_{\%}{}^{0.406} * \left(\frac{\gamma_d}{\gamma}\right)^{3.1}] \tag{11}$$

where γ is total unit weight, γ_d is dry unit weight, and c is the clay percentage. τ_c was estimated using a particle-size-based correlation recommended by the USDA (2014). The VCF was assigned a value of 0.500 in the WinDAM C framework; however, its impact could not be explicitly evaluated in this scenario. Because VCF primarily influences breach initiation timing, the experimental data from Kang et al. (2021) were available only post-breach. Within DLBreach, n was set to 0.016 in accordance with the default value recommended by Wu (2016), as no measured site-specific roughness data were available. In accordance with Equations 6-10 for calculating K_h and AC, the SPT N-value was estimated as 10 using the relative compaction method and d_{50}, following the correlation proposed by Cubrinovski and Ishihara (1999), since standard penetration test results were not available. This approach yielded M_s = 0.050. The soil friction angle was assumed to be 32°, consistent with a clayey sand classification, resulting in K_d = 0.620. Because the soil was considered intact and no particle-size changes occurred during the experiment, K_b and J_s remained constant at 1.

Initial simulations for the untreated case utilized the full baseline parameter set (Table 5) providing representative reference conditions for model calibration and validation. Parameters were then systematically varied to improve the agreement between simulated outcomes and experimental observations of breach evolution. This approach enabled the identification of key input sensitivities and the refinement of model fit for subsequent comparative analyses, as presented in Chapter 4.

Table 5: Key Model Parameter Values for Untreated Correlation Simulation.

Parameter	Value	Method/Equation	Reference
VCF (vegetal cover factor)	0.500	Estimated based on vegetation	USDA (2021)
k_d (erodibility coefficient)	7.630 $cm^3/N\text{-}s$	Equation 11	USDA (2014)
τ_c (critical shear stress)	0.140 Pa	Estimated based on particle diameter	USDA (2014)
K_h (erodibility index)	0.030	Equation 6	Moore (1997)
AC (advance coefficient)	5.780	Equation 9	USDA (2014)
γ_T (total unit weight)	2.160 g/cm^3	Given	Ko et al. (2021)
s_u (undrained shear strength)	39.500 kPa	Assumed	Zhang et al. (2009)
Manning's n	0.016	Recommended by DLBreach Manual	Wu (2016)

3.2.2 Biopolymer-Treated Simulations

The biopolymer treatment evaluated in the study by Kang et al. (2021) was applied as a 5-cm-thick surface layer over the embankment, resulting in spatial heterogeneity of soil properties, as the amendment is not expected to affect the underlying fill at depth.

However, the current modeling framework requires specification of homogeneous input parameters for the entire embankment cross-section. To address this, an equivalent set of composite erodibility parameters (k_d, τ_c, AC, s_u) was derived using a depth-weighted averaging approach that combined untreated soil properties (Table 5) with estimates for the treated zone obtained from equation 12.

$$Average = \frac{\sum_{i=1}^{n} Depth_i * Parameter_i}{\sum_{i=1}^{n} Depth_i} \tag{12}$$

For the biopolymer-amended surface, τ_c was increased by ~400% over the untreated baseline to 0.720 Pa, according to USACE JET data, while k_d was reduced by ~80% to 1.530 cm^3/N-s, consistent with laboratory observations for biopolymer-treated soils. The s_u for the treated material was set at 218.000 kPa, reflecting a ~450% increase, as reported by Ayeldeen et al. (2016) for a 2% XG content, relative to the baseline value reported by Zhang et al. (2009). Resulting composite parameter values were k_d = 7.510 cm^3/N-s, τ_c = 0.160 Pa, and s_u = 43.100 kPa. The AC, which is sensitive to both erodibility and soil structural evolution, was adjusted to 4.360 based on an increase in the material strength number M_s to 0.300, in line with the increased unconfined compressive strength observed for biopolymer-treated soils (Ayeldeen et al. 2016), with all other inputs for equation 6 held constant.

3.3 Breland et al. (2025) Experiment

ERDC researchers conducted a full-scale overtopping experiment using a split-embankment configuration (1.5-m crest height; 1:3 V:H side slopes; ~29-m total crest length) with four 7.3-m-long plots. Two plots were the control (untreated), and the other two were treated with Rhizobium tropici-derived exopolysaccharide biopolymer. The entire common test embankment was constructed of Vicksburg loess lean clay (Breland et al. 2025). Following a full growing season, independent limited-duration overtopping tests (October 2024) evaluated headcut initiation timing, early erosion volumes, and downstream toe scour development under controlled hydraulic loading, while a subsequent full breach test (November 2024) quantified complete headcut progression, crest lowering, and widening rates at ERDC's hydraulic test facility in Vicksburg, Mississippi. Performance across both test types was measured using LiDAR-derived surface change, embedded water-content/suction sensors, distributed acoustic sensing (DAS), electrical resistivity tomography (ERT), and visual/time-lapse observations to characterize biopolymer effects on antecedent moisture, erosion resistance, and headcut migration between treated and untreated sections.

(a) (b)

Figure 10. Post-overtopping condition of the embankment, illustrating the treated (a) and untreated (b) sections.

For the Breland et al. (2025) simulation series, three modeling cases were evaluated: a blind prediction, a breach-only simulation, and a combined overtopping-plus-breach simulation. Each of these used a different set of parameters, which are described in subsequent sections.

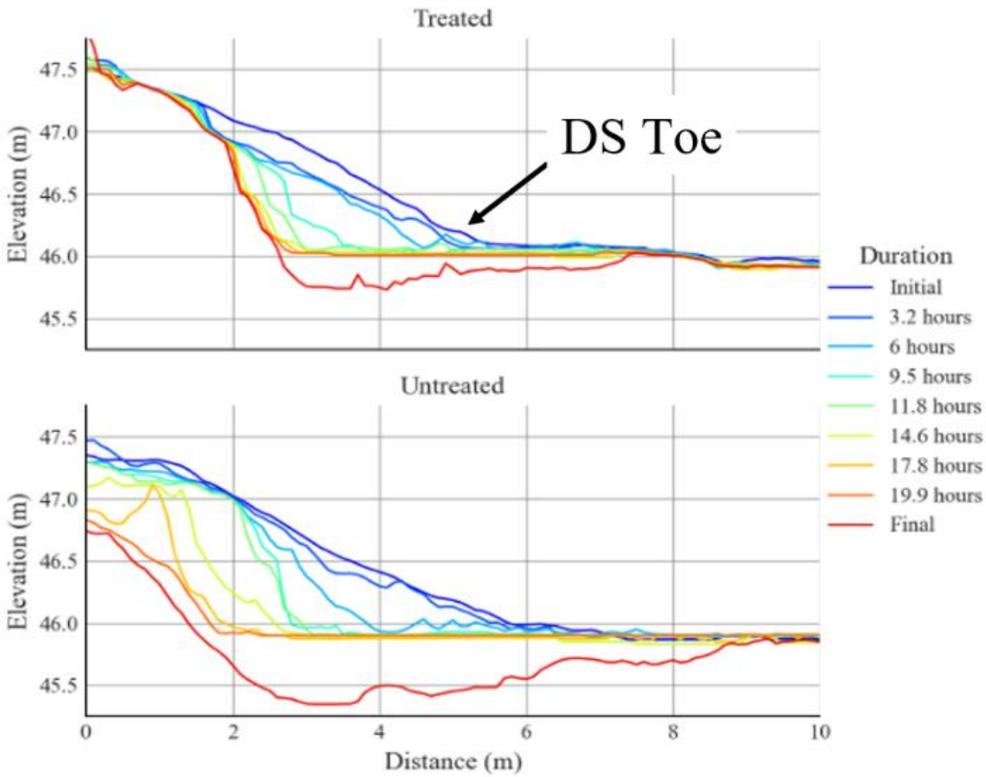

(a)

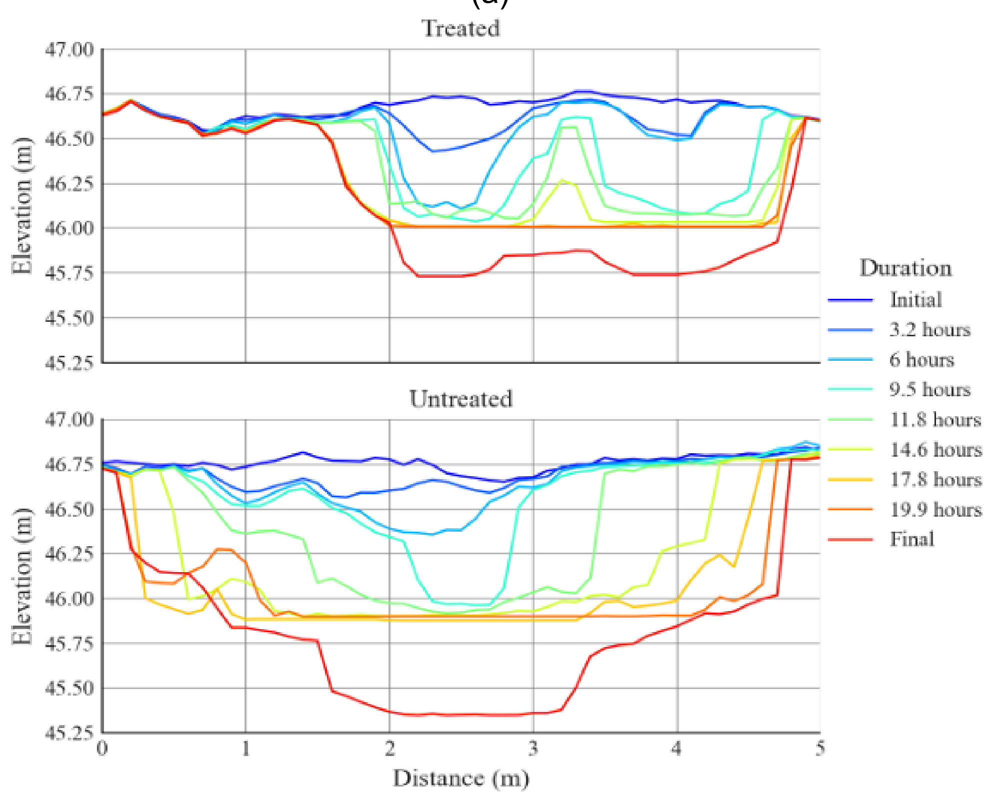

(b)

Figure 11. Observed headcut migration (a), lateral expansion, and deepening (b) with duration of overtopping for treated and untreated plots during the breach experiment (Breland et al. 2025).

3.3.1 Parameter Sets

Lab-observed soil and vegetative parameters for the untreated and biopolymer-treated conditions were derived from experimental data reported by Walshire et al. (2024) and supplemental ERDC laboratory testing. The k_d and τ_c were obtained directly from JET results for both the control and Rhizobium tropici-treated soils. Unit weight values were determined from ERDC compaction testing, while undrained shear strengths were adopted from Walshire et al. (2024). UCS values were then calculated for both untreated and treated samples from the corresponding s_u values (ASTM 2016). These UCS values yielded M_s = 0.044 for the untreated soil and M_s = 0.049 for the treated soil (USDA 2001). Friction angles of 31.7° and 29.8° were applied for the untreated and treated conditions, respectively, yielding K_d values of 0.620 and 0.570. K_b and J_s were both assumed to be 1 for each case. The resulting K_h was computed using Equation 6 to capture variations in unconfined compressive strength and friction angle across treatments, and the advance coefficient was subsequently determined using Equation 9. RCI was calculated as 3.800 (Equation 3) using a stem length of 3 inches (Walshire 2025, personal communication) and a stem density of 200 stems/ft², while VCF was assigned a value of 0.750 based on the native grass mixture described in Table 3. Within DLBreach, Manning's n was set to 0.016 in accordance with the default value recommended in the user manual. These parameters formed the baseline lab-observed input datasets for WinDAM C and DLBreach simulations, serving as the foundation for subsequent calibration and sensitivity analyses.

It is important to note that the lab-observed k_d and τ_c values deviate substantially from typical ranges for cohesive soils. JET and EFA data across cohesive soils show that k_d is typically <10 cm^3/N-s and τ_c >0.1 Pa for mass-erosion regimes (Ursic and Langendoen 2021). The Breland embankment's JET-derived parameters imply unexpectedly high erodibility.

Table 6: Lab-observed vegetation and soil input parameters for WinDAM C and DLBreach (untreated vs. treated).

Parameter	Untreated	Treated	Method	Reference
VCF (vegetal cover factor)	0.750	0.750	Table 3	USDA (2021)
RCI (retardance curve index)	3.800	3.800	Equation 3	USDA (2021)
k_d (erodibility coefficient)	35.840 cm^3/N-s	5.120 cm^3/N-s	Jet Erosion Test	ERDC (2024)
τ_c (critical shear stress)	0.140 Pa	0.490 Pa	Jet Erosion Test	ERDC (2024)
K_h (erodibility index)	0.027	0.028	Equation 6	Moore (1997)
AC (advance coefficient)	5.890	5.860	Equation 9	USDA (2014)
γ_T (total unit weight)	2.040 g/cm^3	1.750 g/cm^3	Compaction Test	ERDC (2024)
s_u (undrained shear strength)	36.000 kPa	39.000 kPa	Undrained Strength Test	(Walshire et al. 2024)
Manning's n	0.016	0.016	Recommended	Wu (2016)

Two additional parameter sets were developed to evaluate model sensitivity and calibration requirements. The correlated dataset retained all lab-observed values except k_d and τ_c, which were estimated using Equation 11, USDA (2014) correlations, and a depth-weighted average (Equation 12) for the treated case. This incorporated the observed ~80% reduction in k_d from biopolymer treatment (Walshire et al. 2024). These three datasets (lab-observed, correlated, best-fit) enabled direct comparison of model performance under progressively refined input conditions.

Table 7. Correlated vegetation and soil input parameters for WinDAM C and DLBreach (untreated vs. treated).

Parameter	Untreated	Treated	Method
VCF (vegetal cover factor)	0.750	0.750	Table 3
RCI (retardance curve index)	3.800	3.800	Equation 3
k_d (erodibility coefficient)	6.850 $cm^3/N\text{-}s$	6.300 $cm^3/N\text{-}s$	(USDA 2014)
τ_c (critical shear stress)	0.140 Pa	0.190 Pa	(USDA 2014)
K_h (erodibility index)	0.027	0.028	Equation 6
AC (advance coefficient)	5.890	5.860	Equation 9
γ_T (total unit weight)	2.040 g/cm^3	1.750 g/cm^3	Compaction Test
s_u (undrained shear strength)	36.000 kPa	39.000 kPa	Undrained Strength Test
Manning's n	0.016	0.016	Recommended

Table 8. Best-fit vegetation and soil parameters for WinDAM C: untreated vs. treated (overtopping-plus-breach experiment).

Parameter	Untreated	Treated
VCF (vegetal cover factor)	0.870	0.750
RCI (retardance curve index)	2.880	4.440
k_d (erodibility coefficient)	3.530 $cm^3/N\text{-}s$	3.250 $cm^3/N\text{-}s$
τ_c (critical shear stress)	0.140 Pa	0.340 Pa
AC (advance coefficient)	0.500	0.300
γ_T (total unit weight)	2.040 g/cm^3	1.750 g/cm^3
s_u (undrained shear strength)	33.500 kPa	35.900 kPa

3.3.2 Blind Prediction Simulations

In the blind-prediction case, the vegetated earth embankment model was run with assumed vegetation inputs, including VCF and RCI, and stem height was set to 3 inches because no site-specific grass information was provided. Erodible soil properties were taken from laboratory-observed data and USDA correlations (Equations 2-10; Tables 2 and 3). The reservoir storage curve was approximated from the source basin geometry provided by ERDC, even though the test basin was the actual basin behind the embankment. The source-basin inflow hydrograph was derived from volume and duration measurements recorded during the October 2024 overtopping experiments. All simulations are split into untreated and treated embankments, with the total reservoir and flow split evenly to represent the two sides of the test section.

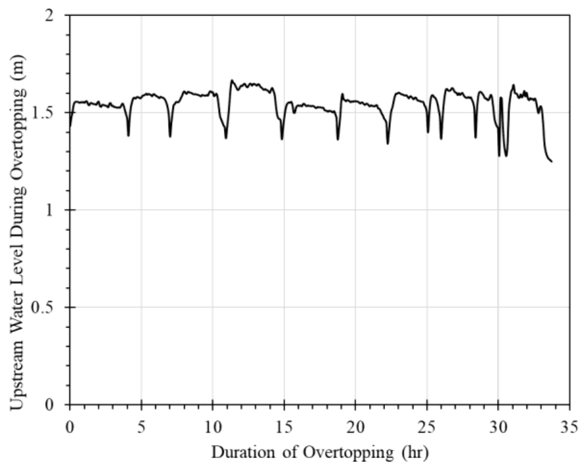

Figure 12. Water surface elevation versus time during the overtopping experiment (Breland et al. 2025).

3.3.3 Breach-Only Simulations

In the breach-only case, the model was informed by the Breland et al. (2025) breach experiment and used the directly provided flow data. This case assumed a bare-soil configuration with no vegetation resistance because the reported experiment results were normalized to 0 hours at the onset of erosion rather than tied to the actual elapsed time in the field test. The same laboratory-observed and USDA-correlated erodibility datasets were used, but the reservoir storage curve was updated from Figure 2-3 in Breland et al. (2025) to match the geometry behind the test embankment. As in the blind case, the reservoir and flow were split between the treated and untreated simulations.

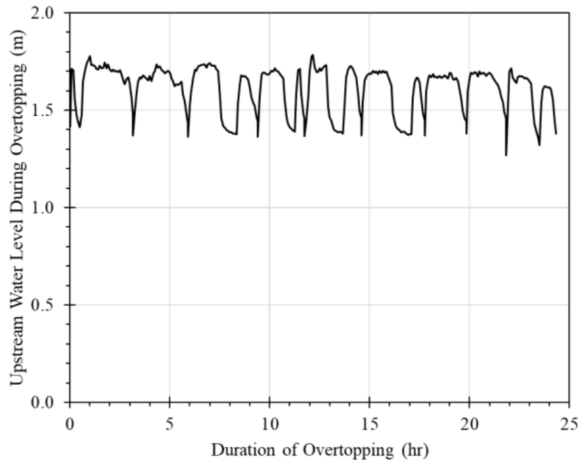

Figure 13. Water surface elevation versus time during the full breach experiment (Breland et al. 2025).

3.3.4 Overtopping-plus-Breach Simulations

In the combined overtopping-plus-breach case, the goal was to use all available information to assess how closely the simulations reproduced the observed response. This case used a vegetated embankment model with VCF and RCI, then expanded the soil-property set to include both the laboratory and correlated values, along with best-fit values for VCF, RCI, k_d, τ_c, AC, s_u, K_h, and Manning's n. The reservoir storage was taken from the breach experiment setup, again split equally between the treated and untreated simulations. The flow was combined from the blind and breach scenarios to represent the best available estimate of the test conditions. Together, these three cases allowed a comparison of failure initiation, breach development, and headcut progression under progressively greater amounts of observed information.

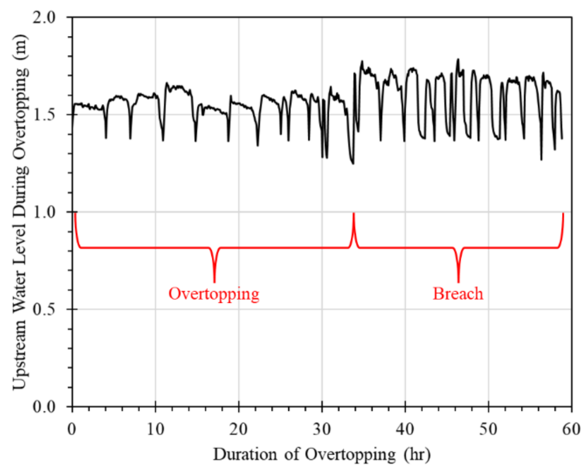

Figure 14. Water surface elevation versus time during combined overtopping and full breach experiments (Breland et al. 2025).

3.3.5 Dakota

A comprehensive parameter sensitivity study was conducted using Dakota (version 6.16; Adams et al. 2022; https://snl-dakota.github.io/docs/6.22.0/users/index.html), an open-source software framework for uncertainty quantification and parametric analysis developed by Sandia National Laboratories. The use of Dakota for breach model sensitivity analysis follows the approach established by Neilson and Cao (2019), who demonstrated its integration with WinDAM C and DLBreach for dam safety applications. The present study adapts that framework to assess how uncertainty in key soil and hydraulic parameters propagates through WinDAM C (energy- and stress-based) and DLBreach, specifically in the context of the Breland et al. (2025) embankment experiment involving biopolymer-treated cohesive soils.

Dakota's multidimensional parameter study was selected as the analysis method because it evaluates model responses on a structured, full-factorial grid across the specified ranges of all input parameters simultaneously. For a given number of variables x, each divided into p equally spaced partitions, the total number of model evaluations is:

$$(p + 1)^x \tag{13}$$

This approach generates a complete, reproducible exploration of the parameter space rather than a random sample, making it well-suited for identifying thresholds, response surface behavior, and combined parameter effects across a small to moderate number of uncertain inputs (Adams et al. 2022). A partition value of four was used for all Dakota runs, yielding five equally spaced evaluation points per variable between the specified lower and upper bounds.

Input parameters were selected based on their direct physical relevance to breach initiation, headcut advance, and breach widening in cohesive embankments, and their demonstrated sensitivity in prior calibration analyses (Sections 4.3-4.5). Three separate Dakota input files were configured, one for each model, with parameter sets reflecting the governing erosion physics of each formulation. Table 9 summarizes the input parameters and their bounds for each model.

Table 9. Parameter ranges used in the WinDAM-C Energy Model, WinDAM-C Stress Model, and DLBreach simulations.

Model	Parameter	Symbol	Lower Bound	Upper Bound
WinDAM C Energy Model	Erodibility Coefficient	k_d	0.700 $cm^3/N\text{-}s$	3.530 $cm^3/N\text{-}s$
	Critical Shear Stress	τ_c	0.140 Pa	0.490 Pa
	Manning's Roughness Coefficient	n	0.010	0.070
	Advance Coefficient	AC	0.100	0.500
WinDAM C Stress Model	Erodibility Coefficient	k_d	0.700 $cm^3/N\text{-}s$	3.530 $cm^3/N\text{-}s$
	Critical Shear Stress	τ_c	0.140 Pa	0.490 Pa
	Undrained Shear Strength	s_u	33.500 kPa	167.500 kPa
	Manning's Roughness Coefficient	n	0.010	0.070
	Total Unit Weight	γ_T	1.750 g/cm^3	2.040 g/cm^3
DLBreach	Erodibility Coefficient	k_d	0.700 $cm^3/N\text{-}s$	3.530 $cm^3/N\text{-}s$
	Critical Shear Stress	τ_c	0.140 Pa	0.490 Pa
	Manning's Roughness Coefficient	n	0.010	0.070
	Erodibility Index	K_h	0.020	0.030

Parameter bounds were defined to represent the full plausible range of each parameter for the Breland et al. (2025) embankment, spanning from the best-fit untreated condition (Table 8) to an assumed condition reflecting full biopolymer treatment. For parameters that decrease under biopolymer treatment (k_d, γ_T, AC, and n), the upper bound corresponds to the best-fit untreated value, and the lower bound corresponds to an assumed ~80% reduction. For parameters that increase under biopolymer treatment (τ_c and s_u), the bounds are reversed: the lower bound is set to the untreated best-fit value, and the upper bound is a ~400% increase. This bounding approach reflects the experimentally observed range of biopolymer effects on cohesive soil erodibility and strength documented in the literature (Kwon et al. 2020; Walshire et al. 2024). This ensures that the full parameter space between untreated and fully treated soil conditions is systematically explored.

Dakota was coupled to each breach model via a batch-file interface. At each parameter combination, Dakota wrote the sampled input values to a parameters file, executed the corresponding batch driver, and read the resulting response values from an output file. This automated driver architecture enabled many model evaluations to be executed sequentially without manual intervention, following the workflow described by Neilson and Cao (2019) for Dakota-WinDAM C coupling. All tabular output was written to a data file for each model for subsequent post-processing.

Three erosion response variables were tracked for each simulation across all three models: final breach width, final hydraulic control elevation, and final headcut distance. These outputs collectively characterize breach geometry, enabling direct comparison of parameter sensitivities across the three modeling frameworks. Each response variable was computed from the model output time series, with final values extracted at the end of the simulation.

Post-processing of the Dakota tabular output was performed in Python using the Spyder integrated development environment. Simple (Pearson 1895) and rank (Spearman 1904) correlation coefficients were computed between each input parameter and each output response across all simulation runs. Pearson correlation captures linear associations, while Spearman rank correlation captures monotonic but potentially nonlinear relationships, making the two measures complementary indicators of parameter influence. To visualize parameter sensitivities, two graphical representations were constructed for each model. A heatmap displayed the relative change in each output response between the lowest and highest tested value of each input parameter, with color intensity indicating the magnitude and direction of that low-versus-high effect.

The lollipop chart conveyed the same information in an alternative format: filled circles at the upper bound of each input parameter and open circles at the lower bound, with a horizontal bar connecting them whose length reflects the magnitude of the sensitivity. Bars were sorted by length to rank the parameter's influence within each model. The Dakota-generated Pearson and Spearman correlation matrices were used as a complementary reference to characterize the overall linear and monotonic associations between inputs and outputs across all simulation runs. Because the correlation matrices reflect the full distribution of model evaluations while the heatmap and lollipop charts capture only the low-versus-high contrast at the parameter bounds, the two representations are not directly equivalent. The correlation matrices may indicate a stronger or more general relationship than is visually apparent in the bound-based charts. Together, these correlation-based outputs identify which parameters most strongly govern breach behavior in each model and provide a basis for comparing parameter importance across the energy-based, stress-based, and DLBreach modeling frameworks.

3.4 Summary

This chapter discussed the approach used to create simulations of the Kang et al. and Breland et al. simulations with the programs WinDAM C and DLBreach. The simulations were created by first selecting the appropriate geometric, hydraulic, soil, and vegetation input parameters for each experiment, then applying the governing equations and model-specific assumptions needed to represent breach initiation, headcut migration, and breach widening. For WinDAM C, the chapter addressed how the energy-based and stress-based formulations were used to model erosion processes, while DLBreach was configured to simulate overtopping breach development using its cohesive-soil and hydraulic-routing framework.

The chapter also described the source and estimation of key input properties, including parameters derived directly from experimental data and others inferred from published correlations or model procedures when measurements were unavailable. In addition, this chapter outlined the Dakota-based sensitivity analysis used to evaluate how changes in selected parameters influenced predicted breach behavior. Together, these methods established the basis for the simulation comparisons and result interpretation presented in the following chapters.

CHAPTER 4

Results

This chapter presents simulation results from WinDAM C and DLBreach programs applied to two experiments involving the overtopping of cohesive embankments. The first experiment was conducted by Kang et al. (2021) in South Korea, and the second by Breland et al. (2025) in Vicksburg, Mississippi. Both experiments included untreated and biopolymer-treated embankments. The simulation results are compared with observations to assess how well WinDAM C and DLBreach capture observed breach progression using respective input parameters for each scenario. Post-processing of the simulations was performed in Python using the output text files generated by each program to produce visual plots of key breach-failure metrics. This approach enables a direct comparison of each model's predictive capabilities against field observations, facilitating the evaluation of their effectiveness in capturing embankment breach processes under varying soil treatment conditions.

Model validation in this study was performed by comparing simulated responses against observed experimental data for the Kang et al. (2021) and Breland et al. (2025) datasets. For the Breland et al. (2025) cases, validation was organized by experimental phase: blind prediction was used to evaluate the overtopping phase, breach-only simulations to evaluate the breach phase, and combined overtopping-plus-breach simulations to evaluate both phases together. Model performance was assessed using set of output metrics, including surface loss, upstream water surface elevation as an indicator of breach initiation, headcut position, breach width, and breach bottom elevation or hydraulic control. These outputs were compared across the lab-observed, USDA-correlated, and best-fit parameter sets, as appropriate. Where applicable, best-fit calibration was used to identify parameter values that improved agreement in final surface loss and final breach width, and a final log-residual summary was used to compare the relative performance of the models.

4.1 Kang et al. (2021) Experiment Results

This section presents the simulation results for the Kang et al. (2021) overtopping experiments using the WinDAM C energy-based model, WinDAM C stress-based model, and DLBreach. Simulations were performed for both untreated and biopolymer-treated embankments, using baseline parameter sets derived from empirical correlations and, where applicable, calibrated best-fit parameter sets. Model performance was evaluated by comparison against observed surface loss. Kang et al. (2021) defines surface loss as the proportion of the downstream slope area that eroded relative to the full surface area of the levee, estimated from time-series image digitization and confirmed with 3D point cloud modeling. In this study, surface loss was calculated from the model output for each simulation as the ratio of breach width to total crest length. This alternative definition was necessary because the present modeling framework represents headcut development differently.

Across all models, two parameter sets were evaluated: (i) baseline values derived from empirical correlations or values reported in prior studies, and (ii) calibrated 'best-fit' values obtained by adjusting one or two key parameters to better match the observed breach progression. In all comparisons, surface loss due to erosion is expressed as the percentage of breach or crest width relative to the total embankment or crest length. To focus on post-initiation processes, the simulation time for WinDAM C was re-referenced so that t = 0 corresponds to the observed breach initiation, while DLBreach inherently begins computations at that time.

4.1.1 WinDAM C Energy Model Results – Untreated Embankment

The WinDAM C energy model results for the untreated embankment are shown in Figure 15. Using baseline parameters derived from empirical correlations, the model reproduced the temporal pattern and magnitude of erosion observed in the experiment without any adjustment to erodibility inputs, indicating that the correlated parameter set captured the observed erosion for this case.

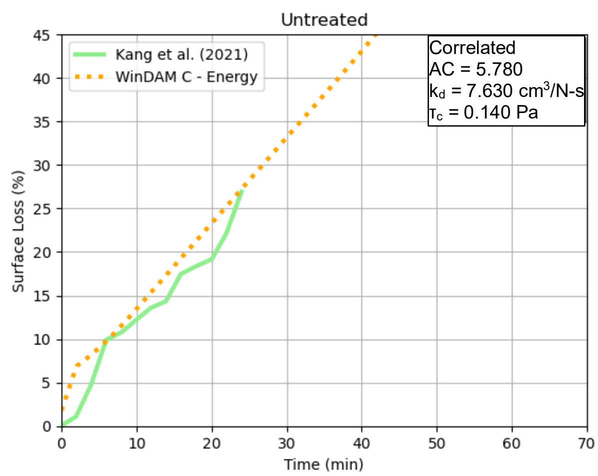

Figure 15. Simulation results from the WinDAM C energy-based model for the untreated embankment using parameter values derived from empirical correlations.

4.1.2 WinDAM C Stress Model Results – Untreated Embankment

The WinDAM C stress-model results for the untreated embankment are presented in Figure 16. With the baseline parameter set, which used a correlated s_u = 39.500 kPa based on Zhang et al. (2009), the model underpredicted the headcut erosion rate. To improve agreement with the observed breach progression, s_u was reduced to 21.500 kPa (Figure 16b), a moderate decrease that shifts the material characterization from a medium-stiff to a soft clay, based on the range reported by Peck et al. (1974). This best-fit value falls within the plausible range for the embankment materials and was used to represent the untreated embankment's strength in other parts of this study.

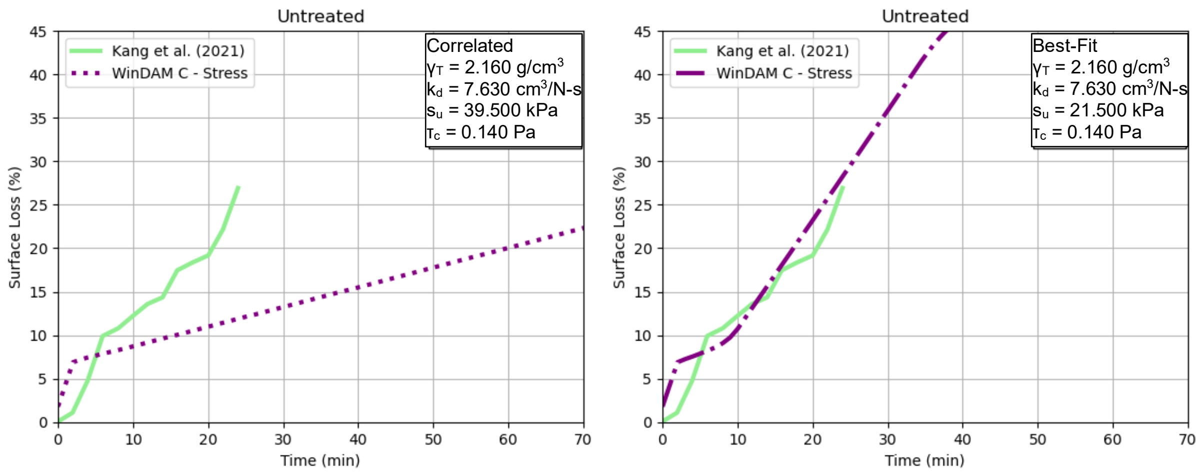

(a) (b)

Figure 16. Simulation results from the WinDAM C stress-based model for the untreated embankment using (a) parameter values derived from empirical correlations and (b) best-fit parameter values obtained via calibration.

4.1.3 DLBreach Results – Untreated Embankment

The DLBreach simulation results for the untreated embankment are presented in Figure 17. With baseline parameters, including n = 0.016 (the value recommended in the DLBreach manual and previously tested with the model) and a correlated k_d, the model produced erosion that was noticeably slower than observed. The best-fit simulation increased n to 0.025 and k_d to 23.000 cm³/N-s (Figure 17b). The revised roughness is consistent with values reported by Arcement and Schneider (1989) for firm soil surfaces, whereas n = 0.016 is more representative of concrete. The calibrated k_d is somewhat higher than typical values but remains within the upper range reported for cohesive soils under breach-scale shear stresses (e.g., up to about 25.000 cm³/N-s in Ursic and Langendoen 2021).

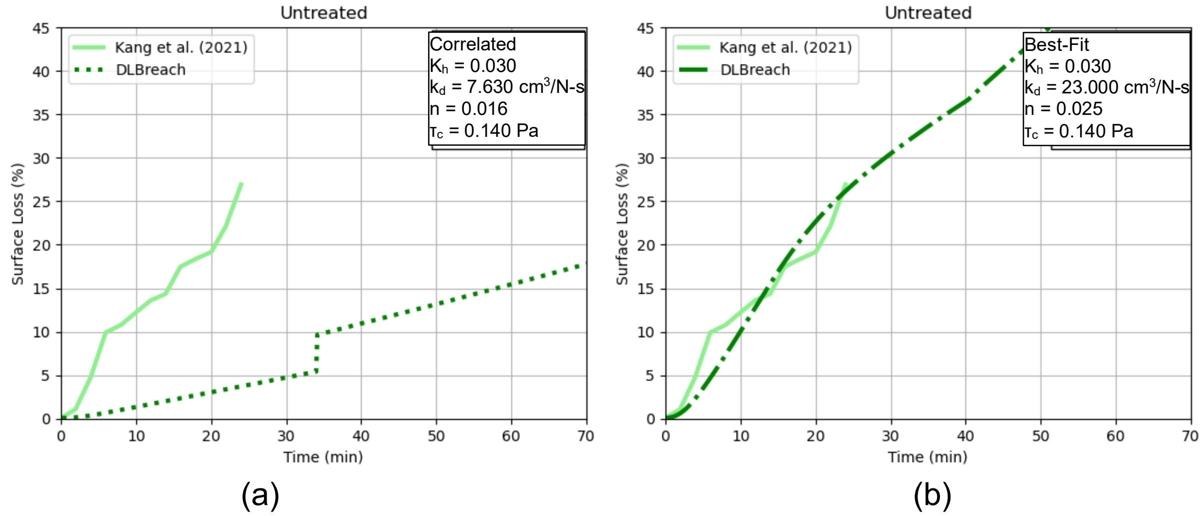

Figure 17. Simulation results from DLBreach for the untreated embankment using (a) parameter values derived from empirical correlations and (b) best-fit parameter values obtained via calibration.

4.1.4 WinDAM C Energy Model Results – Treated Embankment

The WinDAM C energy model results for the treated embankment are shown in Figure 18. Using the depth-weighted composite parameters, the model reproduced the delayed onset and reduced rate of erosion relative to the untreated case (Figure 15a) but overpredicted erosion once headcutting began (Figure 18a). Achieving close agreement with the observed headcut progression required reducing the advance coefficient from 4.360 to 1.700 (Figure 18b). Using equation 6, this adjustment corresponds to an increase in the implied material strength number from 0.300 to 8.730, which falls in the range associated with moderately soft rock rather than cohesive soil. This suggests that the calibrated AC is acting as a compensating parameter and that additional work is needed to understand how biopolymer treatment may alter headcut mechanics, particularly given the lack of direct erodibility measurements in Kang et al. (2021).

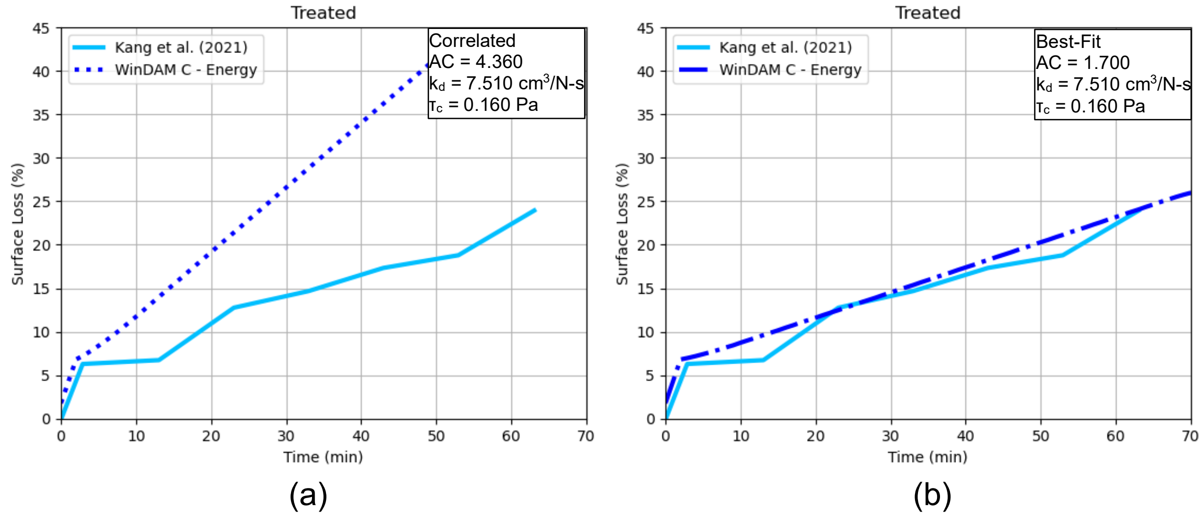

Figure 18. Simulation results from the WinDAM C energy-based model for the treated embankment using (a) parameter values derived from empirical correlations and (b) best-fit parameter values obtained via calibration.

4.1.5 WinDAM C Stress Model Results – Treated Embankment

The stress-model simulations for the treated embankment are presented in Figure 19. Using the depth-weighted composite s_u derived from the correlation-based untreated value (Zhang et al. 2009) and the treated strength from Ayeldeen et al. (2016), the model captured the delayed onset and reduced erosion rate relative to the untreated embankment but slightly underpredicted the measured erosion rate (Figure 19a). The best-fit was achieved by reducing s_u by approximately 22% (Figure 19b), which still leaves the treated embankment stronger than the calibrated untreated case (21.500 kPa vs. about 33.500 kPa). This level of reduction remains consistent with published variability in biopolymer-induced strength gains, as 1% biopolymer has been reported to increase unconfined compressive strength by up to roughly 50% (Çetin et al. 2024).

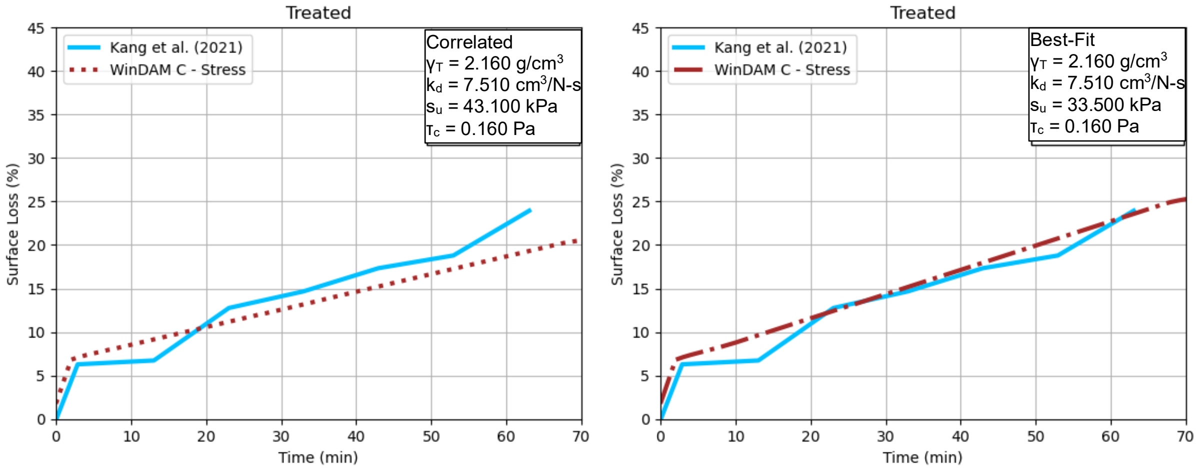

(a) (b)

Figure 19. Simulation results from the WinDAM C stress-based model for the treated embankment using (a) parameter values derived from empirical correlations and (b) best-fit parameter values obtained via calibration.

4.1.6 DLBreach Results – Treated Embankment

The DLBreach results for the treated embankment are shown in Figure 20. Using the composite correlated parameters, the model again produced erosion rates slower than observed (Figure 20a). In this case, satisfactory agreement was achieved by increasing Manning's n to 0.025 (Figure 20b), the same roughness value adopted for the untreated best-fit case. As with the untreated simulations, this increase from the manual's recommended n = 0.016 moves the roughness from a concrete-like value to one more representative of firm soil (Arcement and Schneider 1989) and thus remains physically plausible for both untreated and biopolymer-treated embankment surfaces.

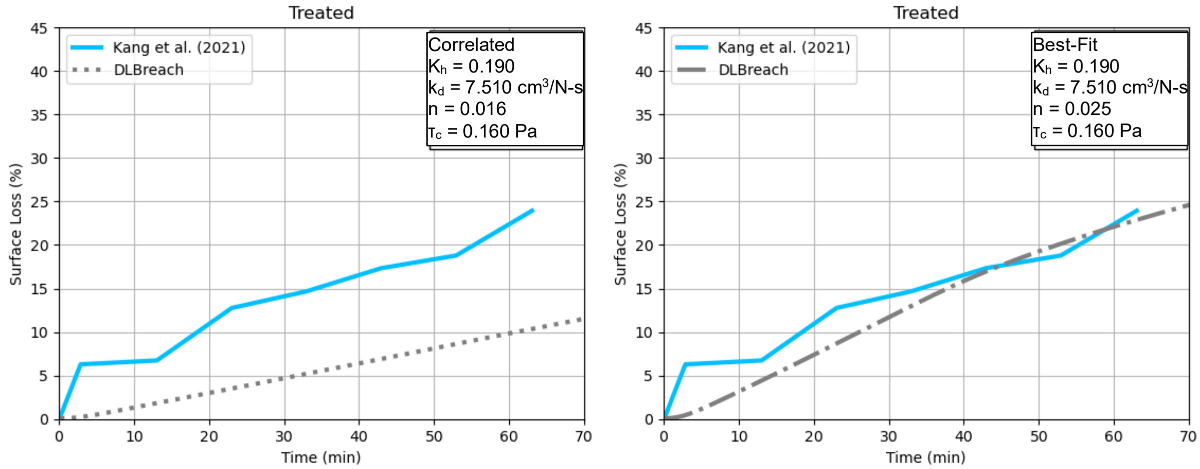

(a) (b)

Figure 20. Simulation results from DLBreach for the treated embankment using (a) parameter values derived from empirical correlations and (b) best-fit parameter values obtained via calibration.

4.1.7 Simulated Breach Progression Comparison

Surface loss was adopted as the principal metric for comparing simulation results to experimental observations because this was the data provided by the study authors, but it is not a standard output variable in embankment breach studies. The temporal evolution of breach width, breach bottom elevation, and headcut migration was also analyzed for the DLBreach, WinDAM C energy-based, and WinDAM C stress-based models, both with and without biopolymer treatment, to further assess the impact of biopolymer treatment on breach development. Both the initial (correlation-based) and best-fit parameter sets were evaluated (Figure 21, Figure 22, and Figure 23). Headcut migration was evaluated using Equation 1, because DLBreach does not explicitly report headcut advancement as an output (Wu 2025, personal communication).

Headcut progression results show consistent differences across models and treatments. In the untreated case, Figure 21a shows that the WinDAM C energy-based model, stress-based (best-fit) model, and DLBreach results were in close agreement. However, the DLBreach best-fit model showed greater headcut development, while the correlated WinDAM C stress-based model exhibited comparatively lower headcut progression. In treated cases, Figure 21b shows that the energy-based WinDAM C model predicts more headcut progression than the stress-based WinDAM C model and DLBreach. However, the best-fit energy- and stress-based WinDAM C simulations remain in close agreement, while DLBreach, like the untreated best-fit case, continues to predict more rapid headcut growth.

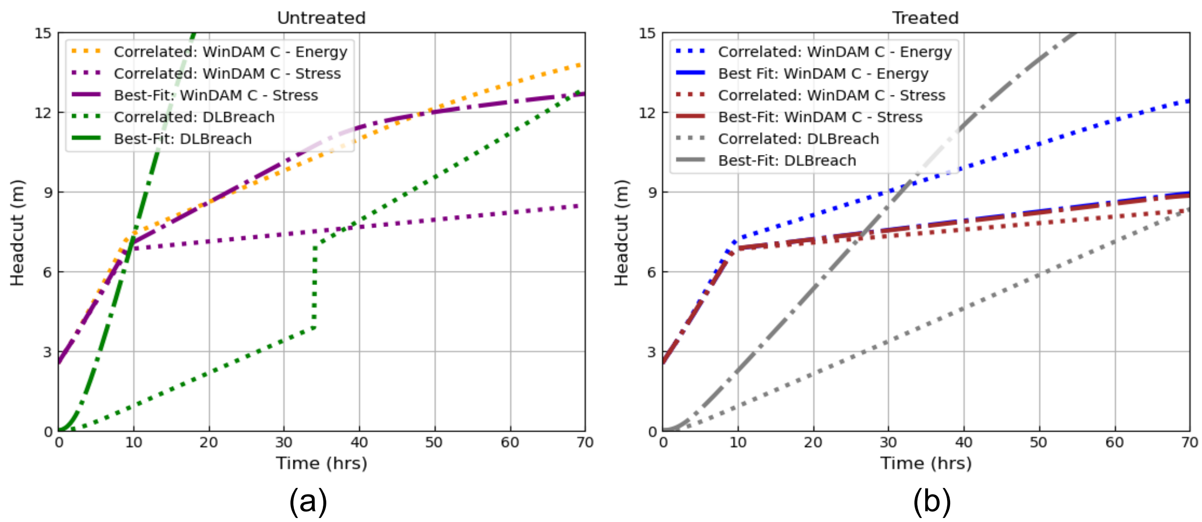

Figure 21. Evolution of headcut progression obtained from simulation for (a) untreated and (b) treated embankment cases.

Breach-widening behavior varies with both model formulation and parameter selection. In the untreated case, simulations with the WinDAM C energy-based model using correlated parameters showed good agreement with experimental results and required no adjustment, whereas simulations with the WinDAM C stress model and DLBreach, both with initial correlated values, predicted less erosion. After parameter adjustment to achieve best-fit conditions, breach widths from all three models converged (Figure 22a). In treated cases, however, both DLBreach and the WinDAM C stress (correlated) models predict less widening, while the WinDAM C energy-based model produces more conservative (larger) estimates (Figure 22b).

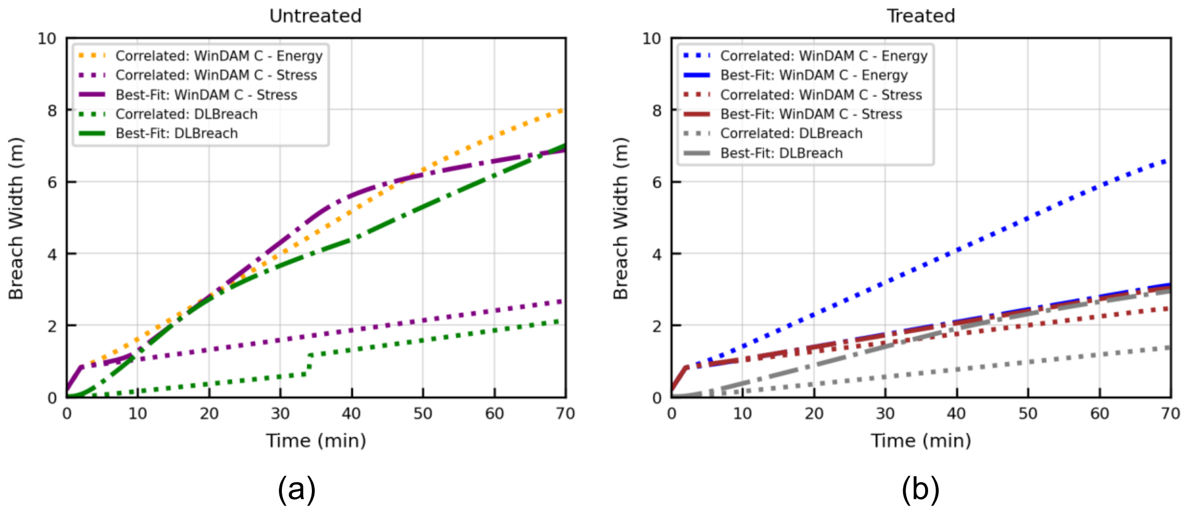

Figure 22. Evolution of breach widening progression obtained from simulation for (a) untreated and (b) treated embankment cases.

The hydraulic control elevation, or breach-bottom elevation, shows a different pattern of agreement among models. In the untreated case, breach bottom elevations from both the energy-based and best-fit stress-based WinDAM C models were in close agreement (Figure 23a), whereas DLBreach produced a more erodible response, with lower breach bottom elevations. In treated cases, the stress-based WinDAM C model maintains reasonable agreement with correlated values, whereas both DLBreach and the WinDAM C energy-based model exhibit a more erodible response, characterized by greater downcutting erosion (Figure 23b).

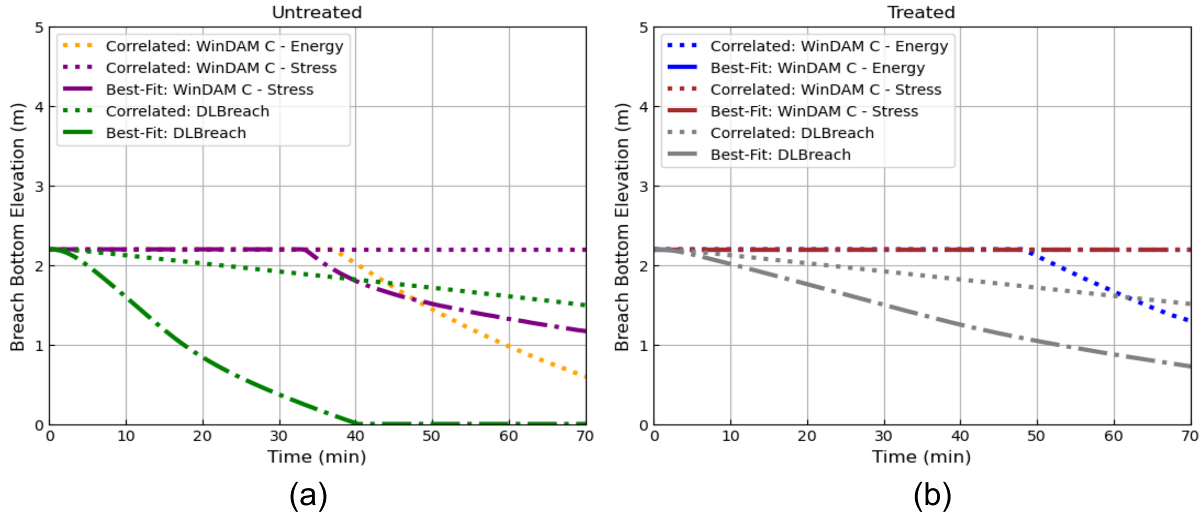

Figure 23. Evolution of breach deepening obtained from simulation for (a) untreated and (b) treated embankment cases.

4.2 Breland et al. (2025) – Blind Prediction

Breland et al. (2025) overtopping tests at ERDC Vicksburg featured split embankments (treated/untreated halves) under sustained overtopping until breach, providing upstream water levels, headcut migration, widening, and hydraulic control data (Figures 11-14). The blind predictions were performed before the results were shared with the author, and used both lab-observed (Table 6) and correlated inputs (Table 7) in WinDAM C and DLBreach.

4.2.1 WinDAM C Energy Model Results – Untreated Embankment

The blind prediction WinDAM C energy-based model results for the untreated embankment are shown in Figures 24-27. Observed upstream water surface elevations (Figure 24) agree well with both the lab-observed and the correlated data sets until approximately 25 hours, when a sharp drop in the simulated water level indicates the initiation of erosion. Following initiation, headcut migration (Figure 25) advances rapidly in both data sets, reaching the full distance from upstream to downstream toe (10 meters) in approximately 3 hours. Breach widening (Figure 26) proceeds more rapidly for the lab-observed data set, achieving the full crest length (7.32 meters) in approximately 4 hours, while the correlated data set overpredicts final breach width by 33% (~6.2 meters). Breach deepening (hydraulic control) (Figure 27) is similarly rapid across both data sets, with the breach bottom reaching the embankment foundation in approximately 3 hours.

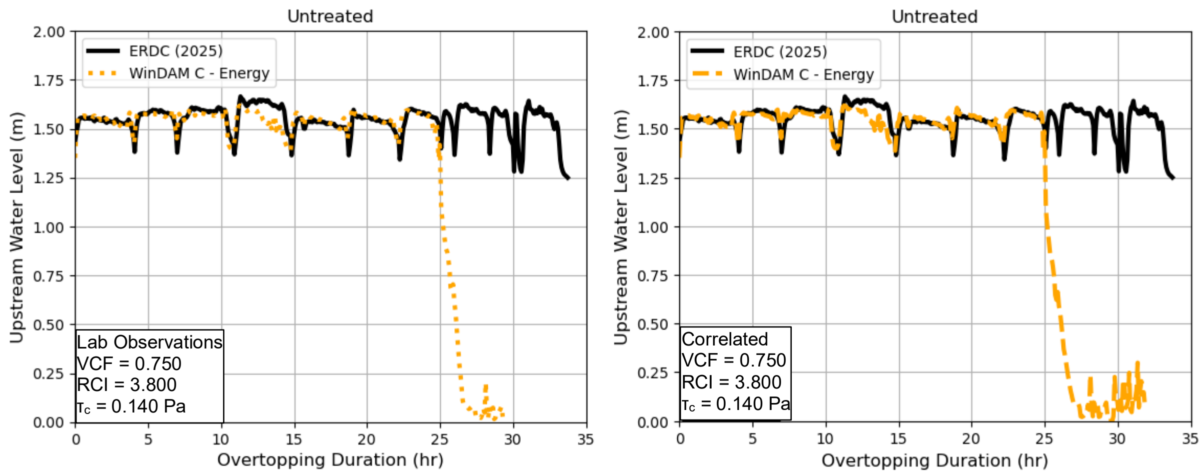

(a) (b)

Figure 24. Comparison of blind-predicted upstream water surface elevations from WinDAM C energy model simulations using (a) lab-observed and (b) correlated input parameter sets for the untreated embankment against ERDC (2025) experimental measurements.

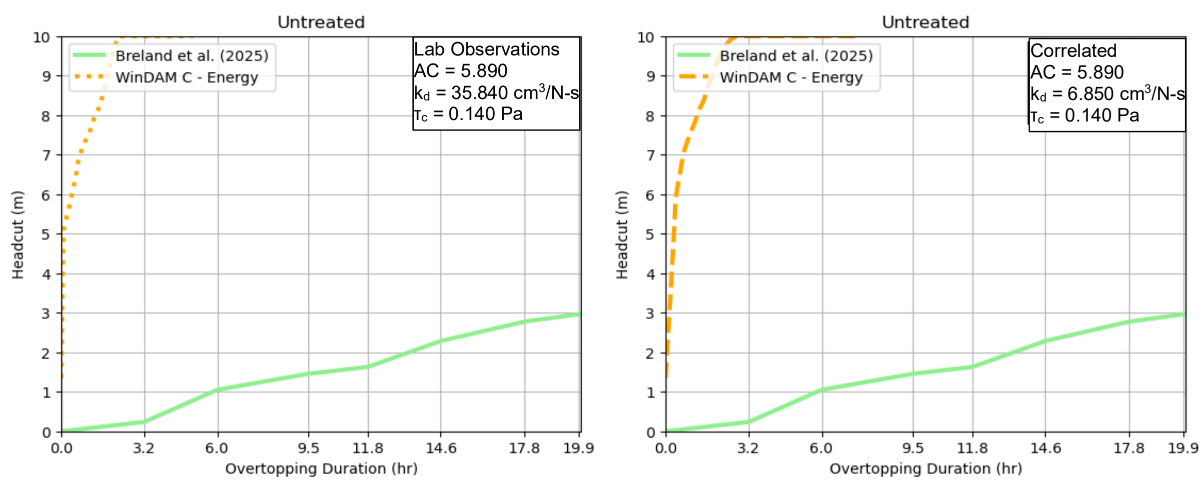

(a) (b)

Figure 25. Comparison of blind-predicted headcut progression from WinDAM C energy model simulations using (a) lab-observed and (b) correlated input parameter sets for the untreated embankment against Breland et al. (2025) breach experiment measurements.

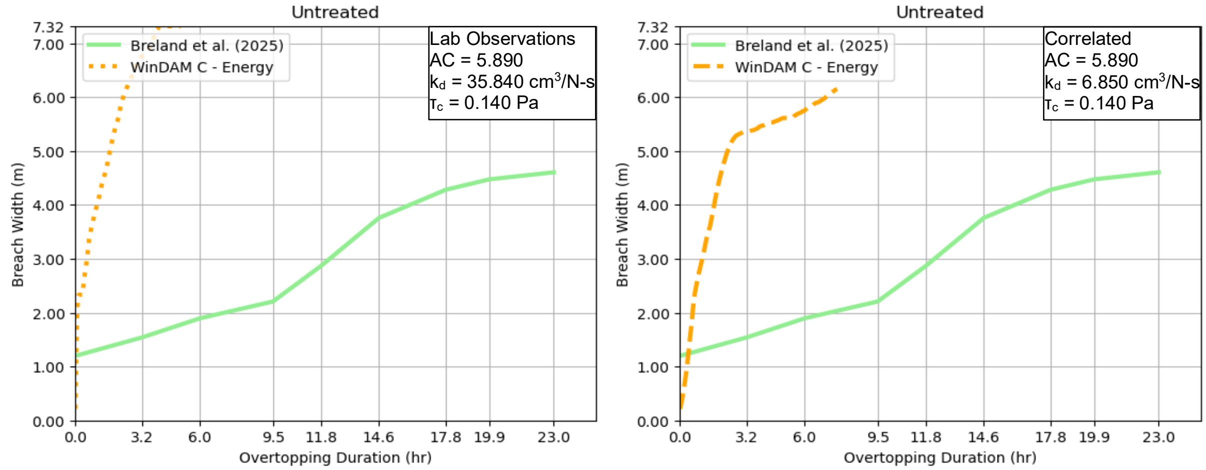

(a) (b)

Figure 26. Comparison of blind-predicted breach widening progression from WinDAM C energy model simulations using (a) lab-observed and (b) correlated input parameter sets for the untreated embankment against Breland et al. (2025) breach experiment measurements.

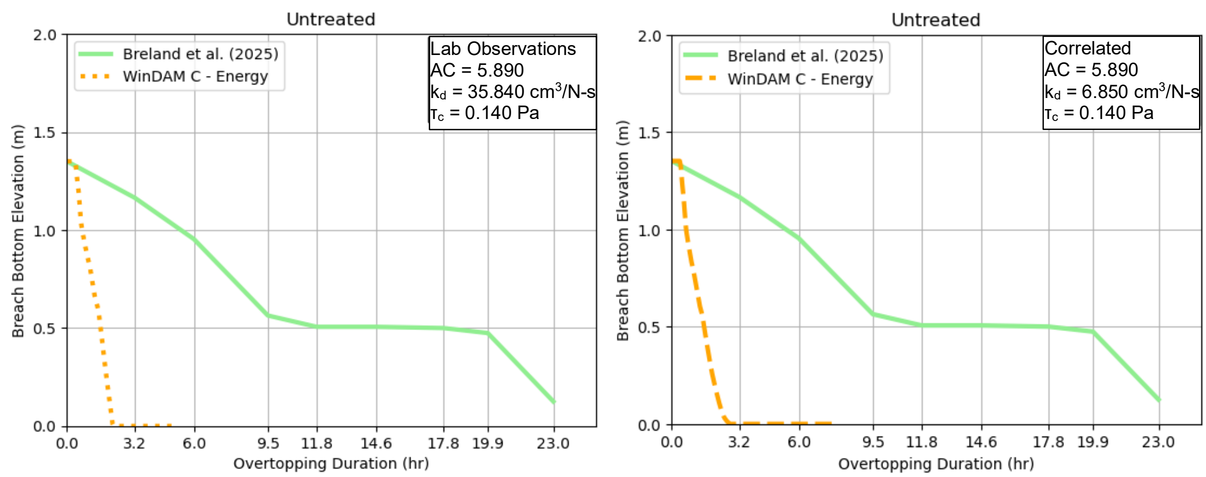

(a) (b)

Figure 27. Comparison of blind-predicted hydraulic control progression from WinDAM C energy model simulations using (a) lab-observed and (b) correlated input parameter sets for the untreated embankment against Breland et al. (2025) breach experiment measurements.

4.2.2 WinDAM C Stress Model Results – Untreated Embankment

The blind prediction WinDAM C stress-based model results for the untreated embankment are shown in Figures 28-31. Observed upstream water surface elevations (Figure 28) agree well with both lab-observed and correlated data sets until approximately 25 hours. The lab-observed data set (k_d = 35.840 cm/N-s) produces a sharp water level drop to 0 meters, indicating rapid breach formation, whereas the correlated data set (k_d = 6.850 cm/N-s) shows only a muted drop to 1 meter below the 1.5 meter embankment height due to substantially reduced downcutting erosion. Following initiation, headcut migration (Figure 29) advances rapidly in both data sets, with the lab-observed data set reaching the full toe-to-toe distance approximately 3 hours after erosion initiation. In contrast, the correlated data set overpredicts the final headcut distance by ~200% the observed maximum of 3 meters (~9 meters). Breach widening (Figure 30) proceeds more rapidly for the lab-observed data set, achieving the full crest length in approximately 5 hours from erosion initiation, while the correlated data set closely predicts the observed final breach width of ~4.6 meters (model: ~4.4 meters). Breach deepening (Figure 31) progresses rapidly for the lab-observed data set, reaching the embankment foundation in ~3 hours from the initiation of erosion, while the correlated data set achieves a comparable final breach bottom elevation (correlated: 0.2 meters vs. observed: 0.15 meters).

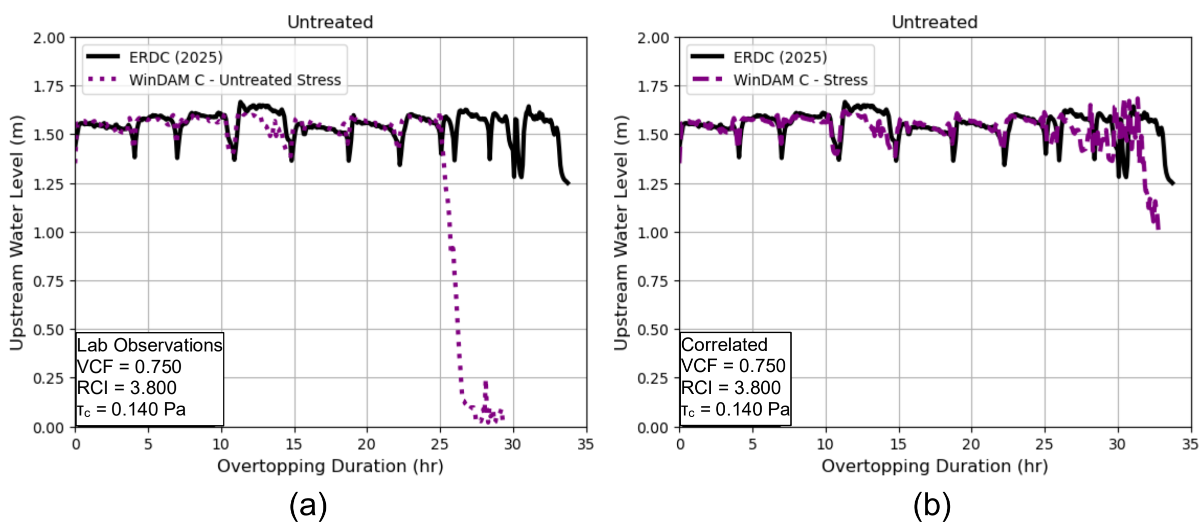

Figure 28. Comparison of blind-predicted upstream water surface elevations from WinDAM C stress model simulations using (a) lab-observed and (b) correlated input parameter sets for the untreated embankment against ERDC (2025) experimental measurements.

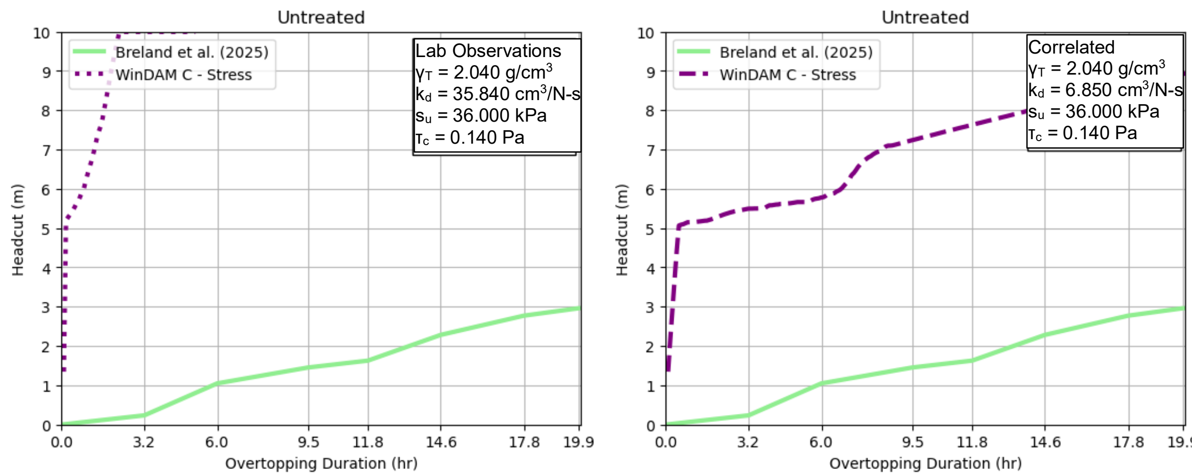

(a) (b)

Figure 29. Comparison of blind-predicted headcut progression from WinDAM C stress model simulations using (a) lab-observed and (b) correlated input parameter sets for the untreated embankment against Breland et al. (2025) breach experiment measurements.

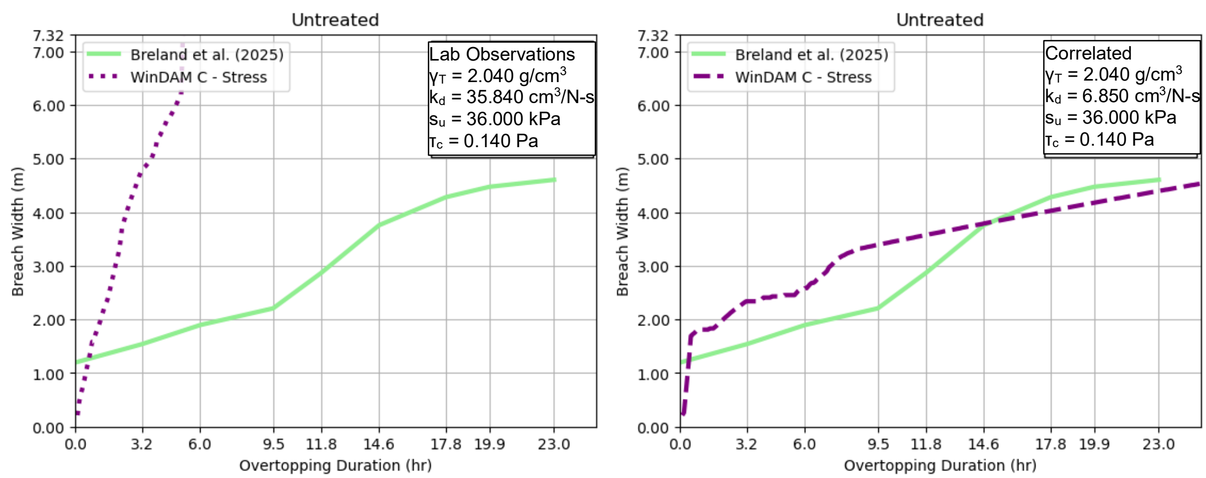

(a) (b)

Figure 30. Comparison of blind-predicted breach widening progression from WinDAM C stress model simulations using (a) lab-observed and (b) correlated input parameter sets for the untreated embankment against Breland et al. (2025) breach experiment measurements.

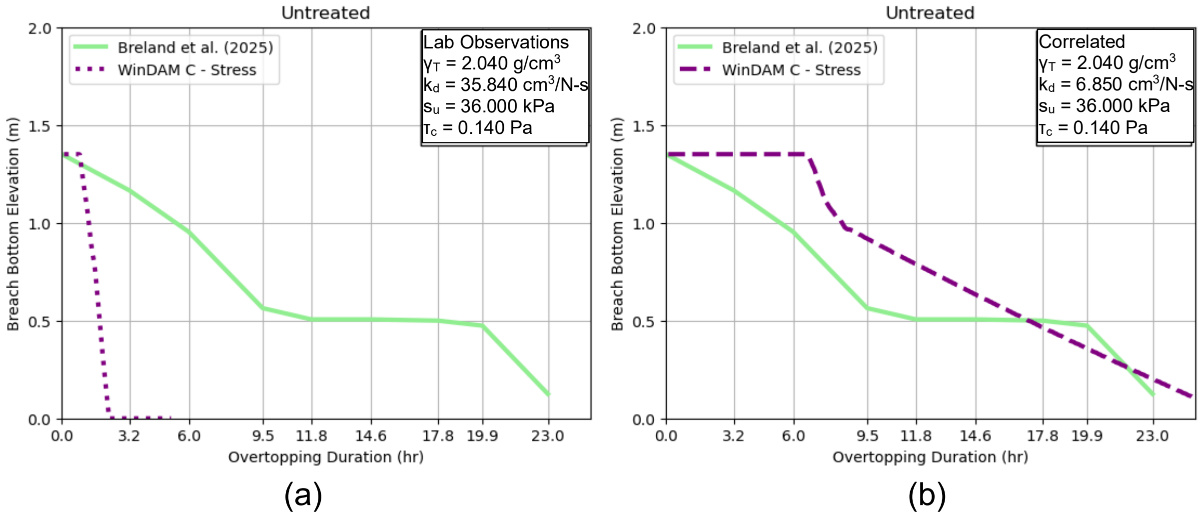

Figure 31. Comparison of blind-predicted hydraulic control progression from WinDAM C stress model simulations using (a) lab-observed and (b) correlated input parameter sets for the untreated embankment against Breland et al. (2025) breach experiment measurements.

4.2.3 DLBreach Results – Untreated Embankment

The blind-prediction results for the DLBreach model on the untreated embankment are shown in Figures 32-35. Simulated upstream water surface elevations (Figure 32) show that erosion initiates immediately at the onset of overtopping, unlike in previous WinDAM C models. This response is expected because DLBreach does not explicitly incorporate vegetation-related resistance parameters, which can delay erosion initiation. As in the WinDAM C stress-based model, the lab-observed data set produces a sharp drop in water level to 0 meters, whereas the correlated data set exhibits a slower downcutting progression to 0 meters due to the lower erodibility coefficient. Headcut migration (Figure 33) continues to advance rapidly in both data sets, with the lab-observed data set reaching the full toe-to-toe distance in approximately 1 hour and the correlated data set in approximately 5 hours. Breach widening (Figure 34) also proceeds more rapidly for the lab-observed data set, reaching the full crest length in approximately 7 hours, while the correlated data set accurately predicts the observed final breach width of approximately 4.6 meters. Breach deepening (Figure 35) progresses rapidly for both data sets, with the lab-observed and correlated cases reaching the embankment foundation in approximately 3.2 hours and 12 hours, respectively.

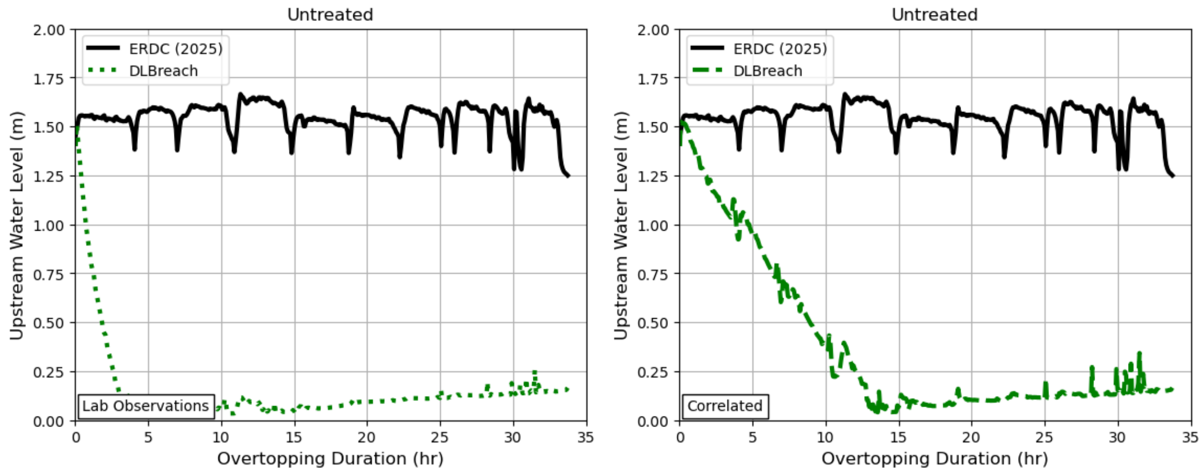

(a) (b)

Figure 32. Comparison of blind-predicted upstream water surface elevations from DLBreach simulations using (a) lab-observed and (b) correlated input parameter sets for the untreated embankment against ERDC (2025) experimental measurements.

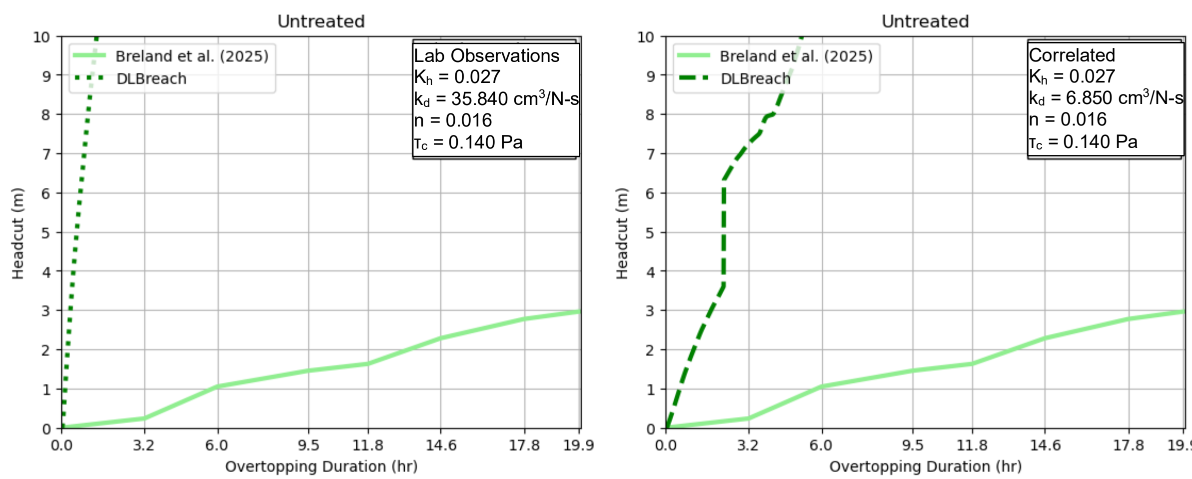

(a) (b)

Figure 33. Comparison of blind-predicted headcut progression from DLBreach simulations using (a) lab-observed and (b) correlated input parameter sets for the untreated embankment against Breland et al. (2025) breach experiment measurements.

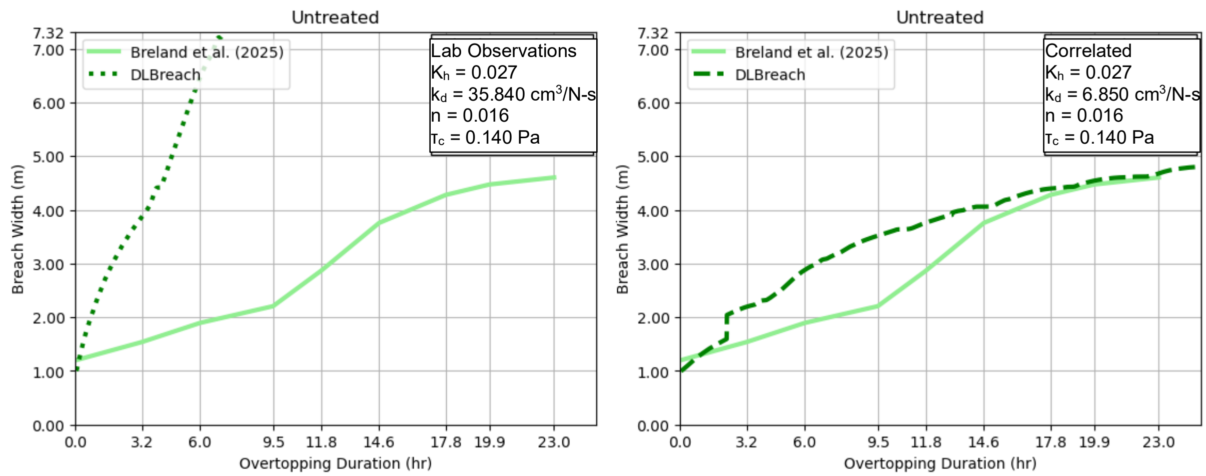

(a) (b)

Figure 34. Comparison of blind-predicted breach widening progression from DLBreach simulations using (a) lab-observed and (b) correlated input parameter sets for the untreated embankment against Breland et al. (2025) breach experiment measurements.

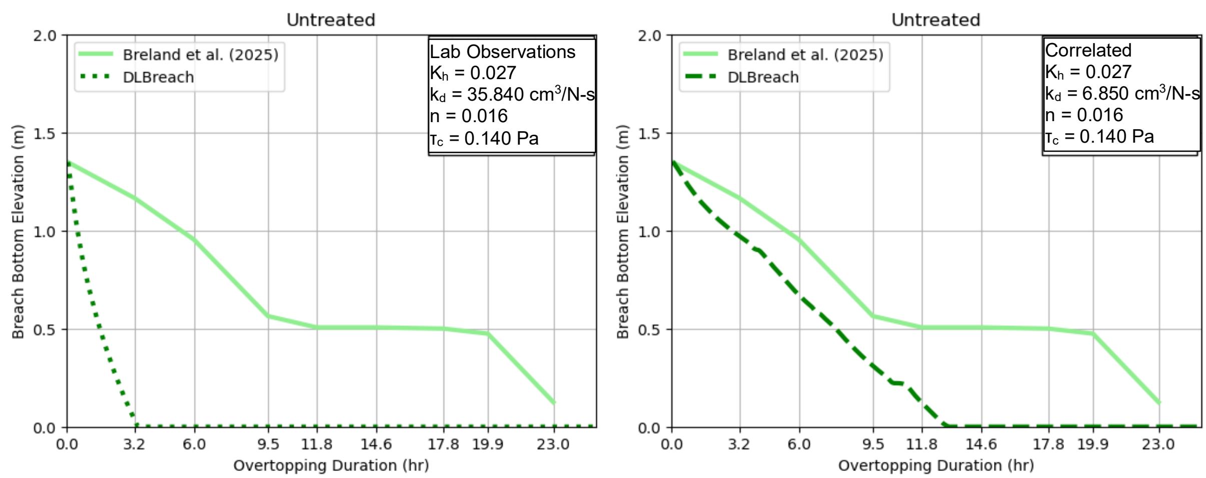

(a) (b)

Figure 35. Comparison of blind-predicted hydraulic control progression from DLBreach simulations using (a) lab-observed and (b) correlated input parameter sets for the untreated embankment against Breland et al. (2025) breach experiment measurements.

4.2.4 Sensitivity Analysis for Vegetation Parameters

A sensitivity analysis of RCI and VCF was performed, as they are the only WinDAM C inputs that explicitly represent vegetation and therefore control how grass cover influences breach initiation timing. Vegetation information was limited for the Breland et al. (2025) overtopping experiments, and so a range of RCI and VCF values were considered to understand the impacts. Figures 36 and 37 illustrate how variations in these parameters affect breach initiation timing in untreated WinDAM C stress model blind predictions. Both parameters are derived indirectly from vegetation characteristics (species mixture, stem height, and stem density) and empirical guidance, whereas key erosion parameters such as k_d and τ_c are directly constrained by laboratory testing. RCI represents the cumulative flow resistance associated with stem height, density, and vegetation type (Temple et al. 1987), while VCF is an empirical descriptor of the potential for vegetal cover to dissipate turbulent currents near the hydraulic stress boundary (Temple 1980). In this study, RCI values were selected from the discrete range in Table 2 (2.880, 5.600, 10.000), spanning the full spectrum recommended by WinDAM C and USDA (2021). Similarly, VCF values were drawn from Table 3 (0.500, 0.750, 0.900), covering the complete range suggested by WinDAM C and USDA (2021). Because these vegetation properties are based on limited categorical guidance rather than direct, spatially distributed measurements, both RCI and VCF carry greater epistemic uncertainty than the laboratory-derived erodible soil parameters.

4.2.4.1 RCI Sensitivity

The RCI sensitivity analysis in the WinDAM C stress model for the Breland et al. (2025) untreated embankment (blind prediction) evaluated how changes in vegetation-induced flow resistance affect the timing of breach initiation (Figure 36). Three discrete RCI values within the model-defined range were examined to bracket plausible vegetation conditions. At the lowest RCI of 2.880 (Figure 36a), breach initiation (as evidenced by the drop in water level) occurred earliest, approximately 9 hours after overtopping began, indicating that reduced hydraulic resistance from vegetation accelerates the onset of erosion. Increasing the RCI to 5.600 (Figure 36b) delayed breach initiation by roughly 17 hours, and the highest RCI of 10.000 (Figure 36c) did not result in breach initiation, unlike the 5.600 case, in which breach initiation occurred approximately 5 hours earlier. This demonstrates that larger RCI values (representing taller, denser vegetation) substantially enhance resistance to breach initiation.

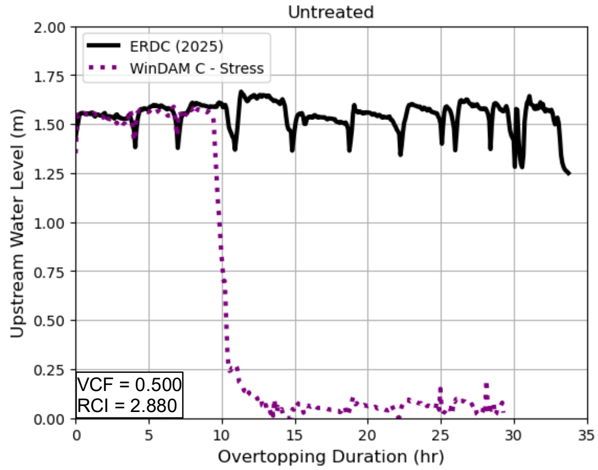

(a)

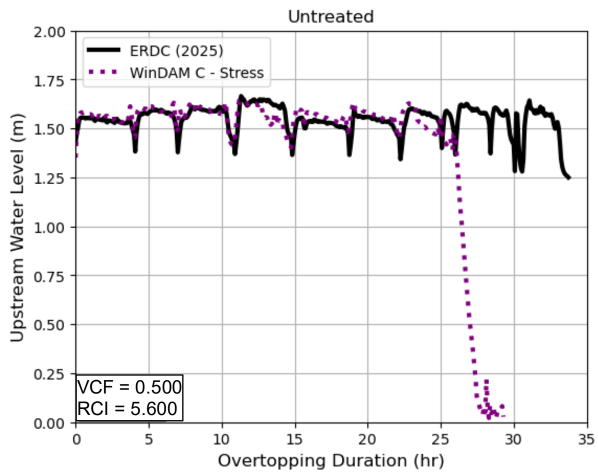

(b)

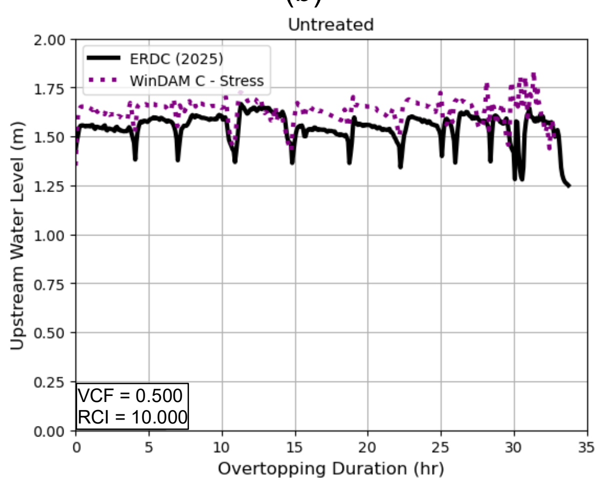

(c)

Figure 36. Sensitivity analysis results showing the impact of the RCI on breach initiation timing for untreated Breland et al. (2025) WinDAM C stress simulations (blind prediction), highlighting how variations in RCI affect the onset of embankment erosion.

4.2.4.2 VCF Sensitivity

The WinDAM C sensitivity analysis for VCF in the WinDAM C stress model for the Breland et al. (2025) untreated embankment (blind prediction) was performed to quantify how changes in the empirical representation of vegetal cover affect breach initiation timing (Figure 37). At the upper bound VCF of 0.900 (Figure 37a), the embankment remained intact for the duration of the simulation, with no breach occurring. This VCF value is consistent with a dense, highly effective vegetative cover that strongly resists erosive flows. Reducing VCF to 0.750 (Figure 37b) advanced breach initiation by approximately 15 hours relative to the no-breach case, and the lowest VCF value of 0.500 (Figure 37c) triggered breach initiation roughly 10 hours earlier than the 0.750 case. As VCF decreased, breach initiation occurred progressively earlier, indicating diminished embankment resilience.

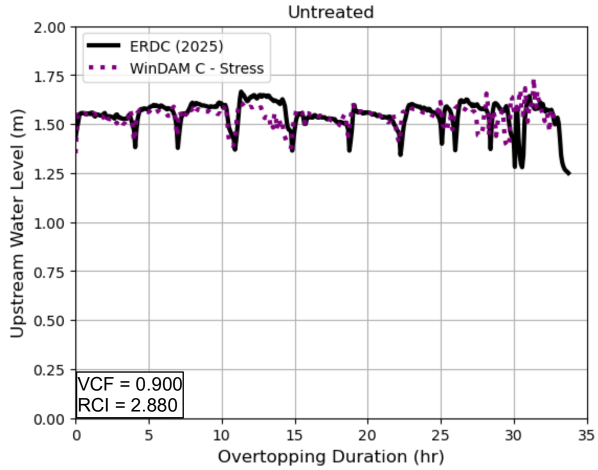

(a)

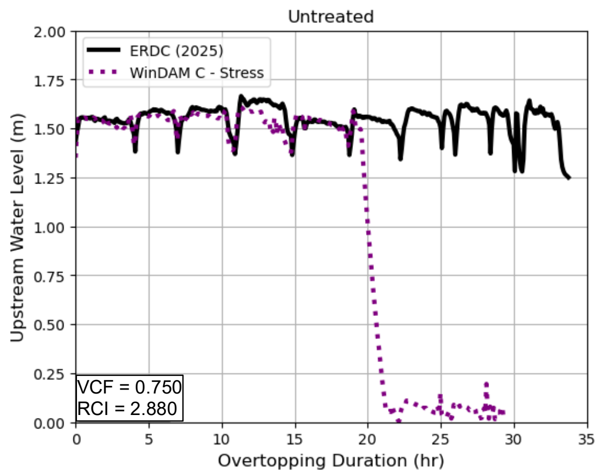

(b)

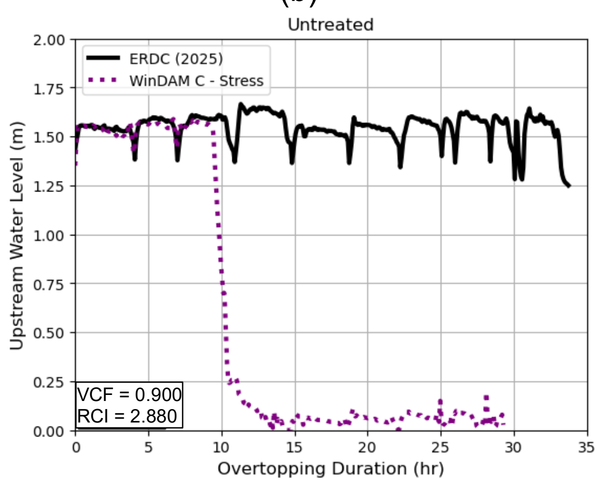

(c)

Figure 37. Sensitivity analysis results showing the impact of VCF on breach initiation timing for untreated Breland et al. (2025) WinDAM C stress simulations (blind prediction), highlighting how variations in VCF affect the onset of embankment erosion.

4.2.5 WinDAM C Energy Model Results – Treated Embankment

The blind prediction WinDAM C energy-based model results for the treated embankment are shown in Figures 38-41. Observed upstream water surface elevations (Figure 38) agree well with both the lab-observed and the correlated data sets until approximately 30 hours, when a sharp drop indicates the initiation of erosion. Following initiation, headcut migration (Figure 39) advances rapidly in both data sets, reaching the full toe-to-toe distance in approximately 2 hours. Breach widening (Figure 40) reaches ~5 meters within ~3 hours (71% above the observed 3.1 meter final width) in both cases, though limited data points reflect late simulation initiation relative to inflow. Breach deepening (Figure 41) is similarly rapid, with the breach bottom hitting the embankment foundation in ~2 hours across datasets.

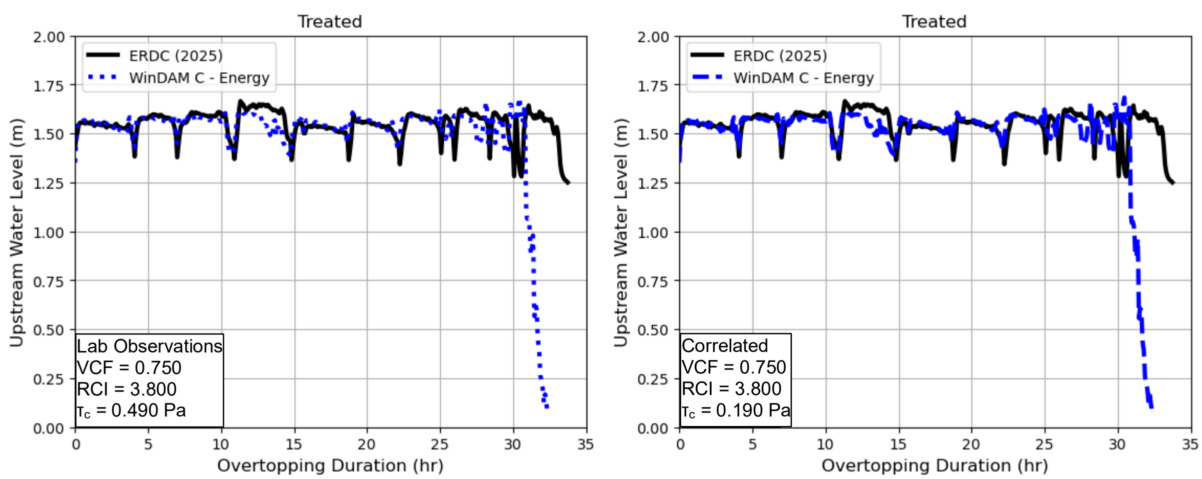

(a) (b)

Figure 38. Comparison of blind-predicted upstream water surface elevations from WinDAM C energy model simulations using (a) lab-observed and (b) correlated input parameter sets for the treated embankment against ERDC (2025) experimental measurements.

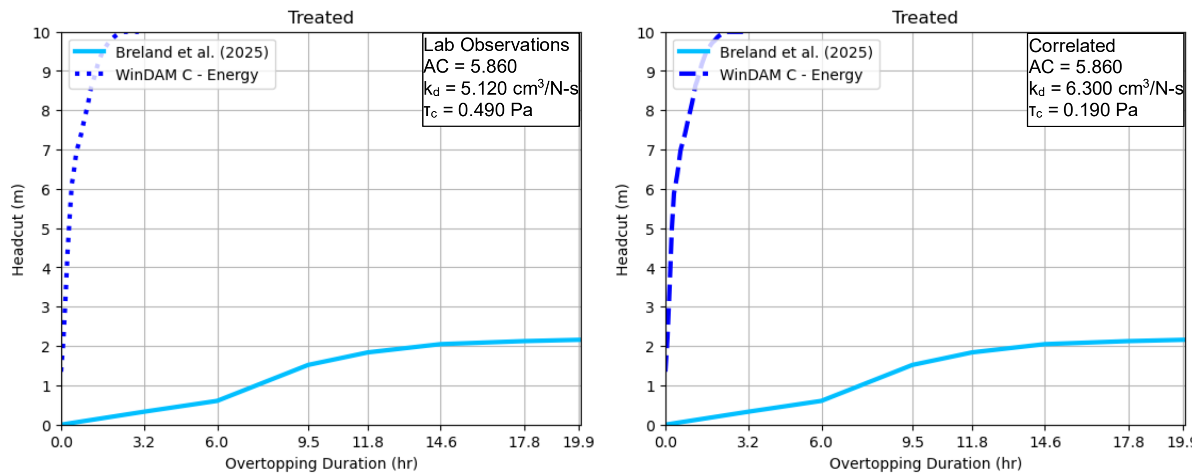

(a) (b)

Figure 39. Comparison of blind-predicted headcut progression from WinDAM C energy model simulations using (a) lab-observed and (b) correlated input parameter sets for the treated embankment against Breland et al. (2025) breach experiment measurements.

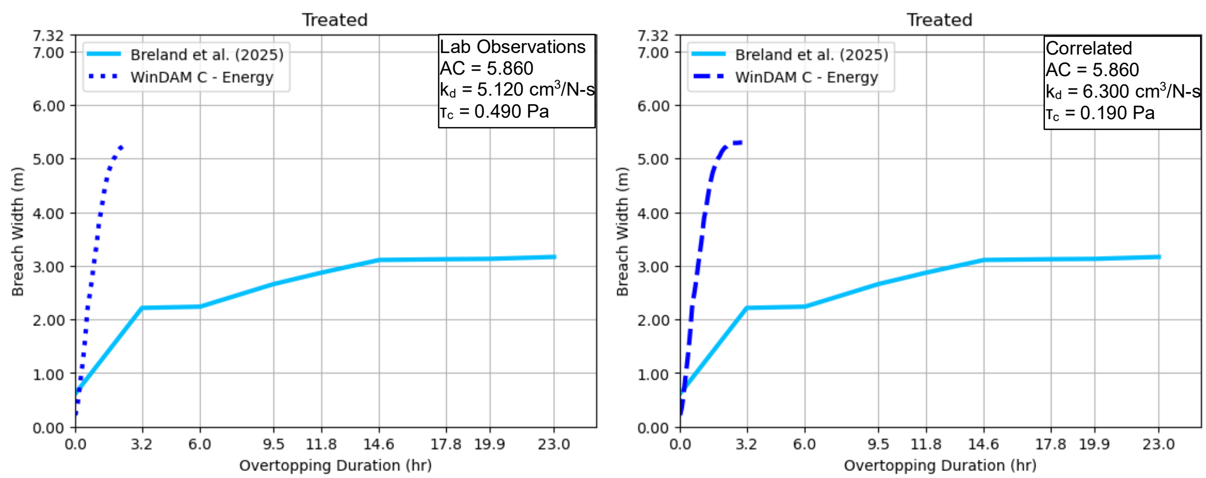

(a) (b)

Figure 40. Comparison of blind-predicted breach widening progression from WinDAM C energy model simulations using (a) lab-observed and (b) correlated input parameter sets for the treated embankment against Breland et al. (2025) breach experiment measurements.

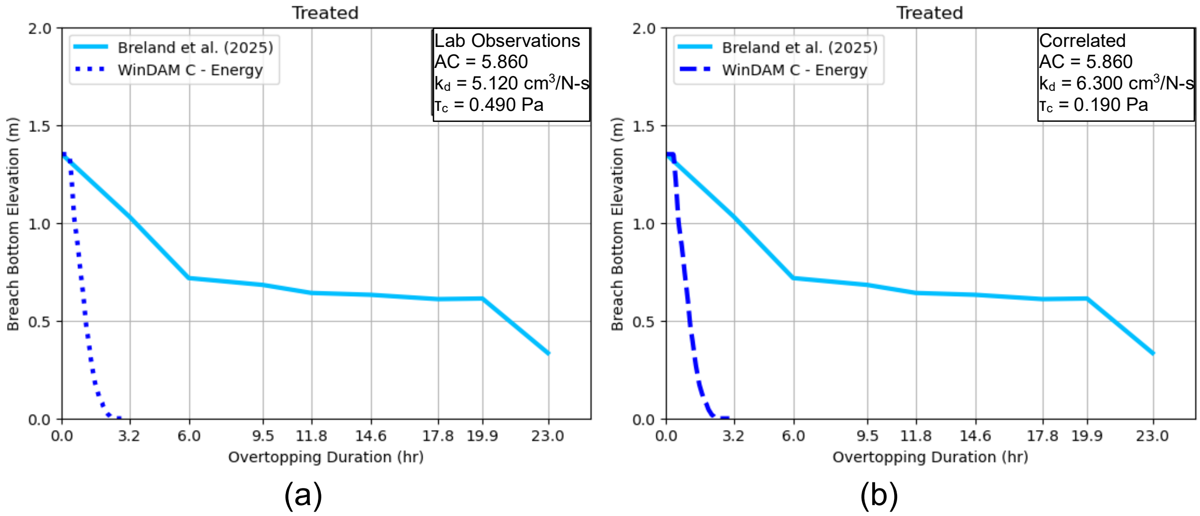

Figure 41. Comparison of blind-predicted hydraulic control progression from WinDAM C energy model simulations using (a) lab-observed and (b) correlated input parameter sets for the treated embankment against Breland et al. (2025) breach experiment measurements.

4.2.6 WinDAM C Stress Model Results – Treated Embankment

The blind prediction WinDAM C stress-based model results for the treated embankment are shown in Figures 42-45. Simulated upstream water surface elevations (Figure 42) align well with both the lab-observed and the correlated datasets until approximately 30 hours, after which model fluctuations signal erosion initiation. Following initiation, headcut migration (Figure 43) advances rapidly overpredicting by ~200% (lab-observed and correlated: ~5.5 meters vs. observed: ~2 meters). The lab-observed dataset (τ_c = 0.490 Pa) had fewer points due to its higher τ_c, limiting runtime for erosion initiation compared with the correlated dataset (τ_c = 0.190 Pa). Breach widening (Figure 44) underpredicts the final extent (lab-observed and correlated: ~1.5 meters), while no deepening occurs (Figure 45) as the breach base remains at the initial notch (lab-observed and correlated: ~1.35 meters vs. observed: ~0.4 meters).

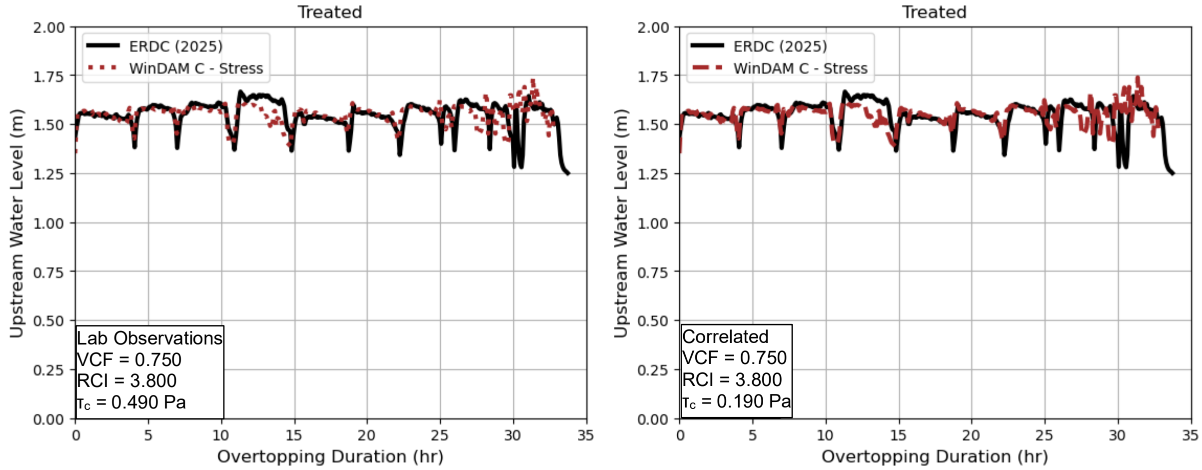

(a) (b)

Figure 42. Comparison of blind-predicted upstream water surface elevations from WinDAM C stress model simulations using (a) lab-observed and (b) correlated input parameter sets for the treated embankment against ERDC (2025) experimental measurements.

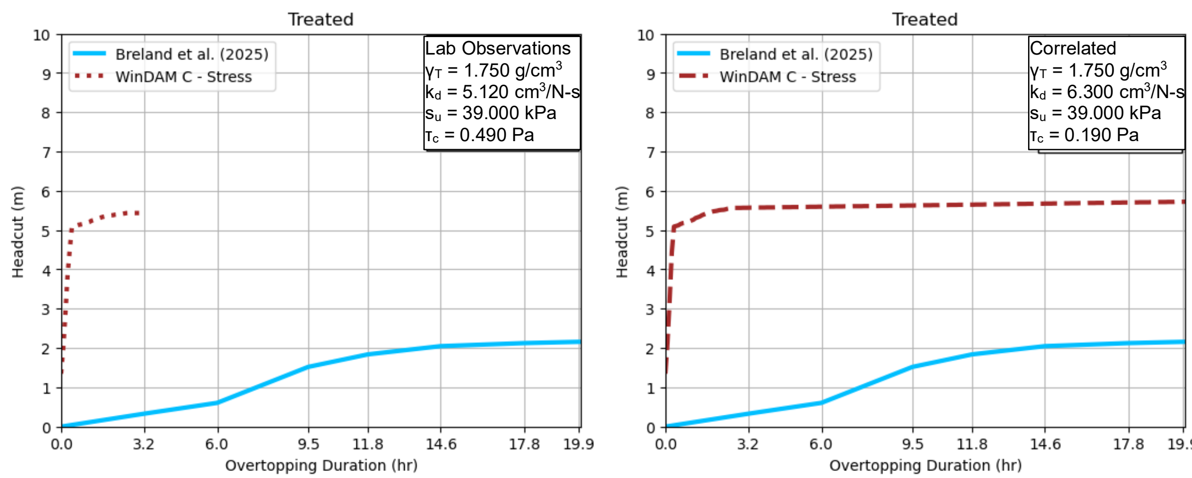

(a) (b)

Figure 43. Comparison of blind-predicted headcut progression from WinDAM C stress model simulations using (a) lab-observed and (b) correlated input parameter sets for the treated embankment against Breland et al. (2025) breach experiment measurements.

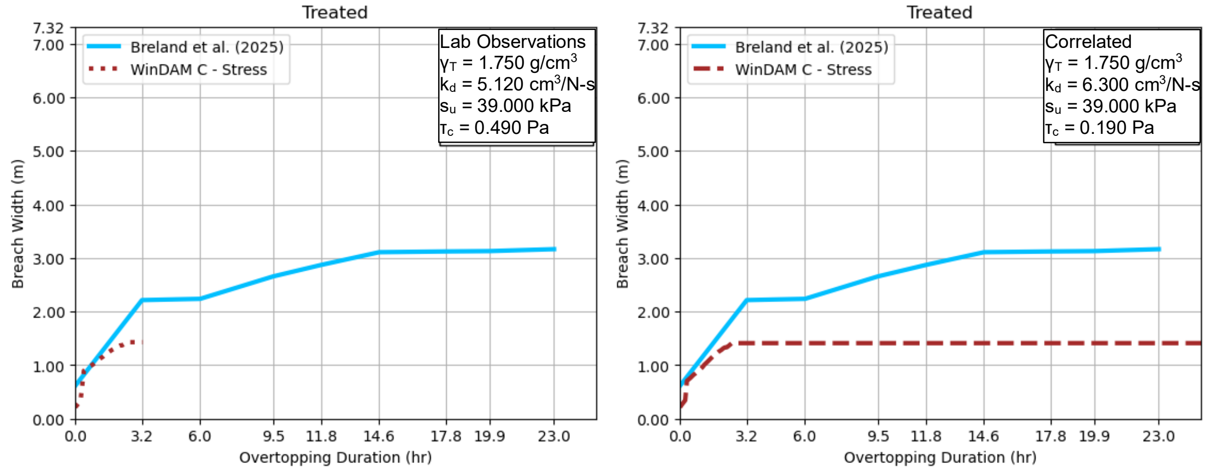

(a) (b)

Figure 44. Comparison of blind-predicted breach widening progression from WinDAM C stress model simulations using (a) lab-observed and (b) correlated input parameter sets for the treated embankment against Breland et al. (2025) breach experiment measurements.

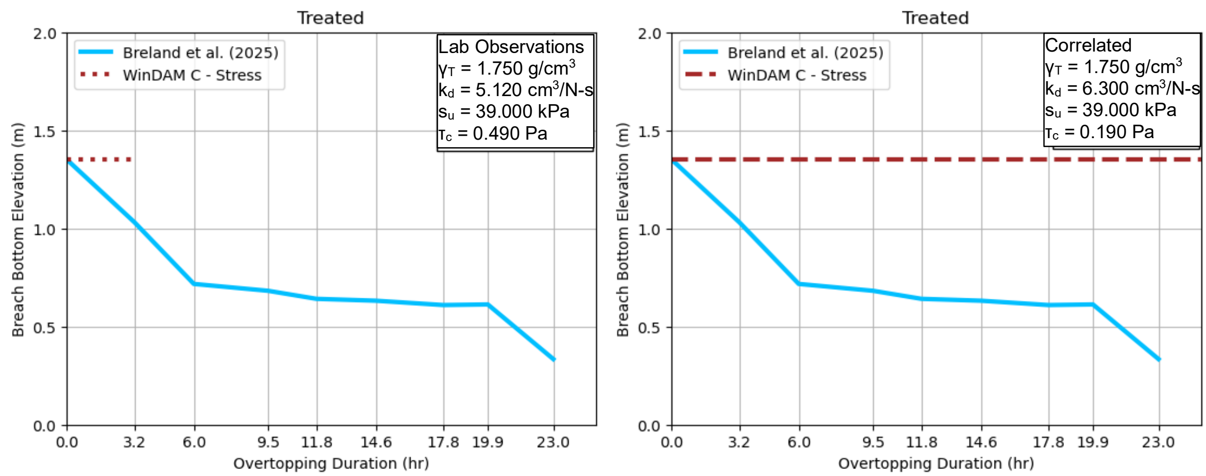

(a) (b)

Figure 45. Comparison of blind-predicted hydraulic control progression from WinDAM C stress model simulations using (a) lab-observed and (b) correlated input parameter sets for the treated embankment against Breland et al. (2025) breach experiment measurements.

4.2.7 DLBreach Results – Treated Embankment

The blind prediction DLBreach model results for the treated embankment are shown in Figures 46-49. Consistent with untreated simulations, simulated upstream water surface elevations (Figure 46) show erosion initiating immediately at overtopping onset; lab-observed data (k_d = 5.120 cm³/N-s) yield a slower water level drop to 0.1 meters

(~18 hours), while correlated data (k_d = 6.300 cm³/N-s) reach 0 meters faster (~14 hours) due to higher erodibility. Headcut migration (Figure 47) advances rapidly across datasets, spanning full toe-to-toe distance in ~6 hours. Breach widening (Figure 48) shows modest overprediction at 29% for lab-observed (~4 meters) and 39% for correlated (~4.3 meters), while deepening (Figure 49) reaches the embankment foundation more slowly in lab-observed data (~18 hours) versus correlated (~15 hours).

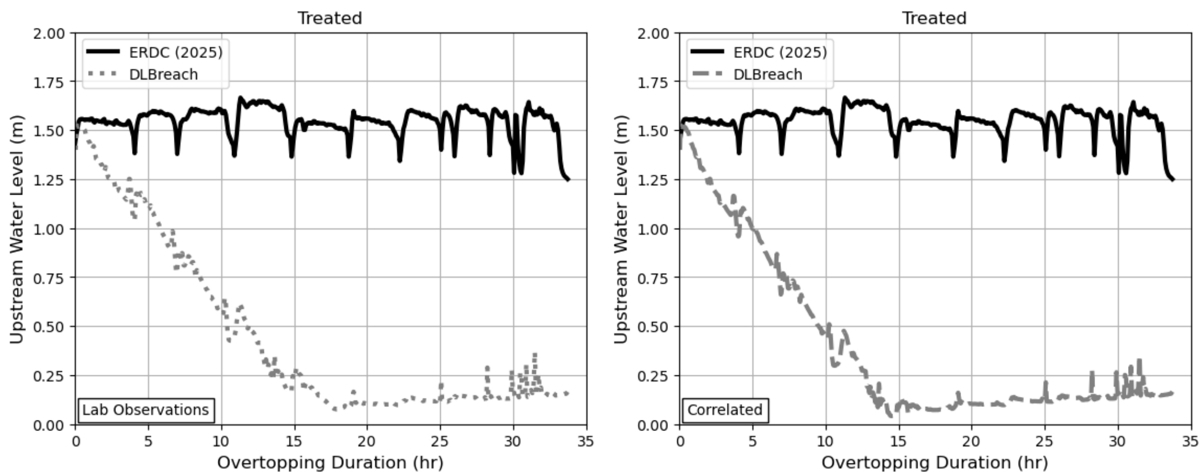

(a) (b)

Figure 46. Comparison of blind-predicted upstream water surface elevations from DLBreach model simulations using (a) lab-observed and (b) correlated input parameter sets for the treated embankment against ERDC (2025) experimental measurements.

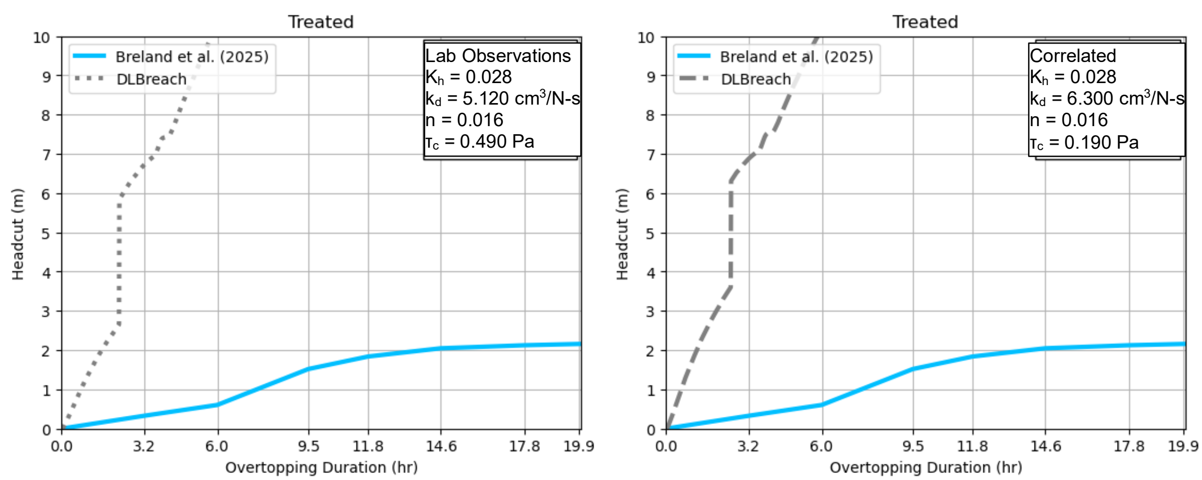

(a) (b)

Figure 47. Comparison of blind-predicted headcut progression from DLBreach model simulations using (a) lab-observed and (b) correlated input parameter sets for the treated embankment against Breland et al. (2025) breach experiment measurements.

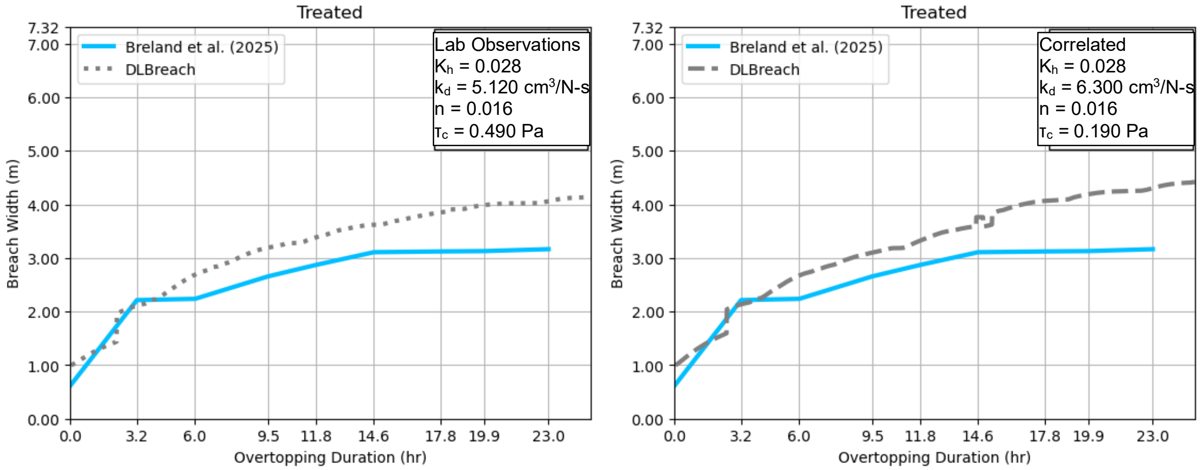

(a) (b)

Figure 48. Comparison of blind-predicted breach widening progression from DLBreach model simulations using (a) lab-observed and (b) correlated input parameter sets for the treated embankment against Breland et al. (2025) breach experiment measurements.

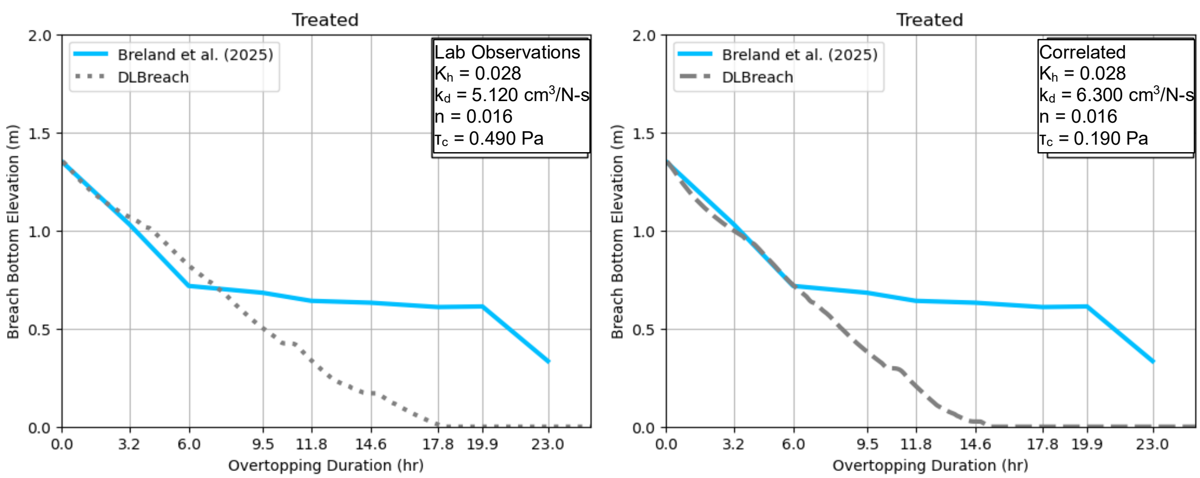

(a) (b)

Figure 49. Comparison of blind-predicted hydraulic control progression from DLBreach model simulations using (a) lab-observed and (b) correlated input parameter sets for the treated embankment against Breland et al. (2025) breach experiment measurements.

4.2.8 Summary

Overall, the blind-prediction results showed that the models reproduced the general pattern of breach development, but their accuracy varied across models, cases, and response variables. The stress-based WinDAM C formulation and DLBreach generally performed best, with several predictions bracketing the observed values and capturing the overall progression more closely than the WinDAM C energy-based formulation. By comparison, the energy-based formulation more often deviated from the observations, tending to produce a more erosive response and faster breach development than was measured in the experiments.

The blind-prediction exercise also highlighted the importance of parameter selection for both erosion initiation and breach progression. The lab-observed inputs generally produced erosion that was too rapid, with headcut advance and breach widening occurring well before the measured response, whereas the correlated inputs better matched water levels and final widths but still exaggerated headcut progression. Treated cases showed a modest delay in initiation relative to untreated cases, but the models still struggled to reproduce the observed sequence with high fidelity. These results indicate that the models were most successful at capturing broad breach trends and least successful at matching the most sensitive erosion metrics, especially where thin biopolymer effects and spatially variable resistance likely influenced the experimental response.

4.4 Breland et al. (2025) – Breach Experiment

As discussed in Chapter 3, the Breland et al. (2025) experiments were divided into two phases: overtopping, which ran until erosion was initiated; and breach, which focused on breach progression (Figure 14). The blind prediction used the overtopping phase, but it was not known at the time of those simulations when the breach initiated. The sensitivity studies in the previous section showed that the timing of breach initiation is controlled by vegetation parameters that are not well-defined. Therefore, this section focused on the breach phase of the experiment to isolate post-initiation processes. The simulations used the recorded inflows from the Breland et al. (2025) breach experiment (Figure 13), and results are compared for both the lab-observed and correlated parameters in terms of headcut, breach width, and hydraulic control elevation.

4.4.1 WinDAM C Energy Model Results – Untreated Embankment

The breach experiment WinDAM C energy-based model results for the untreated embankment are shown in Figures 50-52. Observed upstream water surface elevations are unavailable for comparison, as simulations assume immediate erosion at the onset of overtopping. Headcut migration (Figure 50) advances rapidly across datasets, reaching the full toe-to-toe distance in ~1 hour for lab-observed and ~2 hours for correlated. Breach widening (Figure 51) progresses faster using the lab-observed data, spanning full crest length in ~4 hours versus ~12 hours for correlated. Breach deepening (Figure 52) is similarly aggressive, reaching the embankment foundation in ~1 hour for the lab-observed and ~2 hours for the correlated. All of these overpredict the observed breach progression.

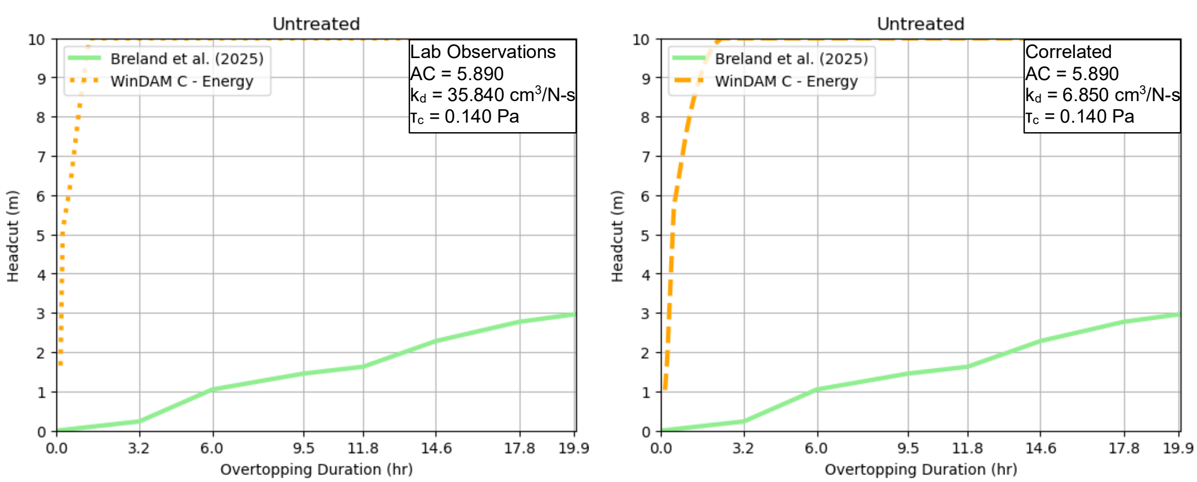

(a) (b)

Figure 50. Comparison of breach experiment headcut progression from WinDAM C energy model simulations using (a) lab-observed and (b) correlated input parameter sets for the untreated embankment against Breland et al. (2025) breach experiment measurements.

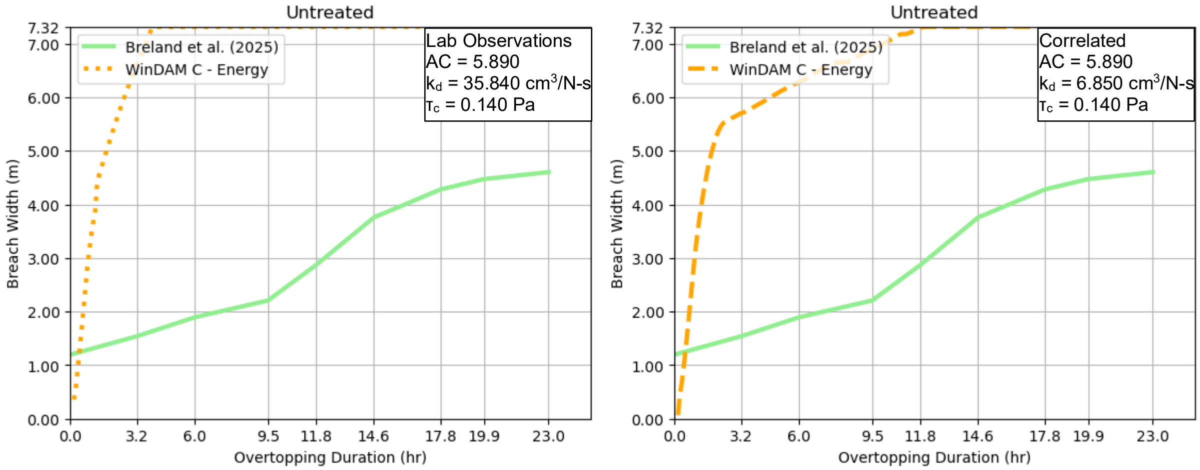

(a) (b)

Figure 51. Comparison of breach experiment breach widening progression from WinDAM C energy model simulations using (a) lab-observed and (b) correlated input parameter sets for the untreated embankment against Breland et al. (2025) breach experiment measurements.

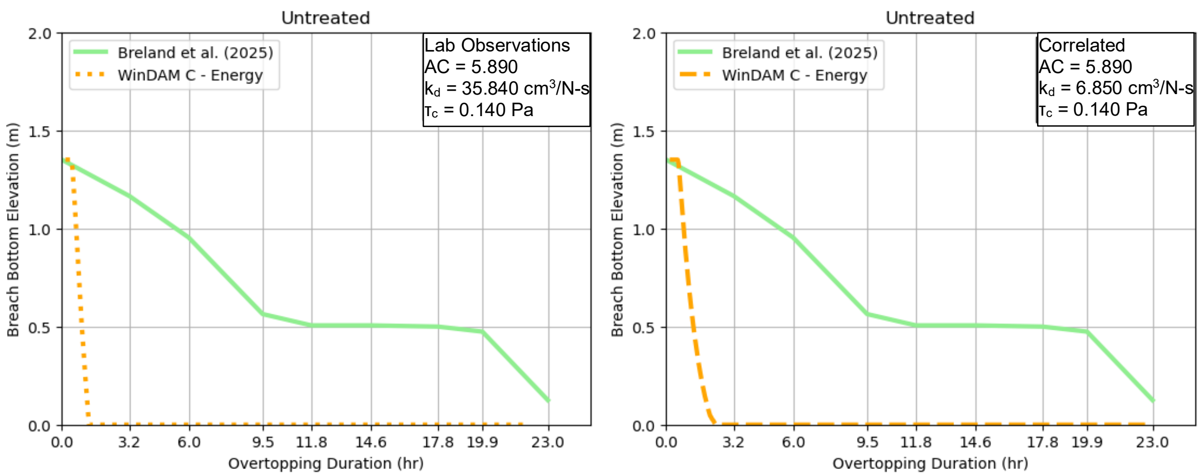

(a) (b)

Figure 52. Comparison of breach experiment hydraulic control progression from WinDAM C energy model simulations using (a) lab-observed and (b) correlated input parameter sets for the untreated embankment against Breland et al. (2025) breach experiment measurements.

4.4.2 WinDAM C Stress Model Results – Untreated Embankment

The breach experiment WinDAM C stress-based model results for the untreated embankment are shown in Figures 53-55. Headcut migration (Figure 53) advances rapidly across datasets, reaching the full toe-to-toe distance in ~1.5 hours for the lab-observed dataset and in ~12 hours for the correlated dataset. Breach widening (Figure

54) progresses faster in lab-observed data, spanning full crest length in ~4 hours, while correlated results are closer, but still overpredict observed final width by 42% (~6.1 meters). Breach deepening (Figure 55) mirrors headcut timing, hitting the embankment foundation in ~1.5 hours for the lab-observed and ~12 hours for the correlated.

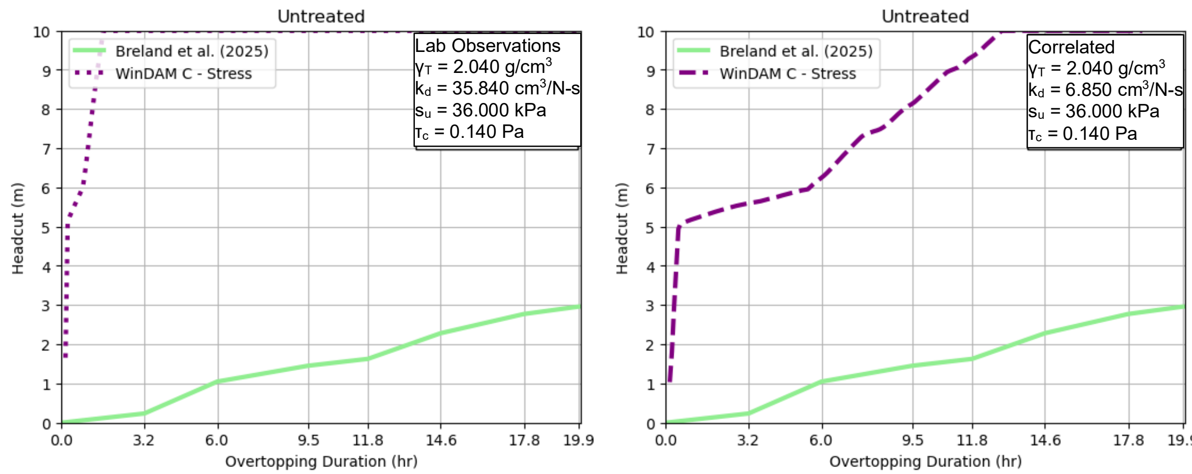

(a) (b)

Figure 53. Comparison of breach experiment headcut progression from WinDAM C stress model simulations using (a) lab-observed and (b) correlated input parameter sets for the untreated embankment against Breland et al. (2025) breach experiment measurements.

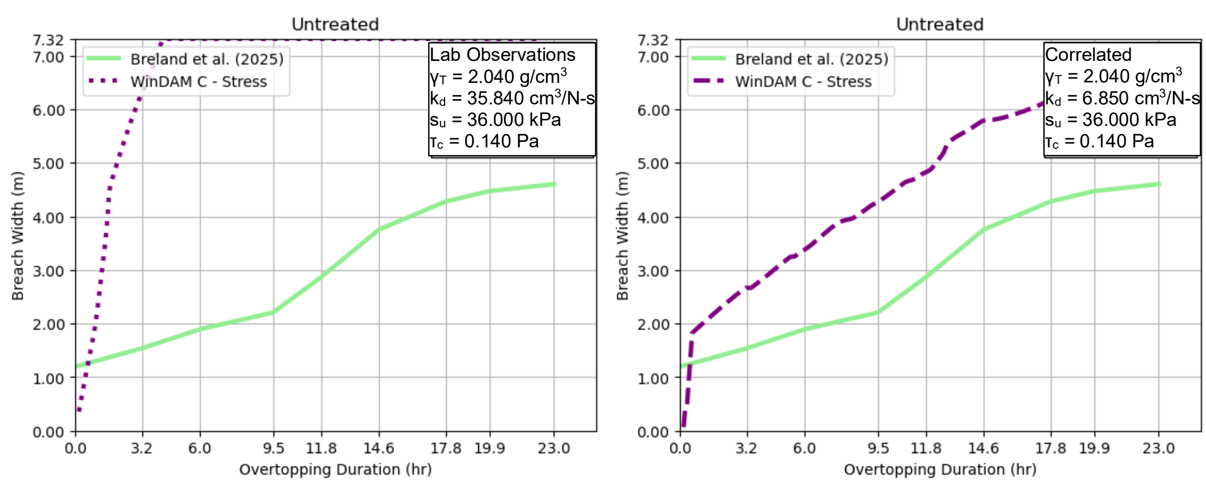

(a) (b)

Figure 54. Comparison of breach experiment breach widening progression from WinDAM C stress model simulations using (a) lab-observed and (b) correlated input parameter sets for the untreated embankment against Breland et al. (2025) breach experiment measurements.

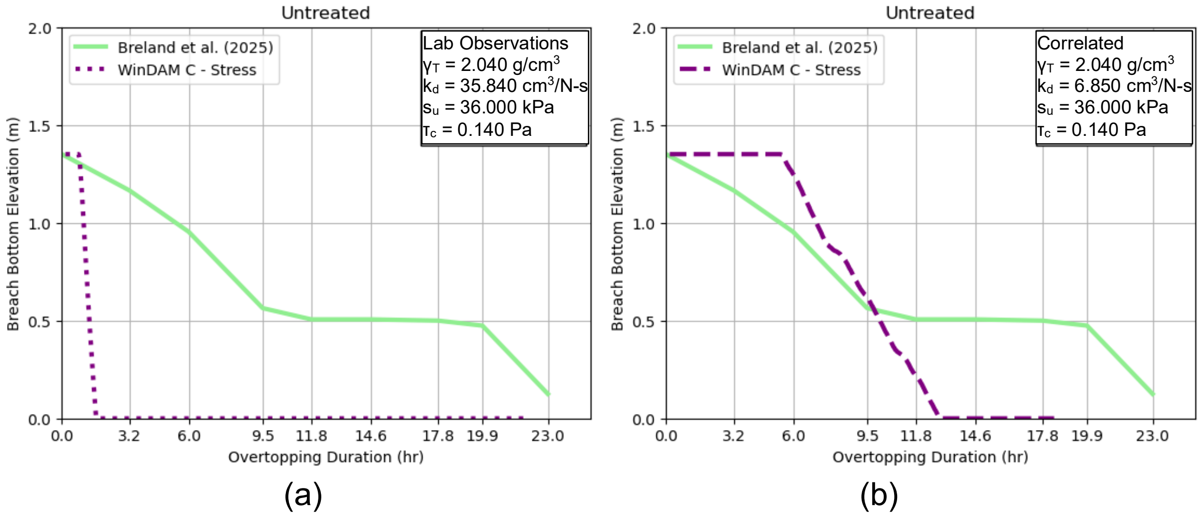

Figure 55. Comparison of breach experiment hydraulic control progression from WinDAM C stress model simulations using (a) lab-observed and (b) correlated input parameter sets for the untreated embankment against Breland et al. (2025) breach experiment measurements.

4.4.3 DLBreach Results – Untreated Embankment

The breach experiment results for the DLBreach model on the untreated embankment are shown in Figures 56-58. Headcut migration (Figure 56) advances rapidly across datasets, reaching the full toe-to-toe distance in ~1 hour for the lab-observed and ~4 hours for the correlated. Breach widening (Figure 57) shows contrasting predictions: lab-observed overpredicts final width by 42% (~6.1 meters), while correlated underpredicts by 21% (~3.7 meters). Breach deepening (Figure 58) reaches the embankment foundation rapidly in ~1 hour for the lab-observed) and ~7 hours for the correlated.

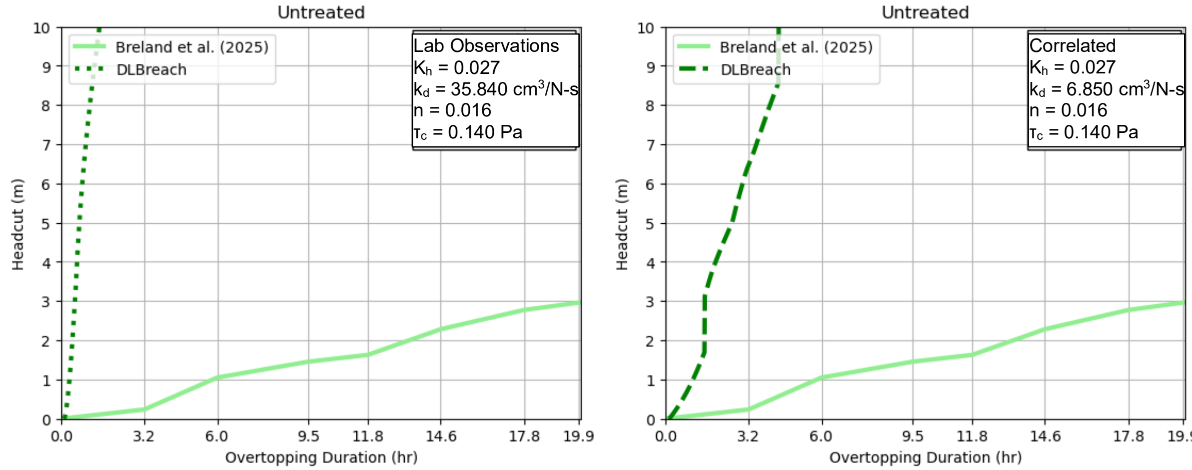

(a) (b)

Figure 56. Comparison of breach experiment headcut progression from DLBreach simulations using (a) lab-observed and (b) correlated input parameter sets for the untreated embankment against Breland et al. (2025) breach experiment measurements.

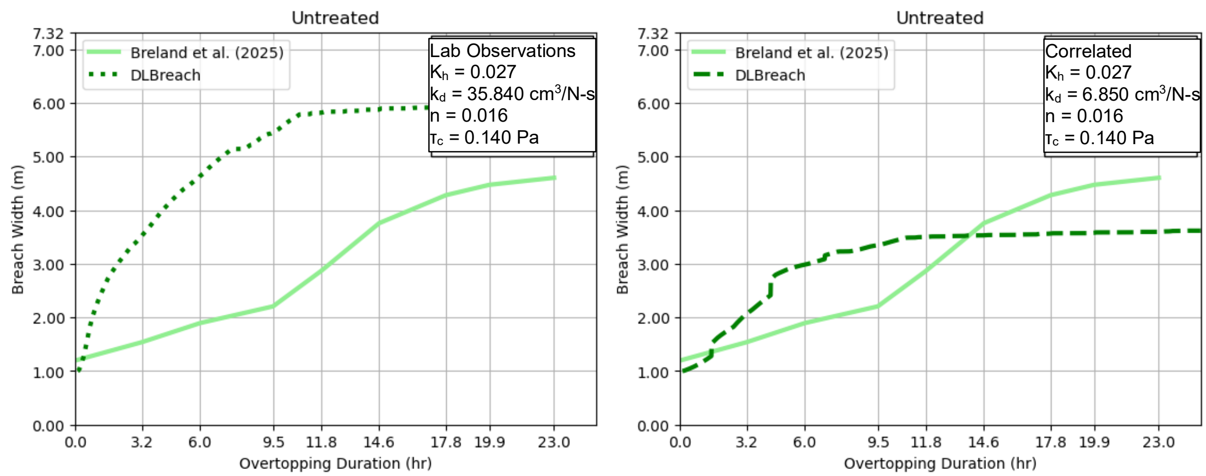

(a) (b)

Figure 57. Comparison of breach experiment breach widening progression from DLBreach simulations using (a) lab-observed and (b) correlated input parameter sets for the untreated embankment against Breland et al. (2025) breach experiment measurements.

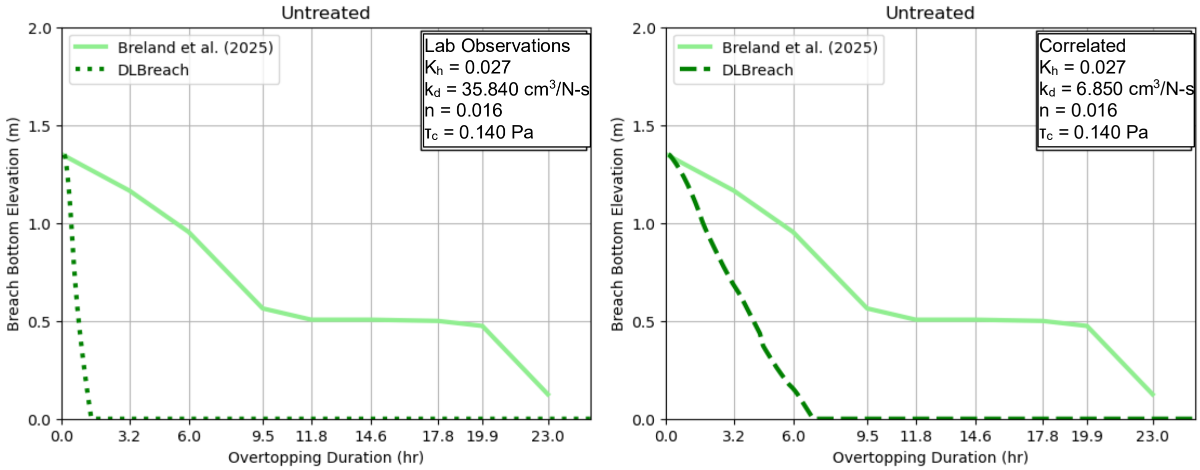

(a) (b)

Figure 58. Comparison of breach experiment hydraulic control progression from DLBreach simulations using (a) lab-observed and (b) correlated input parameter sets for the untreated embankment against Breland et al. (2025) breach experiment measurements.

4.4.4 WinDAM C Energy Model Results – Treated Embankment

The breach experiment WinDAM C energy-based model results for the treated embankment are shown in Figures 59-61. Headcut migration (Figure 59) advances rapidly across both datasets, reaching the full toe-to-toe distance in approximately 2 hours. Breach widening (Figure 60) progresses rapidly across datasets, reaching full toe-to-toe distance in ~17 hours for the lab-observed and ~12 hours for the correlated. Breach deepening (Figure 61) is similarly rapid, with the breach bottom hitting the embankment foundation in ~2 hours across datasets.

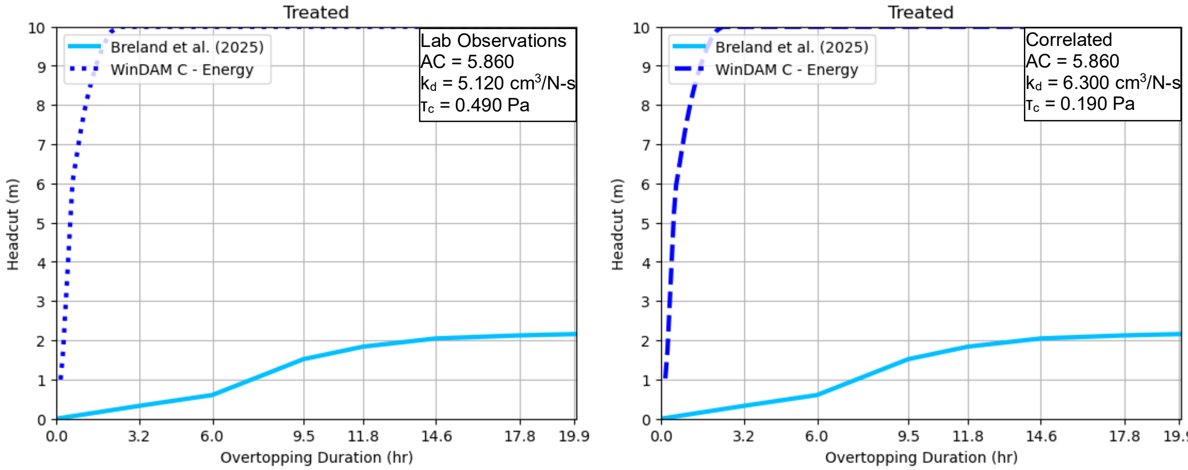

(a) (b)

Figure 59. Comparison of breach experiment headcut progression from WinDAM C energy model simulations using (a) lab-observed and (b) correlated input parameter sets for the treated embankment against Breland et al. (2025) breach experiment measurements.

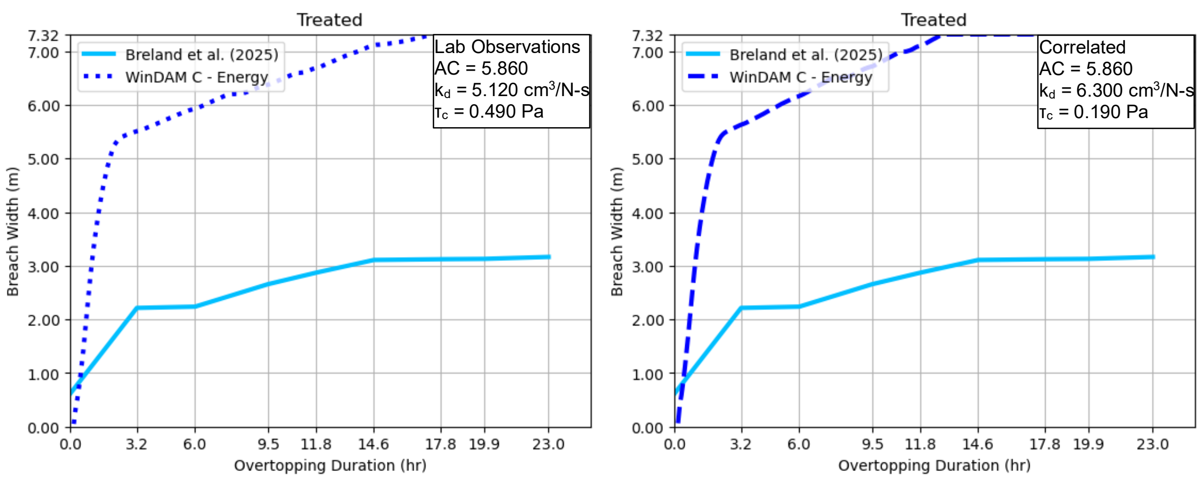

(a) (b)

Figure 60. Comparison of breach experiment breach widening progression from WinDAM C energy model simulations using (a) lab-observed and (b) correlated input parameter sets for the treated embankment against Breland et al. (2025) breach experiment measurements.

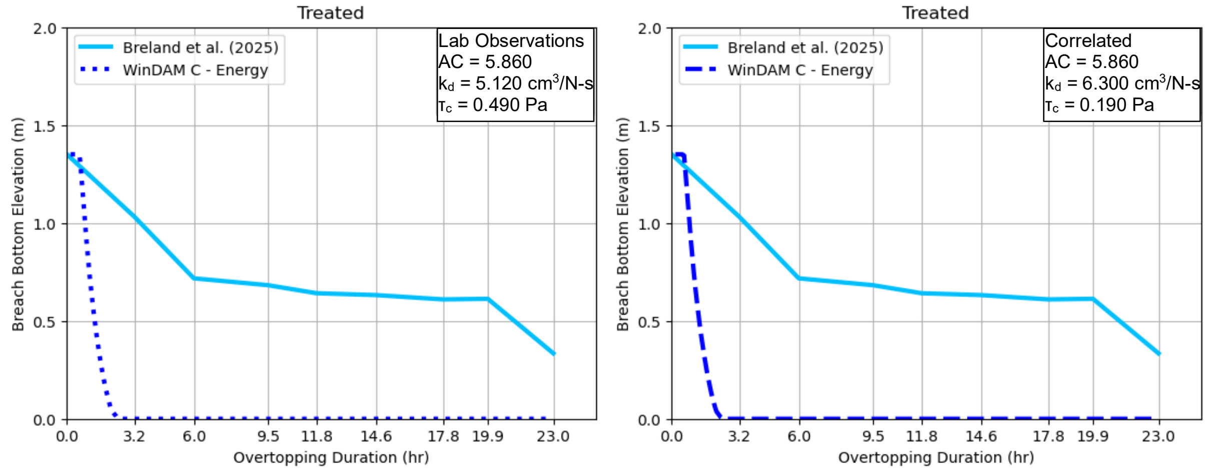

(a) (b)

Figure 61. Comparison of breach experiment hydraulic control progression from WinDAM C energy model simulations using (a) lab-observed and (b) correlated input parameter sets for the treated embankment against Breland et al. (2025) breach experiment measurements.

4.4.5 WinDAM C Stress Model Results – Treated Embankment

The breach experiment WinDAM C stress-based model results for the treated embankment are shown in Figures 62-64. Headcut migration (Figure 62) advances rapidly across datasets, reaching the full toe-to-toe distance in ~20 hours for the lab-observed versus ~14 hours for the correlated. Breach widening (Figure 63) overpredicts final observed width by ~100% (~5.9 meters for lab-observed and ~6.1 meters for correlated). Breach deepening (Figure 64) mirrors headcut timing, reaching the embankment foundation in ~20 hours for the lab-observed and ~14 hours for the correlated.

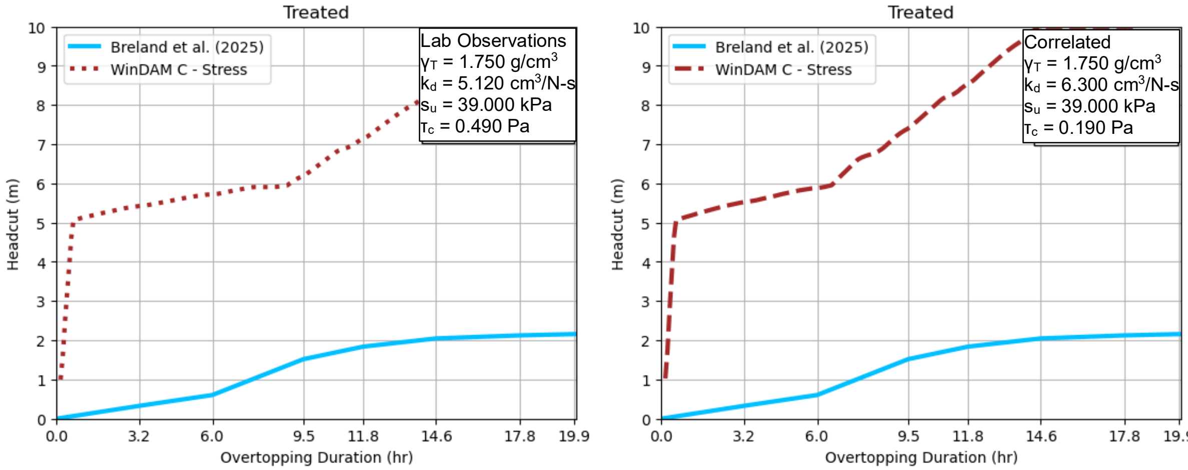

(a) (b)

Figure 62. Comparison of breach experiment headcut progression from WinDAM C stress model simulations using (a) lab-observed and (b) correlated input parameter sets for the treated embankment against Breland et al. (2025) breach experiment measurements.

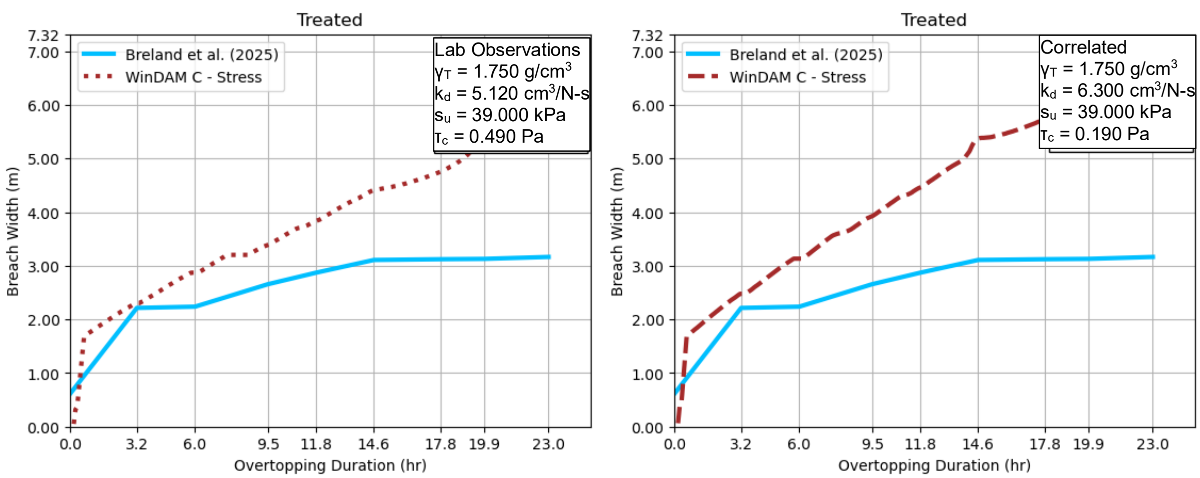

(a) (b)

Figure 63. Comparison of breach experiment breach widening progression from WinDAM C stress model simulations using (a) lab-observed and (b) correlated input parameter sets for the treated embankment against Breland et al. (2025) breach experiment measurements.

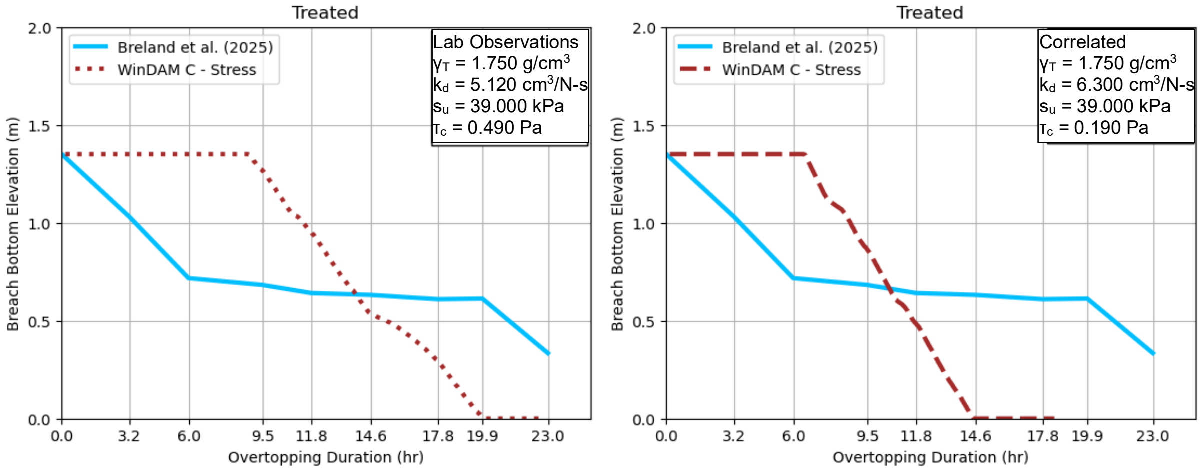

(a) (b)

Figure 64. Comparison of breach experiment hydraulic control progression from WinDAM C stress model simulations using (a) lab-observed and (b) correlated input parameter sets for the treated embankment against Breland et al. (2025) breach experiment measurements.

4.4.6 DLBreach Results – Treated Embankment

The breach experiment DLBreach model results for the treated embankment are shown in Figures 65-67. Headcut migration (Figure 65) advances rapidly across datasets, spanning full toe-to-toe distance in ~3 hours. Breach widening (Figure 66) shows overprediction at 77% for lab-observed (~5.5 meters) and 65% for correlated (~5.1 meters), while deepening (Figure 67) reaches the embankment foundation more slowly in lab-observed data (~12 hours) versus correlated (~10 hours).

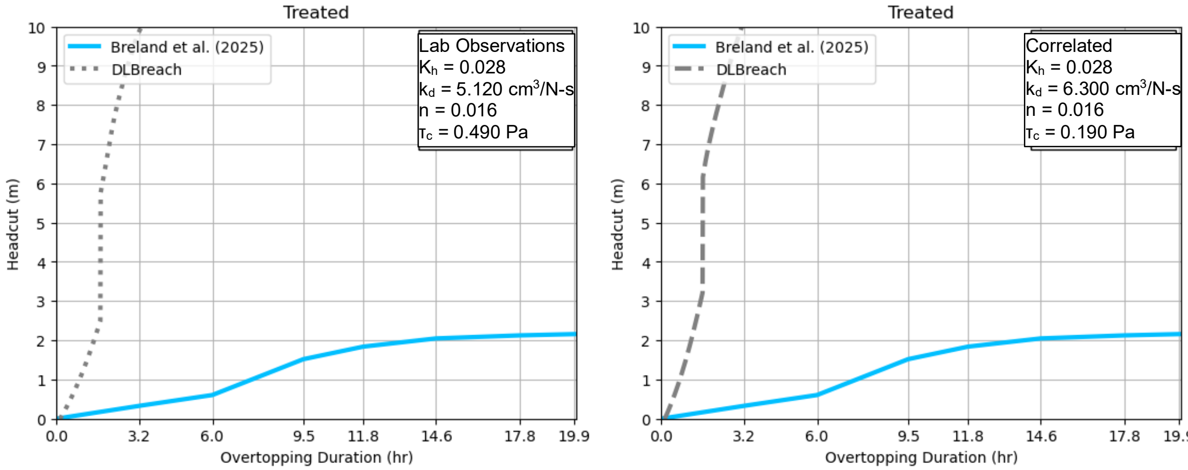

(a) (b)

Figure 65. Comparison of breach experiment headcut progression from DLBreach model simulations using (a) lab-observed and (b) correlated input parameter sets for the treated embankment against Breland et al. (2025) breach experiment measurements.

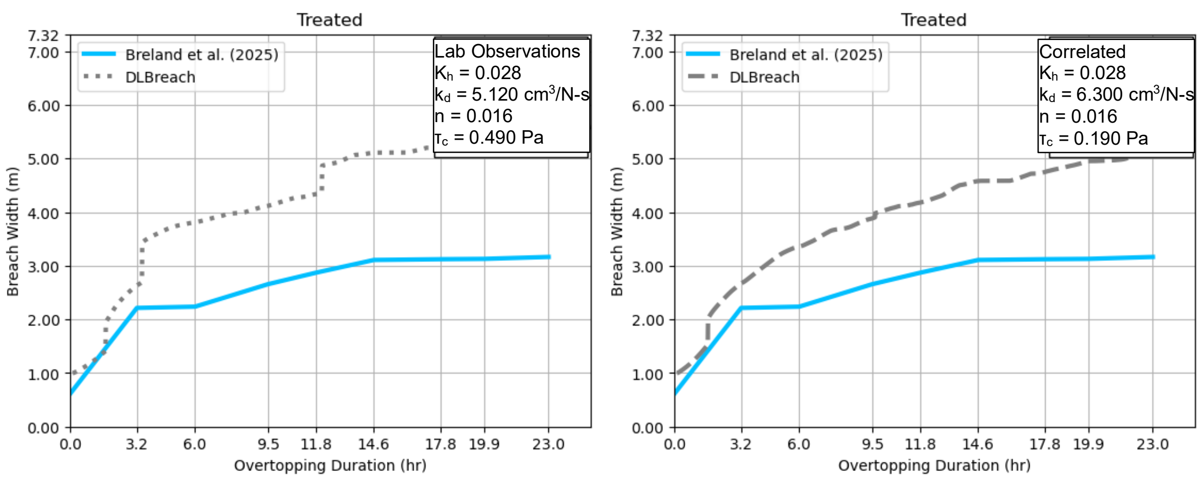

(a) (b)

Figure 66. Comparison of breach experiment breach widening progression from DLBreach model simulations using (a) lab-observed and (b) correlated input parameter sets for the treated embankment against Breland et al. (2025) breach experiment measurements.

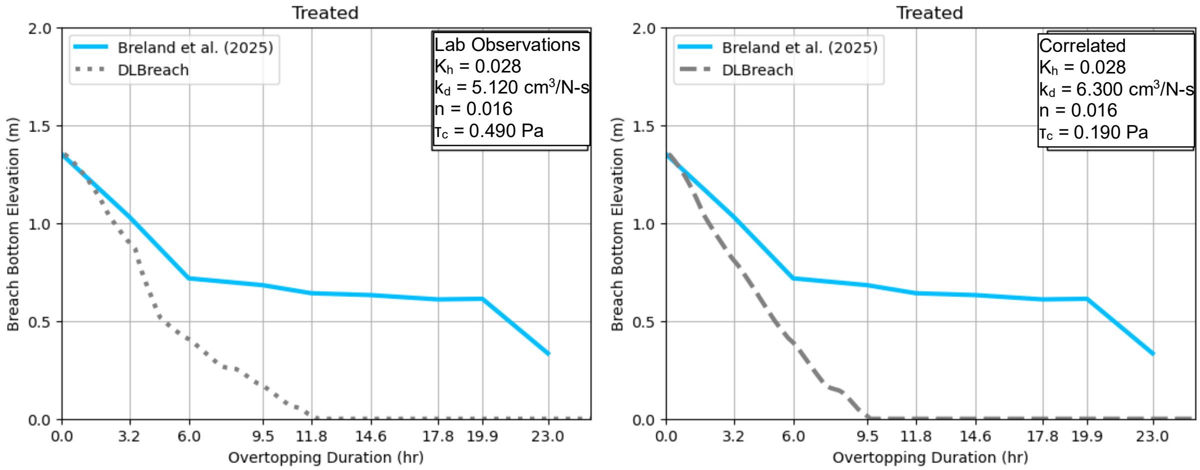

Figure 67. Comparison of breach experiment hydraulic control progression from DLBreach model simulations using (a) lab-observed and (b) correlated input parameter sets for the treated embankment against Breland et al. (2025) breach experiment measurements.

4.4.7 Summary

Overall, the breach experiment simulations demonstrated that all three models captured the general sequence of breach development, but none reproduced the observed headcut advance with high fidelity. A primary limitation is that the models represent headcut migration as a discrete, parameter-driven process, whereas the experimental breach likely involved overlapping field processes that evolved more continuously and interactively. As a result, all models overpredicted the timing of headcut progression and breach widening, with simulated headcut advance reaching toe-to-toe conditions approximately 2 to 12 hours earlier than observed and full crest widening occurring approximately 4 to 17 hours earlier than observed. The lab-observed k_d values generally produced the fastest erosion rates, while the correlated input sets slowed progression but still predicted breach development roughly ~100% to ~300% faster than measured.

Despite these discrepancies, the correlated inputs improved overall agreement relative to the laboratory-derived values in several cases, indicating that the correlation-based parameterization better moderates the erosion response. However, the persistent overprediction across all models suggests that the dominant limitation was not simply parameter selection, but the models' structural representation of erosion progression. Taken together, the breach experiment results show that the simulations were useful for capturing the overall direction of breach evolution, but they remained overly aggressive in predicting progression rates.

4.5 Breland et al. (2025) – Combined Overtopping-plus-Breach Simulations

The combined simulations in this section attempted to replicate the Breland et al. (2025) sequence: an initial overtopping inflow for erosion initiation, followed by continued overtopping for breach progression (Figure 14). The simulations were first run using the laboratory and correlated parameter sets described in Chapter 3 and then adjusted to develop a best-fit case for comparison with the observed data (Table 8). The resulting best-fit dataset reduced the differences between the simulated and observed hydrographs, breach evolution, and headcut migration by systematically adjusting the WinDAM C parameters VCF, RCI, k_d, τ_c, AC, and s_u. DLBreach was not calibrated for the combined overtopping-plus-breach experiment because it does not represent vegetation effects on erosion initiation, limiting its use to blind prediction and breach-only simulations. The parameters VCF, RCI, and τ_c were first adjusted to better match the onset of erosion at 33 hours, followed by k_d and AC/s_u to align final breach widths. Headcut progression was excluded from the best-fit evaluation because WinDAM C represents headcut migration differently than what was observed in the experiment, preventing any parameter combination from matching that response exactly.

4.5.1 WinDAM C Energy Model Results – Untreated Embankment

The WinDAM C energy-based model results for the combined overtopping-plus-breach experiment on the untreated embankment are presented in Figures 68-71. Simulated upstream water surface elevations (Figure 68) align closely with both lab-observed and correlated datasets up to approximately 25 hours, when the sharp drop marks erosion onset in those cases. The best-fit scenario intentionally shifts the initiation of erosion to the end of the overtopping phase (~33 hours) by adjusting vegetation/erosion resistance parameters. Specifically, the VCF was increased to 0.870, which is one cover class above the original (Table 3), enhancing resistance to initial erosion. The RCI was reduced to 2.880, which is one class lower (Table 2), simulating shorter/mowed grass that accelerates flow and early detachment. Following initiation, headcut migration (Figure 69) progresses rapidly, spanning the full toe-to-toe distance in about 3 hours for both lab-observed and correlated datasets, whereas the best-fit simulation requires approximately 16 hours. Calibration did not target headcut migration for best-fit matching, as the model demonstrated poor predictive reliability across all parameter sets, consistently overpredicting rates. Breach widening (Figure 70) advances fastest in the lab-observed data, reaching full crest length in roughly 3 hours, with the correlated dataset following at approximately 13 hours. For breach deepening (Figure 71), both lab-observed and correlated datasets exhibit rapid downcutting, with the breach bottom reaching the embankment foundation in about 2 hours. The best-fit case slows this process significantly to ~16 hours. Achieving best-fit alignment required substantial reductions in the erodible soil parameters, with k_d decreasing by ~90% relative to the lab-observed value and ~50% relative to the correlated value (to 3.530 cm^3/N-s), while AC decreased by ~92% to 0.500. The k_d value remains within the range reported by Ursic and Langendoen (2021), whereas the AC value is considerably lower and indicates behavior consistent with moderately hard rock (USDA 2001). This value is unrealistic for this material, demonstrating that the parameter adjustment is attempting to offset a more fundamental disagreement between the simulation and observations. These adjustments primarily controlled the final breach width prediction, while VCF and RCI helped delay erosion initiation.

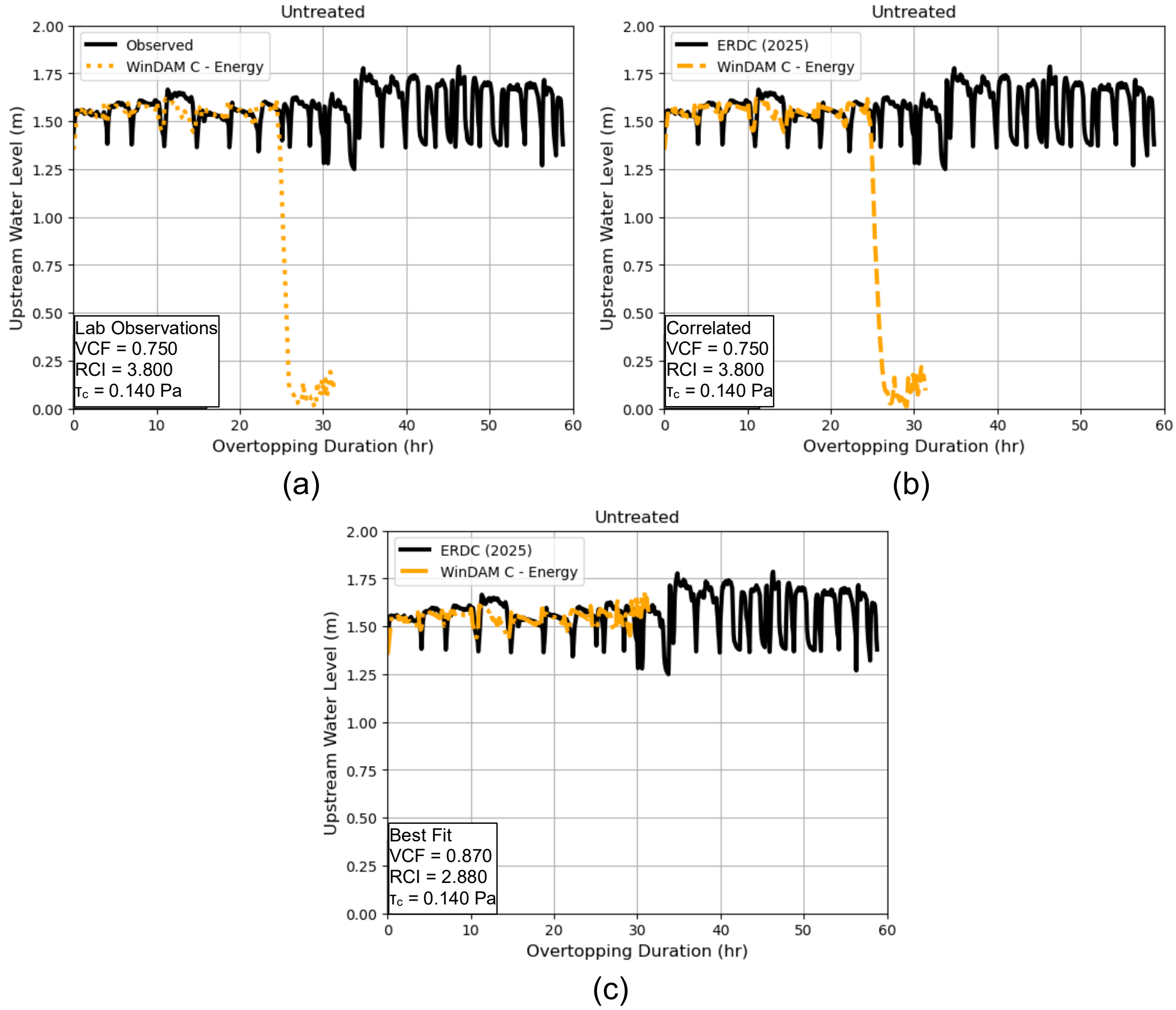

Figure 68. Comparison of combined overtopping-plus-breach experiment upstream water surface elevations from WinDAM C energy model simulations using (a) lab-observed, (b) correlated, and (c) best-fit input parameter sets for the untreated embankment against ERDC (2025) and Breland et al. (2025) experimental measurements.

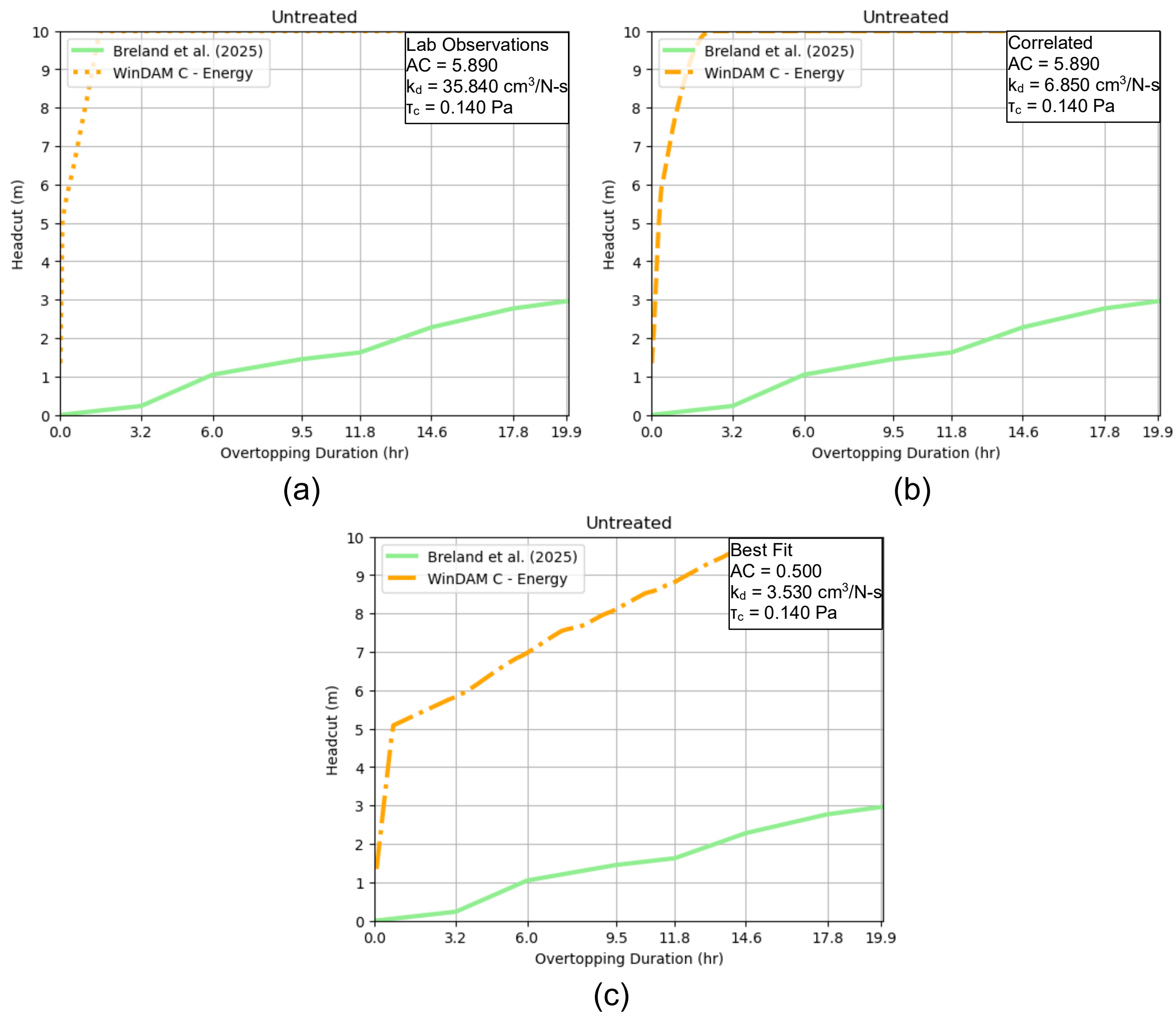

Figure 69. Comparison of combined overtopping-plus-breach experiment headcut progression from WinDAM C energy model simulations using (a) lab-observed, (b) correlated, and (c) best-fit input parameter sets for the untreated embankment against Breland et al. (2025) breach experiment measurements.

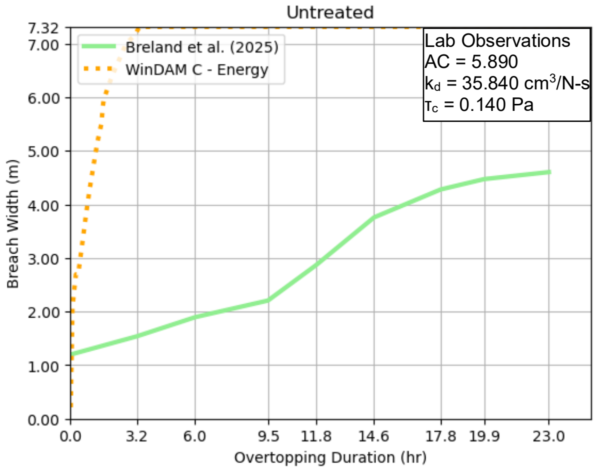

(a)

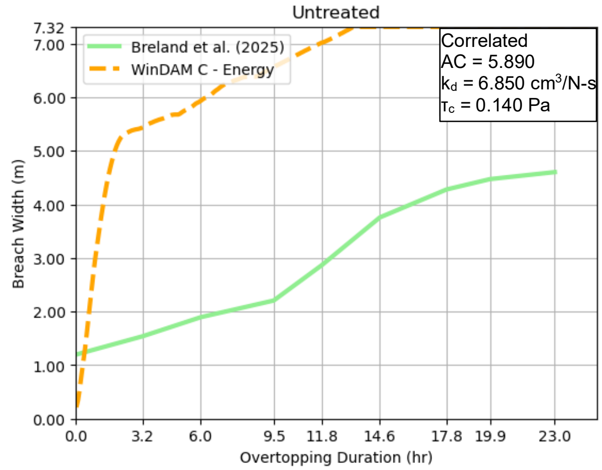

(b)

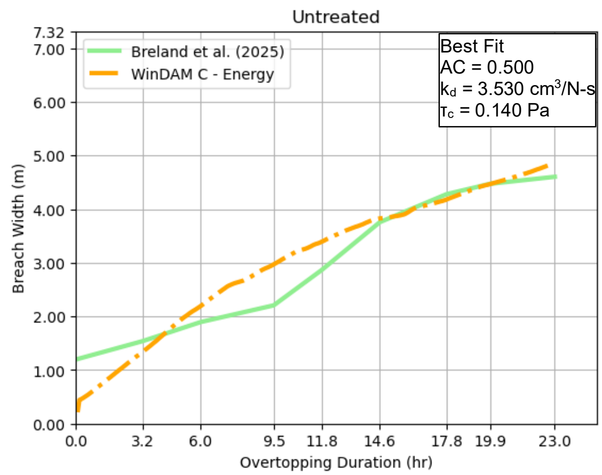

(c)

Figure 70. Comparison of combined overtopping-plus-breach experiment breach widening progression from WinDAM C energy model simulations using (a) lab-observed, (b) correlated, and (c) best-fit input parameter sets for the untreated embankment against Breland et al. (2025) breach experiment measurements.

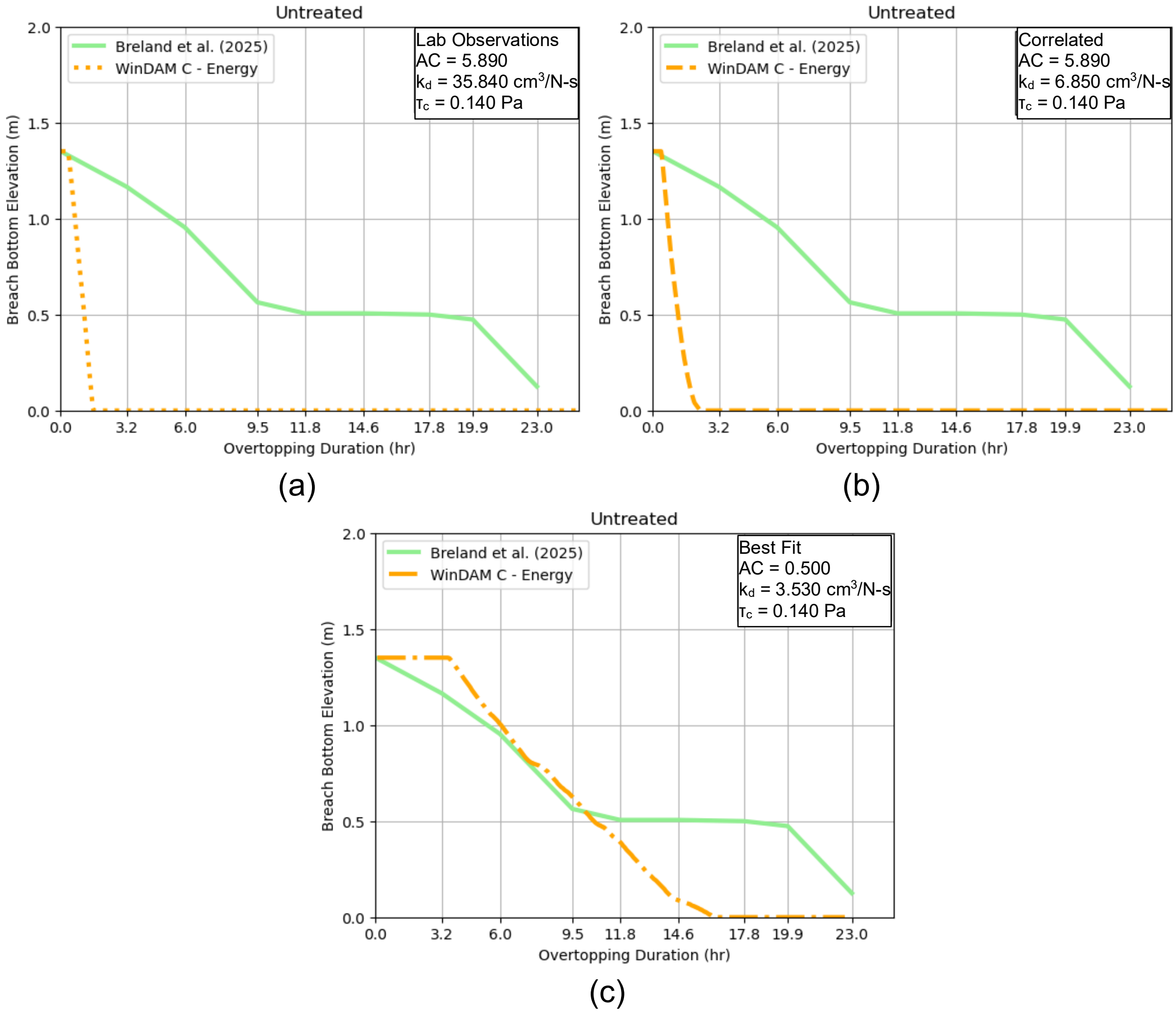

Figure 71. Comparison of combined overtopping-plus-breach experiment hydraulic control progression from WinDAM C energy model simulations using (a) lab-observed, (b) correlated, and (c) best-fit input parameter sets for the untreated embankment against Breland et al. (2025) breach experiment measurements.

4.5.2 WinDAM C Stress Model Results – Untreated Embankment

The WinDAM C stress-based model results for the combined overtopping-plus-breach experiment on the untreated embankment are presented in Figures 72-75. Simulated upstream water surface elevations (Figure 72) align closely with both the lab-observed and correlated datasets until approximately 25 hours, when erosion onset occurs, marked by a sharper drop in the lab-observed case due to its higher k_d. The best-fit scenario delays the initiation of this erosion until the end of the overtopping phase (~33 hours) by targeted adjustments to vegetation and erosion-resistance parameters. This adjustment is the same as for the energy model, as the initiation is independent of the headcut model. Following initiation, headcut migration (Figure 73) advances most rapidly in the lab-observed dataset, spanning the full toe-to-toe distance in about 2 hours, with the correlated dataset requiring approximately 12 hours. The best-fit simulation still overpredicts the final headcut substantially at ~8.6 meters (~200% relative to observations), but headcut migration was not calibrated in any scenario. Breach widening (Figure 74) proceeds fastest in the lab-observed data, achieving full crest length in roughly 5 hours, followed by the correlated dataset at approximately 13 hours. Breach deepening (Figure 75) shows the lab-observed dataset downcutting most rapidly to the embankment foundation in ~2 hours, with the correlated dataset reaching at ~13 hours. The best-fit simulation agrees with the observed final breach bottom elevation, but the progression process was different. Best-fit alignment required reductions in erodible soil parameters: k_d decreased by ~90% and ~50% relative to the lab-observed and correlated baselines, respectively (to 3.530 $cm^3/N\text{-}s$), while s_u was reduced by 7% from the original 36.000 kPa in both datasets (to ~33.500 kPa), indicating a slightly softer soil but still within the same consistency category (Peck et al. 1974). These k_d and s_u adjustments primarily controlled the final breach width.

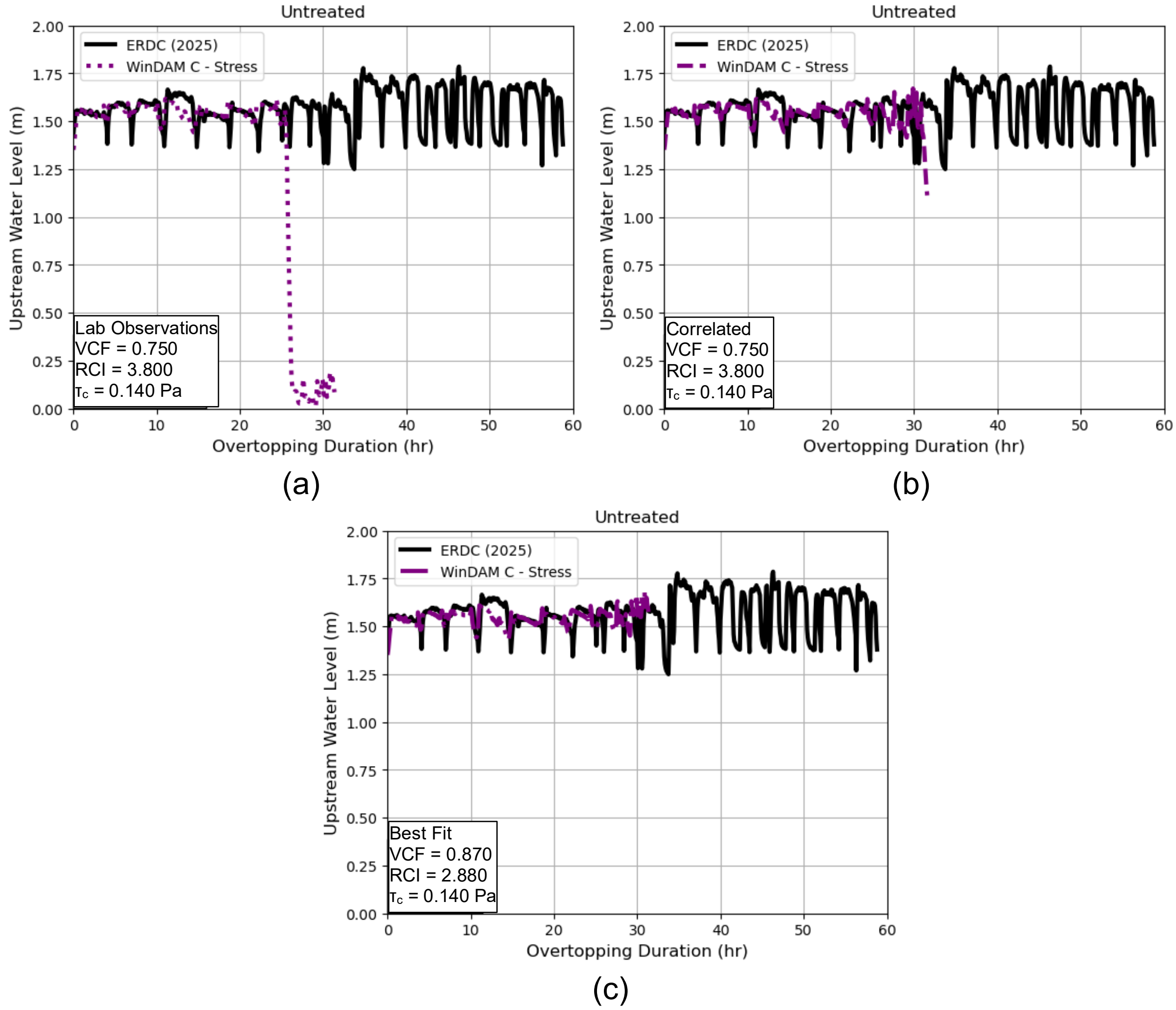

Figure 72. Comparison of combined overtopping-plus-breach experiment upstream water surface elevations from WinDAM C stress model simulations using (a) lab-observed, (b) correlated, and (c) best-fit input parameter sets for the untreated embankment against ERDC (2025) and Breland et al. (2025) experimental measurements.

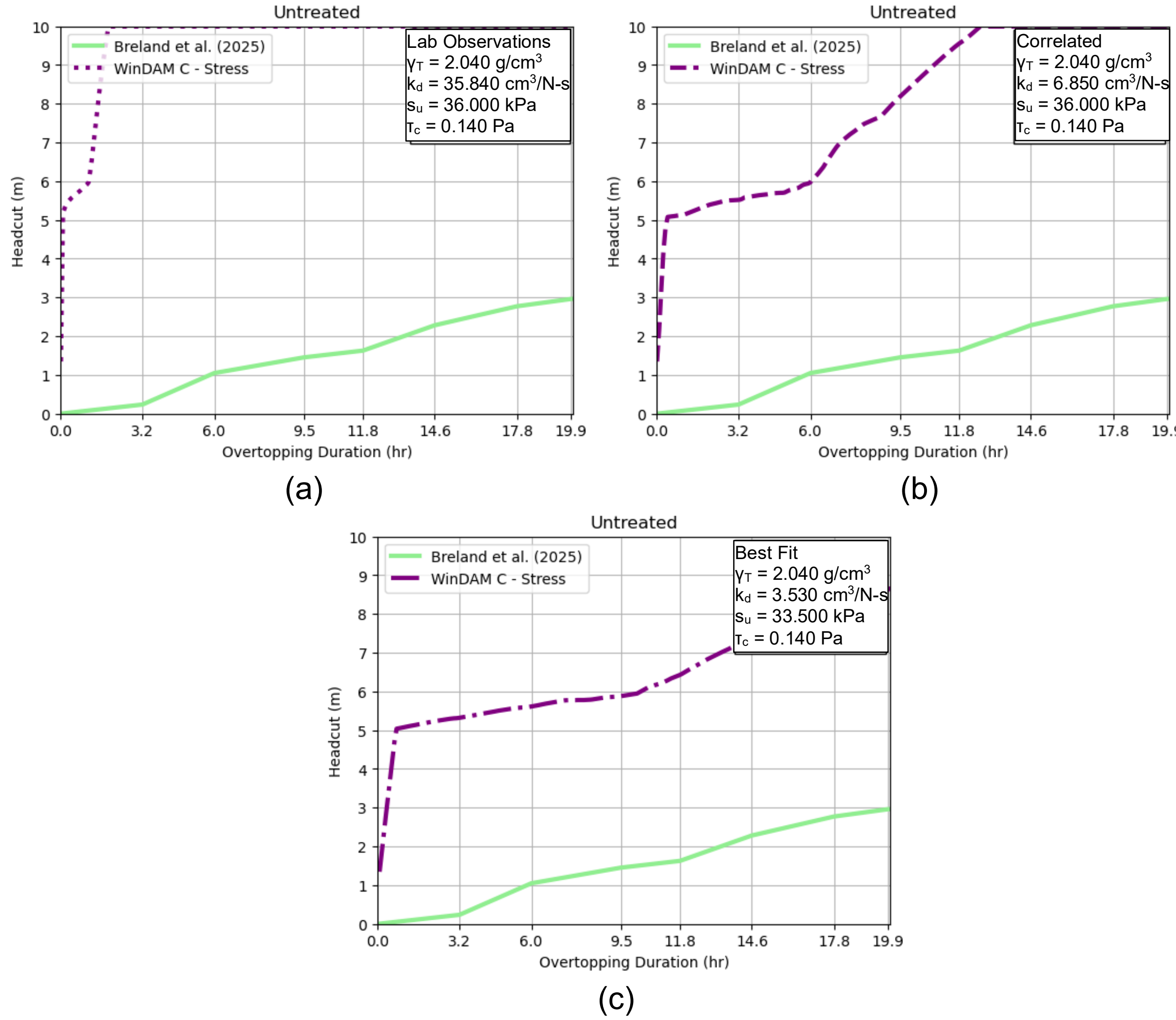

Figure 73. Comparison of combined overtopping-plus-breach experiment headcut progression from WinDAM C stress model simulations using (a) lab-observed, (b) correlated, and (c) best-fit input parameter sets for the untreated embankment against Breland et al. (2025) breach experiment measurements.

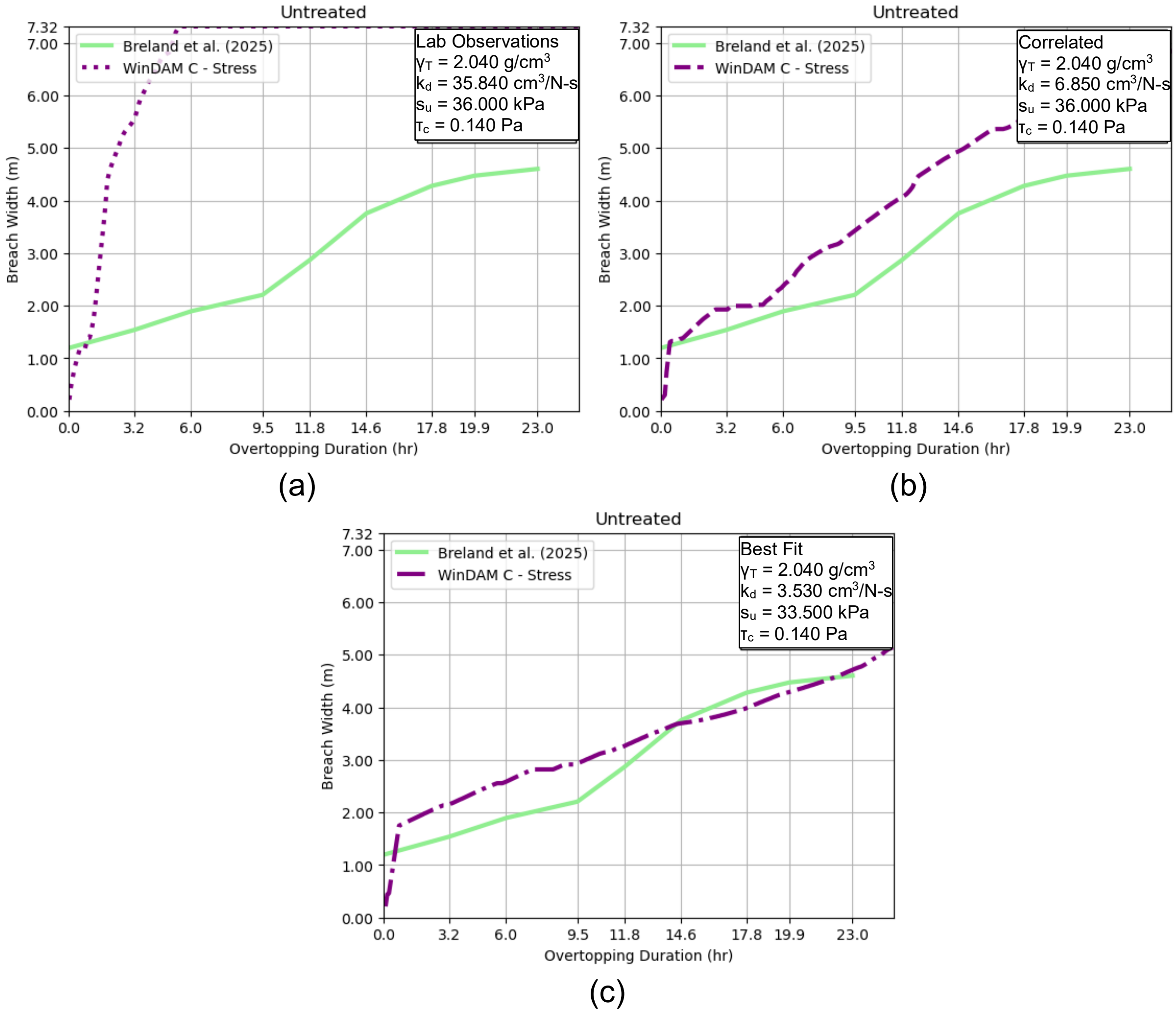

Figure 74. Comparison of combined overtopping-plus-breach experiment breach widening progression from WinDAM C stress model simulations using (a) lab-observed, (b) correlated, and (c) best-fit input parameter sets for the untreated embankment against Breland et al. (2025) breach experiment measurements.

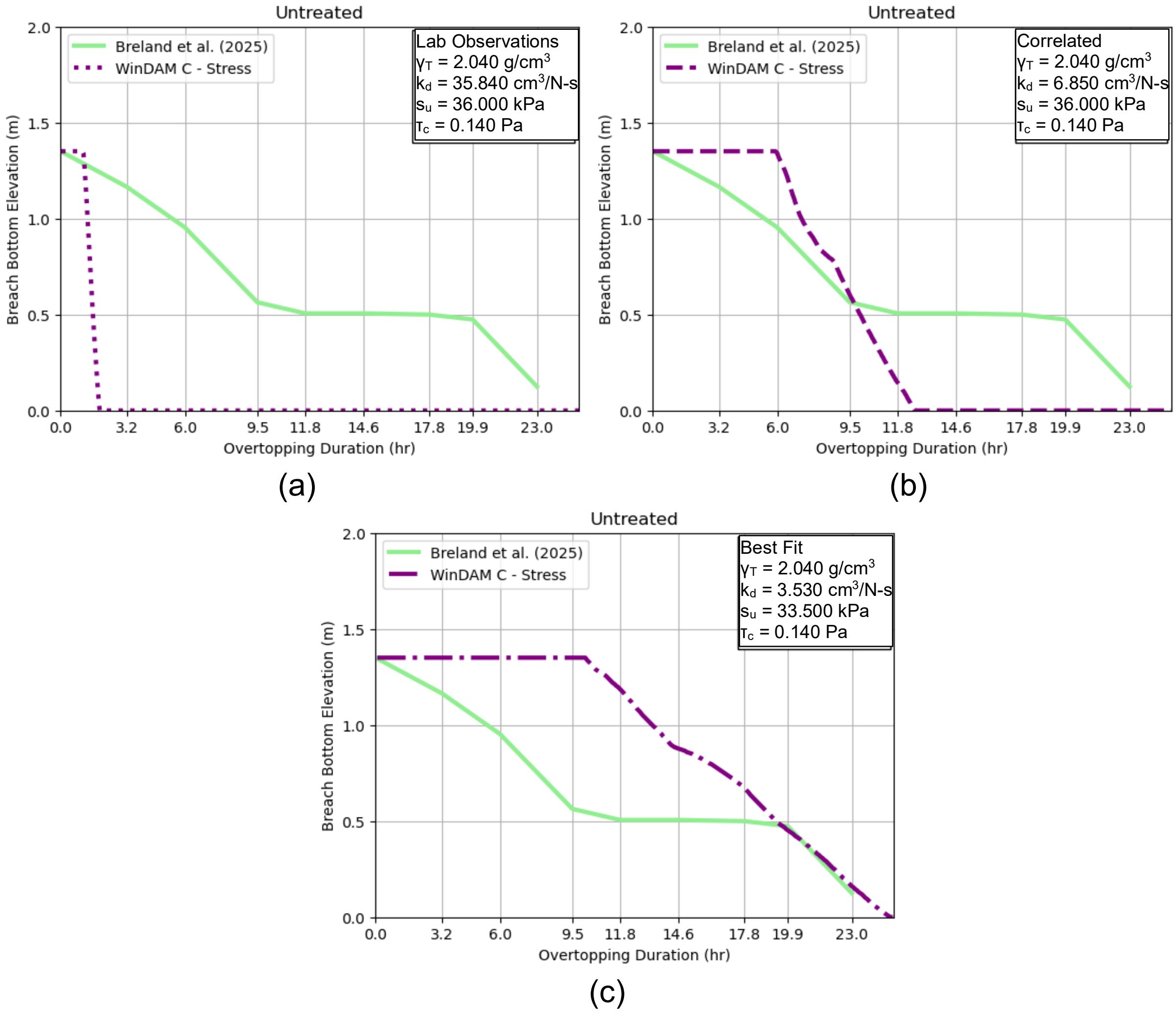

Figure 75. Comparison of combined overtopping-plus-breach experiment hydraulic control progression from WinDAM C stress model simulations using (a) lab-observed, (b) correlated, and (c) best-fit input parameter sets for the untreated embankment against Breland et al. (2025) breach experiment measurements.

4.5.3 WinDAM C Energy Model Results – Treated Embankment

The WinDAM C energy-based model results for the combined overtopping-plus-breach experiment on the treated embankment are presented in Figures 76-79. Simulated upstream water surface elevations (Figure 76) match the lab-observed and correlated datasets until ~30 hours, after which they exhibit a sharp drop, marking the onset of erosion. Best-fit delays initiation to overtopping end (~33 hours) via vegetation/erosion tweaks: VCF held at 0.750, RCI raised to 4.440 (Table 2), higher for taller grass and flow deceleration, and τ_c set to 0.340. Although vegetation was uniformly distributed across the treated and untreated halves, the best-fit values of VCF and RCI likely reflect uncertainty in the modeled distribution of overtopping flow between the two halves. Because the experimental data did not provide side-specific flow measurements, these parameter adjustments were intentionally used during calibration but may also partly compensate for limitations in the assumed flow partitioning. Following initiation, headcut migration (Figure 77) covers toe-to-toe distance in ~2 hours for lab-observed and correlated cases. The best-fit overpredicts ~350% (~9.75 meters). The headcut remains uncalibrated because the model consistently overpredicts across all runs. Breach widening (Figure 78) shows the correlated dataset widening fastest (~12 hours to full crest), ahead of the lab-observed dataset (~15 hours), due to a higher k_d (lab-observed: 5.120 cm^3/N-s vs. correlated: 6.300 cm^3/N-s). Lab-observed and correlated datasets deepen to the foundation in ~2 hours (Figure 79), and the best-fit dataset extends, reaching the foundation in ~20 hours post-initiation. Achieving the best fit required reducing k_d by 58% relative to the lab-observed value and reducing AC by 95%. Again, the k_d value remains within the range reported by Ursic and Langendoen (2021), whereas the AC value is considerably lower and indicates behavior consistent with hard rock (USDA 2001). This unrealistic AC value again demonstrates that the parameter adjustment is compensating for other factors.

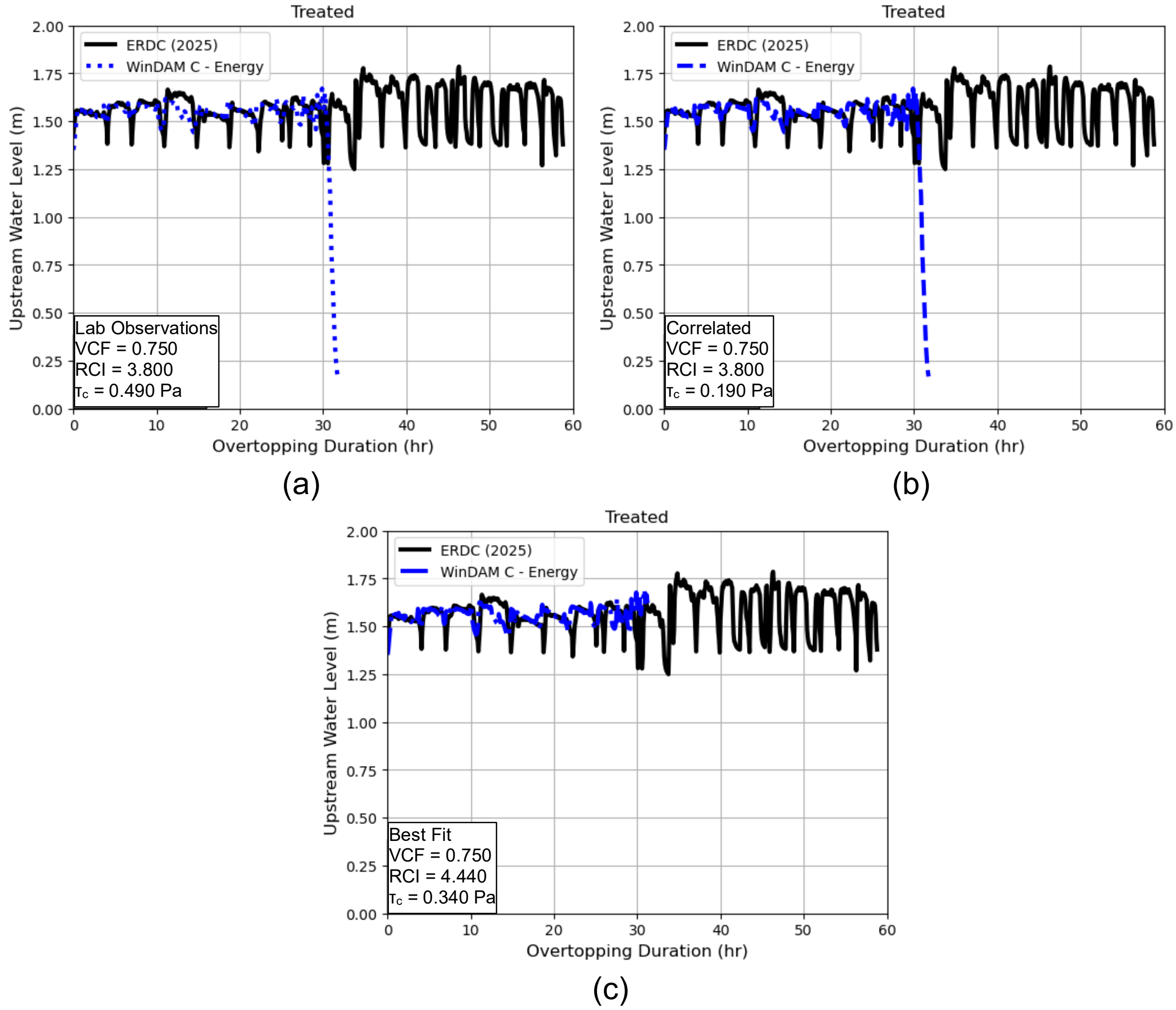

Figure 76. Comparison of combined overtopping-plus-breach experiment upstream water surface elevations from WinDAM C energy model simulations using (a) lab-observed, (b) correlated, and (c) best-fit input parameter sets for the treated embankment against ERDC (2025) and Breland et al. (2025) experimental measurements.

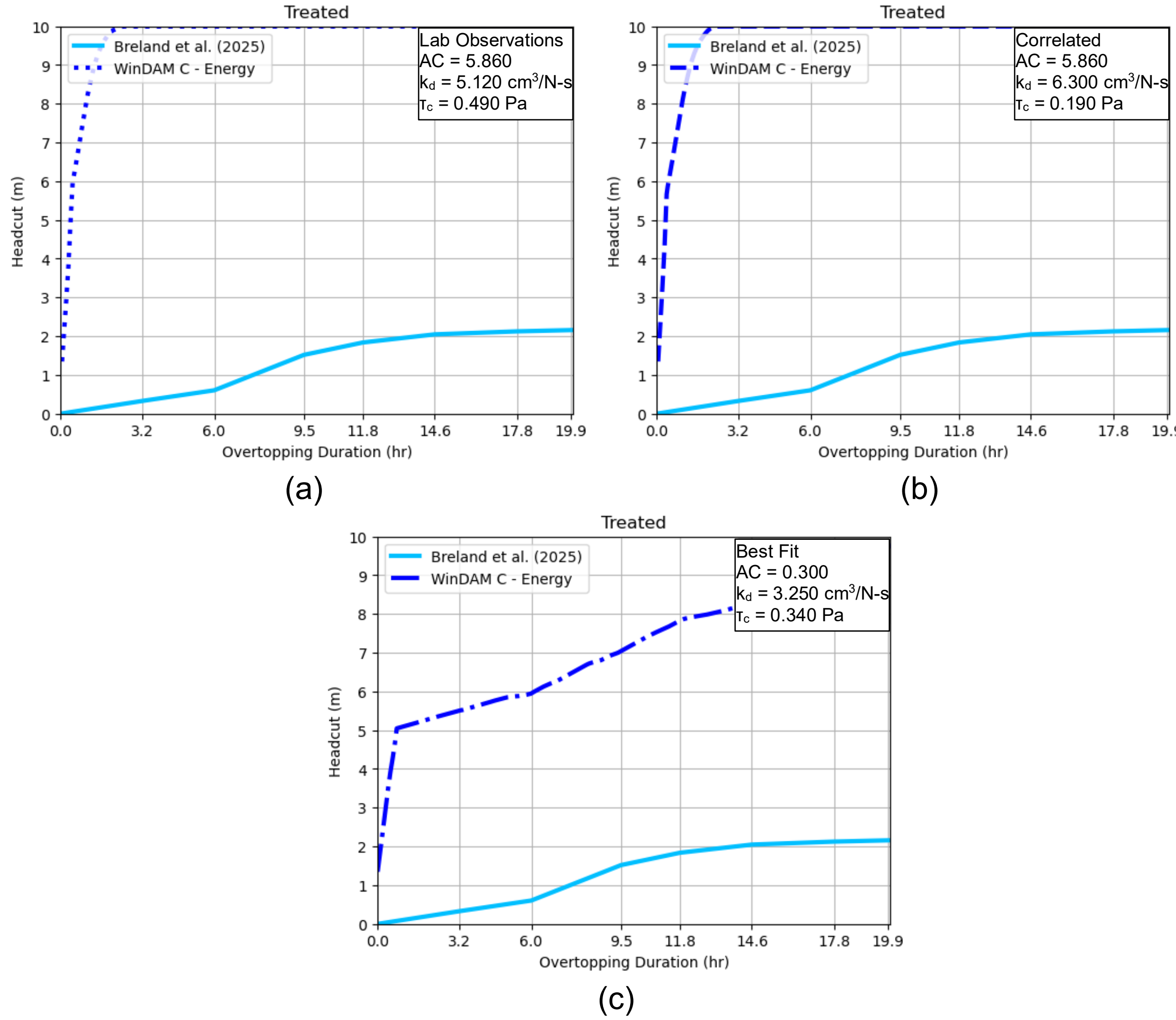

Figure 77. Comparison of combined overtopping-plus-breach experiment headcut progression from WinDAM C energy model simulations using (a) lab-observed, (b) correlated, and (c) best-fit input parameter sets for the treated embankment against Breland et al. (2025) breach experiment measurements.

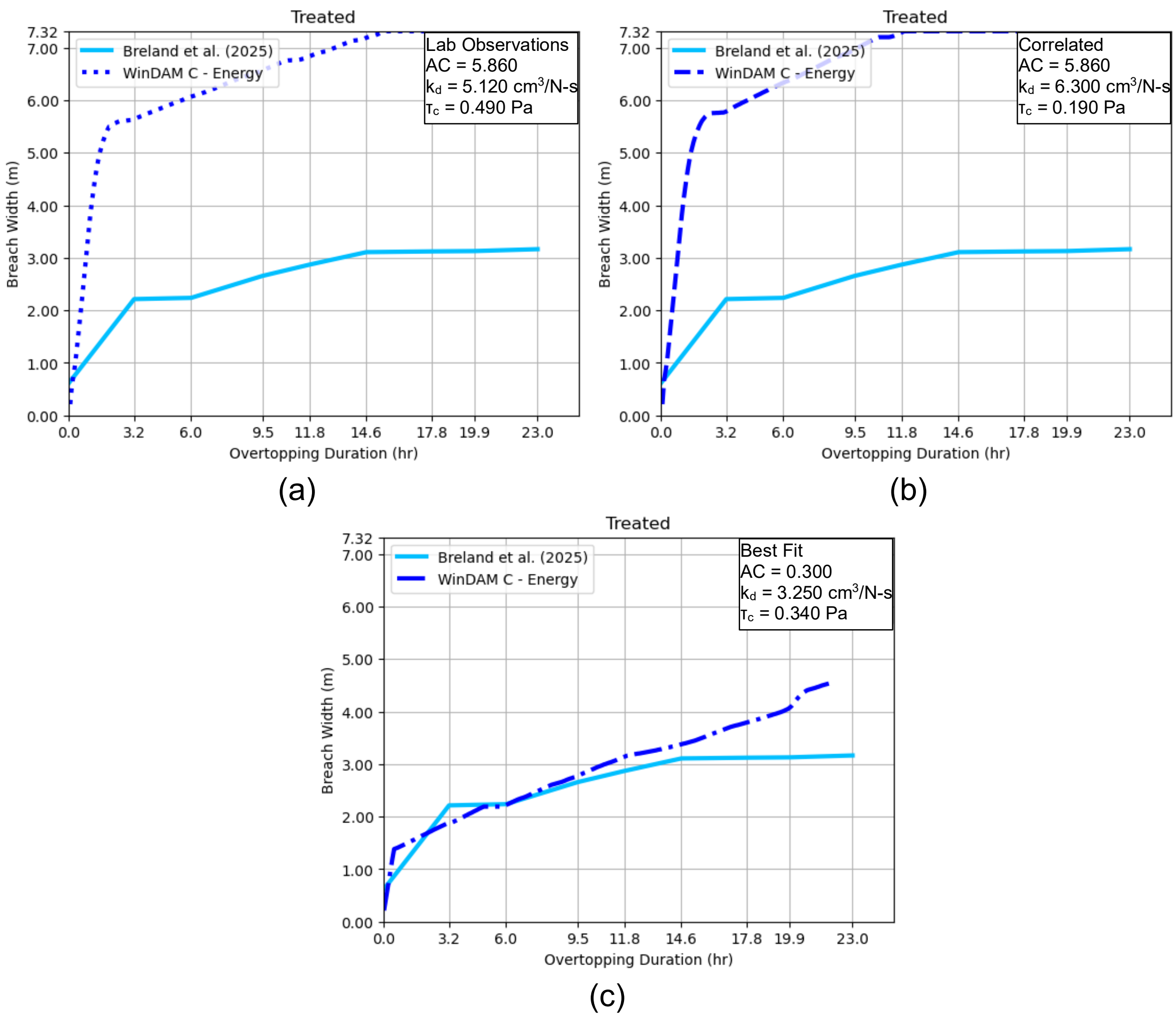

Figure 78. Comparison of combined overtopping-plus-breach experiment breach widening progression from WinDAM C energy model simulations using (a) lab-observed, (b) correlated, and (c) best-fit input parameter sets for the treated embankment against Breland et al. (2025) breach experiment measurements.

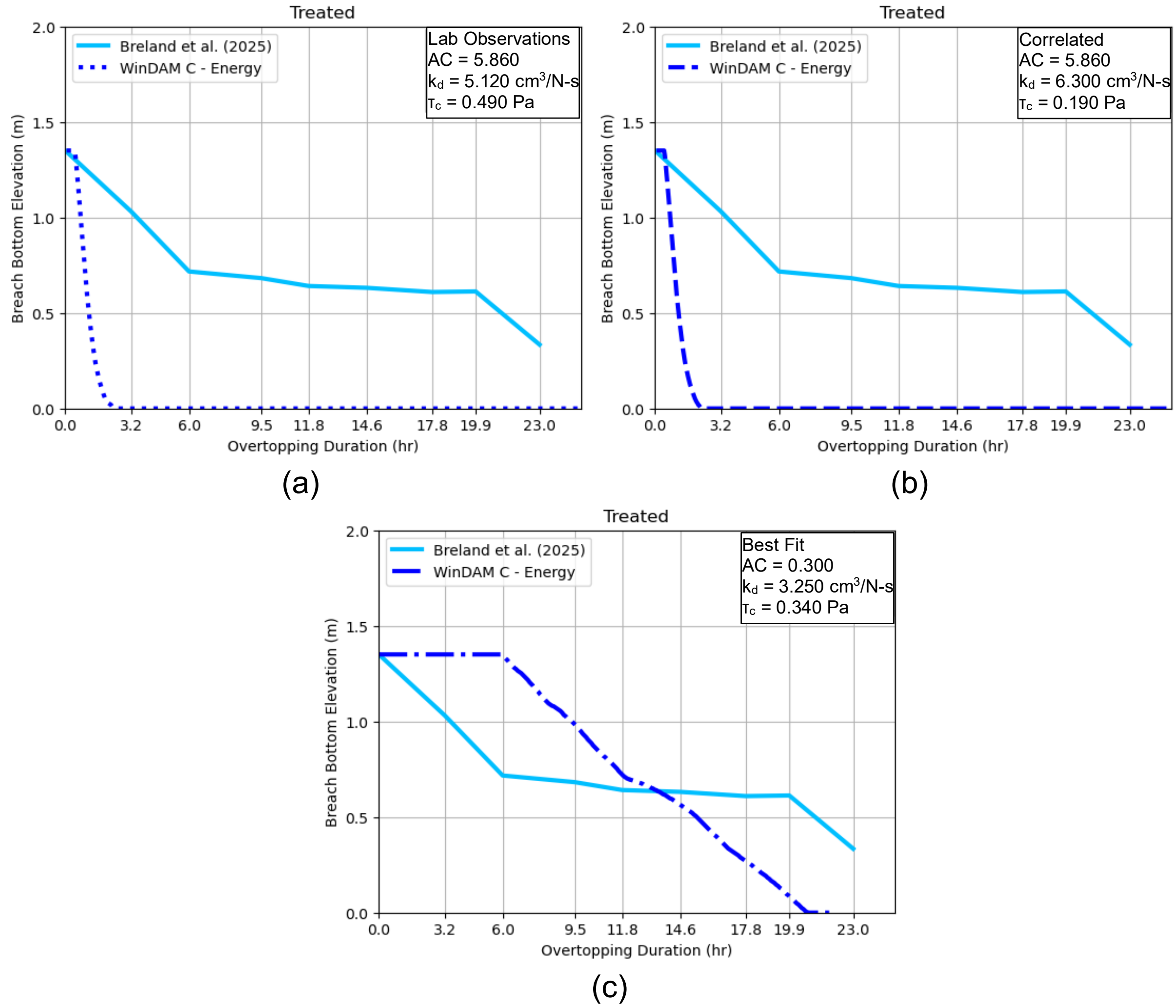

Figure 79. Comparison of combined overtopping-plus-breach experiment hydraulic control progression from WinDAM C energy model simulations using (a) lab-observed, (b) correlated, and (c) best-fit input parameter sets for the treated embankment against Breland et al. (2025) breach experiment measurements.

4.5.4 WinDAM C Stress Model Results – Treated Embankment

The WinDAM C stress-based model results for the combined overtopping-plus-breach experiment on the treated embankment are presented in Figures 80-83. Simulated upstream water surface elevations (Figure 80) match lab-observed and correlated datasets until ~30 hours, when erosion begins with water-level fluctuations. Best-fit approximately delays onset to the overtopping end (~33 hours) using identical vegetation tweaks as the treated energy model: VCF constant at 0.750, RCI at 4.440, and τ_c at 0.340 Pa. Headcut migration (Figure 81) advances fastest in the correlated dataset (~16 hours to full toe-to-toe distance), while the lab-observed overpredicts ~400% (~9.2 meters), and the best-fit overpredicts greater than 300% (~8.7 meters). As before, headcut was excluded from calibration due to the model's consistent unreliability. The correlated dataset widens most rapidly, overpredicting by ~100% (~6.2 meters) compared with lab-observed (<100%, ~5.7 meters) (Figure 82). The correlated dataset deepens fastest to the foundation (~16 hours), whereas the lab-observed dataset is slower (~22 hours) (Figure 83). The best-fit roughly matches the observed final breach bottom elevation. Achieving the best-fit condition required reducing k_d by 58% from the lab-observed value. The s_u reduced by ~2% from the original 39.000 kPa in both datasets to 38.300 kPa. These adjustments are all reasonable given the uncertainty in these parameters.

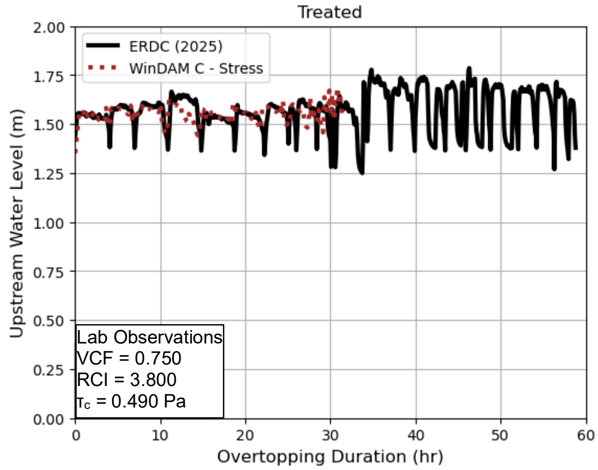

(a)

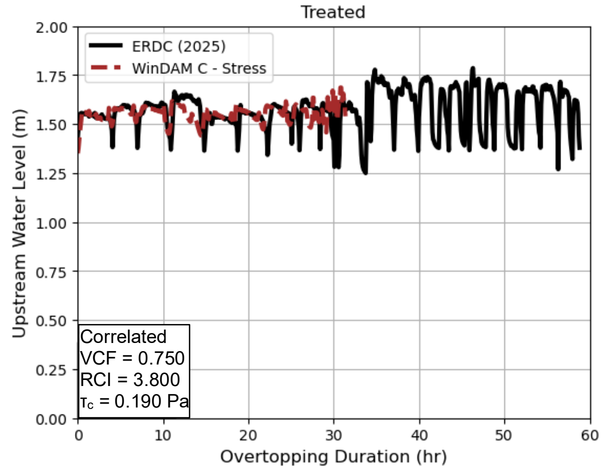

(b)

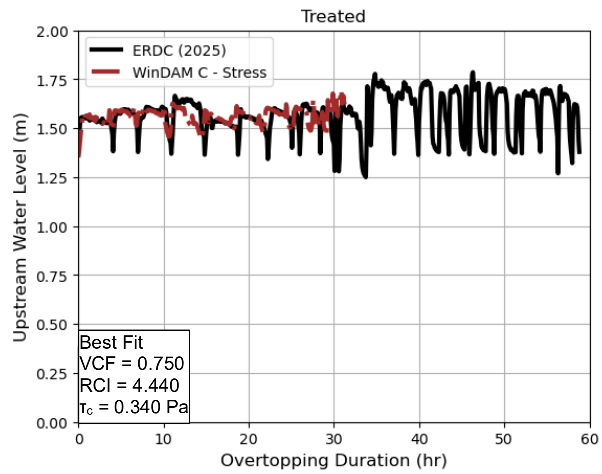

(c)

Figure 80. Comparison of combined overtopping-plus-breach experiment upstream water surface elevations from WinDAM C stress model simulations using (a) lab-observed, (b) correlated, and (c) best-fit input parameter sets for the treated embankment against ERDC (2025) and Breland et al. (2025) experimental measurements.

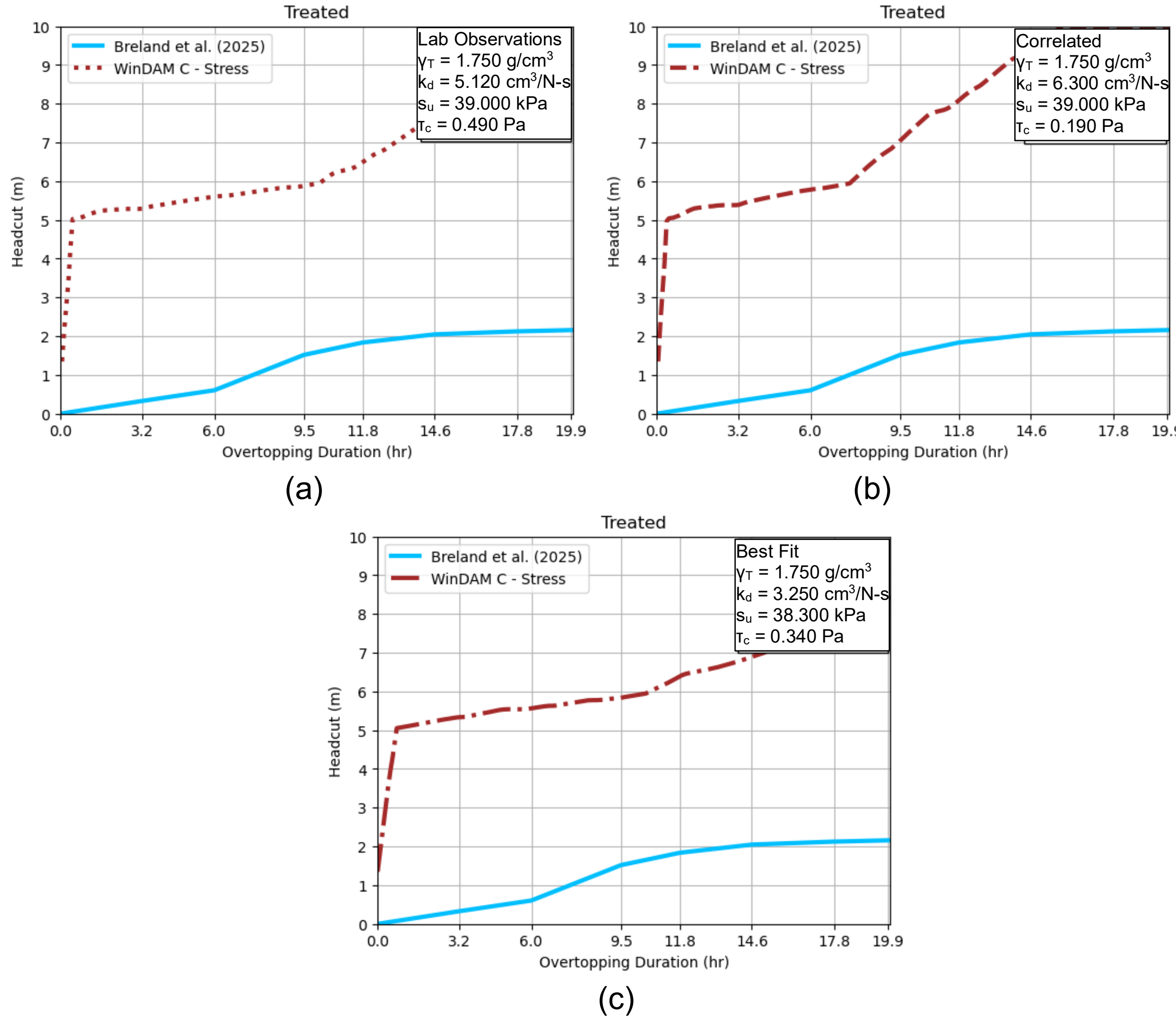

Figure 81. Comparison of combined overtopping-plus-breach experiment headcut progression from WinDAM C stress model simulations using (a) lab-observed, (b) correlated, and (c) best-fit input parameter sets for the treated embankment against Breland et al. (2025) breach experiment measurements.

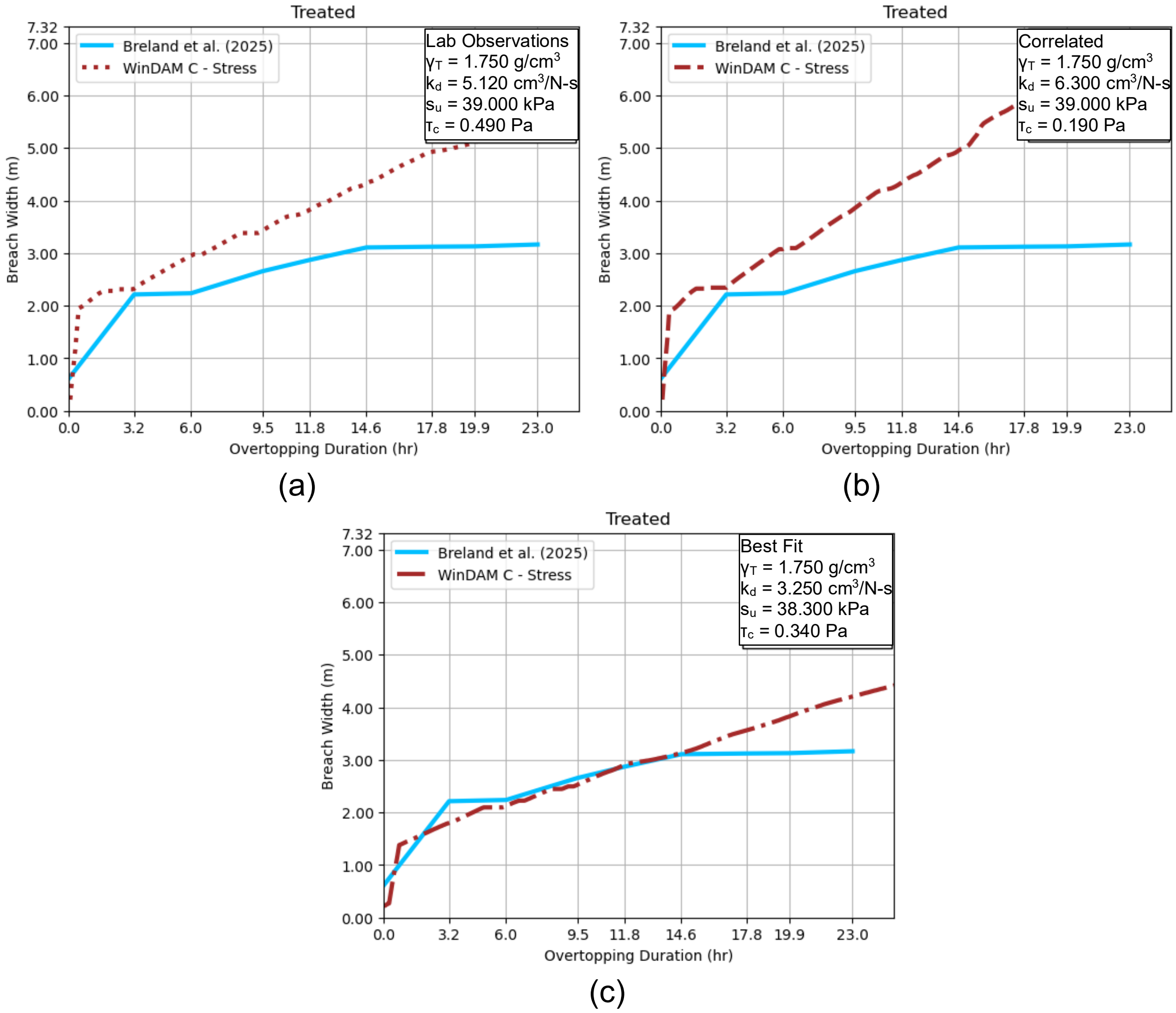

Figure 82. Comparison of combined overtopping-plus-breach experiment breach widening progression from WinDAM C stress model simulations using (a) lab-observed, (b) correlated, and (c) best-fit input parameter sets for the treated embankment against Breland et al. (2025) breach experiment measurements.

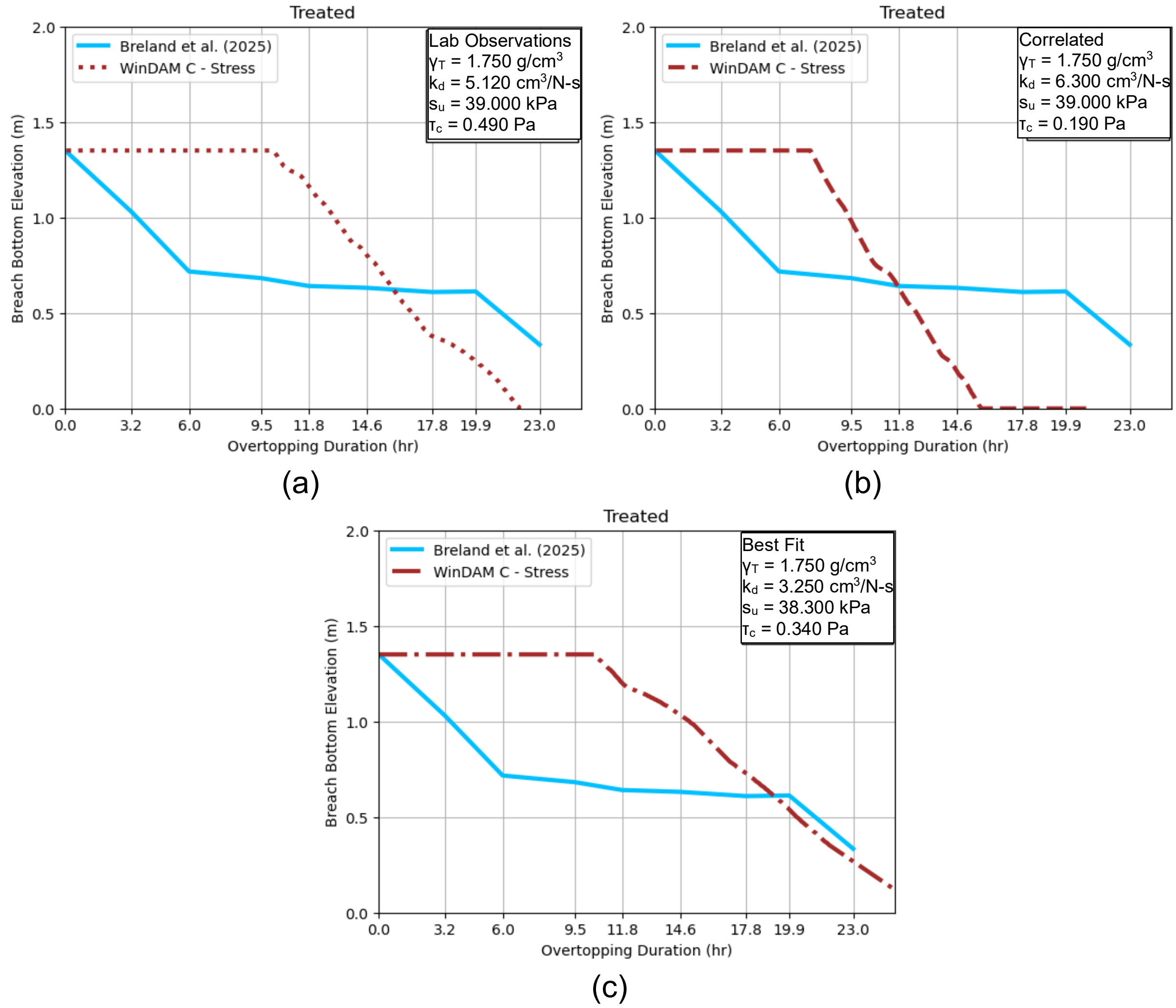

Figure 83. Comparison of combined overtopping-plus-breach experiment hydraulic control progression from WinDAM C stress model simulations using (a) lab-observed, (b) correlated, and (c) best-fit input parameter sets for the treated embankment against Breland et al. (2025) breach experiment measurements.

4.5.5 Summary

Overall, the combined overtopping-plus-breach simulations reproduced the general sequence of erosion initiation, headcut advance, and breach enlargement, but consistently overestimated the rate of headcut progression relative to field observations. In the untreated cases, erosion initiated between approximately 25 and 30 hours, whereas the best-fit simulations delayed initiation to about 33 hours by adjusting VCF, RCI, and τ_c. Headcut advance remained too rapid in all cases, with simulated headcut migration typically occurring 3 to 5 times faster than observed, indicating that calibration could improve timing of onset and breach geometry but could not fully correct the model's staged-process representation of erosion.

The best-fit simulations achieved reasonable agreement with observed breach widths and depths after reducing k_d up to 58% relative to lab-observed values and decreasing AC by up to 95%, but these improvements came at the cost of pushing some parameter values into physically unrealistic ranges. In particular, the very low AC values required to match the observations suggest that the model was compensating for structural limitations in its representation of erosion progression rather than fully capturing the underlying process. Differences between the untreated and treated parameter adjustments also highlighted the model's sensitivity to the assumed flow partitioning between embankment halves, particularly since the simplified half-flow approach could not account for the likely redistribution of overtopping discharge in the experiment. Taken together, the overtopping-plus-breach simulation results show that calibration could improve agreement with selected metrics, but it cannot resolve the fundamental mismatch between the modeled erosion sequence and the experimental breach behavior.

4.6 Breland et al. (2025) – Simulated Breach Progression Comparison

Figure 84 presents the final percent-error summary for headcut and breach width under untreated and treated conditions. The four lines correspond to the untreated headcut, the treated headcut, the untreated breach width, and the treated breach width, respectively. The y-axis shows percent error relative to observed final values, with 0%

indicating exact agreement, positive values indicating overprediction, and negative values indicating underprediction.

Comparisons were restricted to the correlated and best-fit parameter sets because the laboratory-derived erodibility parameters were judged to be less representative of the breach erosion behavior observed in the Breland simulations. Within this subset, the “blind” cases reflect predictive simulations conducted with limited prior knowledge and engineering judgment, while the overtopping-plus-breach cases reflect simulations informed by the broader experimental conditions and end-state behavior. Consequently, the blind and overtopping-plus-breach, correlated and best-fit, simulations give a sense of how well the models can project erosion progression under pre-test uncertainty and under more complete experimental guidance, respectively.

Across both embankment conditions, the plot confirms that headcut progression is the more challenging response to reproduce, with all scenarios overpredicting the final headcut position. As previously discussed, this is due to the headcut progression built into WinDAM C, which starts at the downstream crest. Observations from the Breland et al. (2025) experiments showed that the headcut initiated on the face or at the downstream toe and did not progress as far as the simulations indicated. This difference in mechanisms cannot be reconciled through parameter adjustments. DLBreach does not explicitly output the headcut position, but the extracted values, based on the other outputs, similarly show very rapid progression.

In contrast, breach width is closer to observations, with some simulations overpredicting and some underpredicting the final width. For the untreated embankment, all simulations except the blind-correlated WinDAM C stress model overpredict breach width. The treated embankment follows the same general pattern: the blind-correlated WinDAM C stress model underpredicts breach width, whereas the remaining simulations tend to overpredict it. While the direction of error is predominantly positive, the width predictions are closer than headcut. Overall, the results support the broader interpretation that calibration can improve aspects of the final breach response, but they do not fully resolve fundamental assumptions in the models.

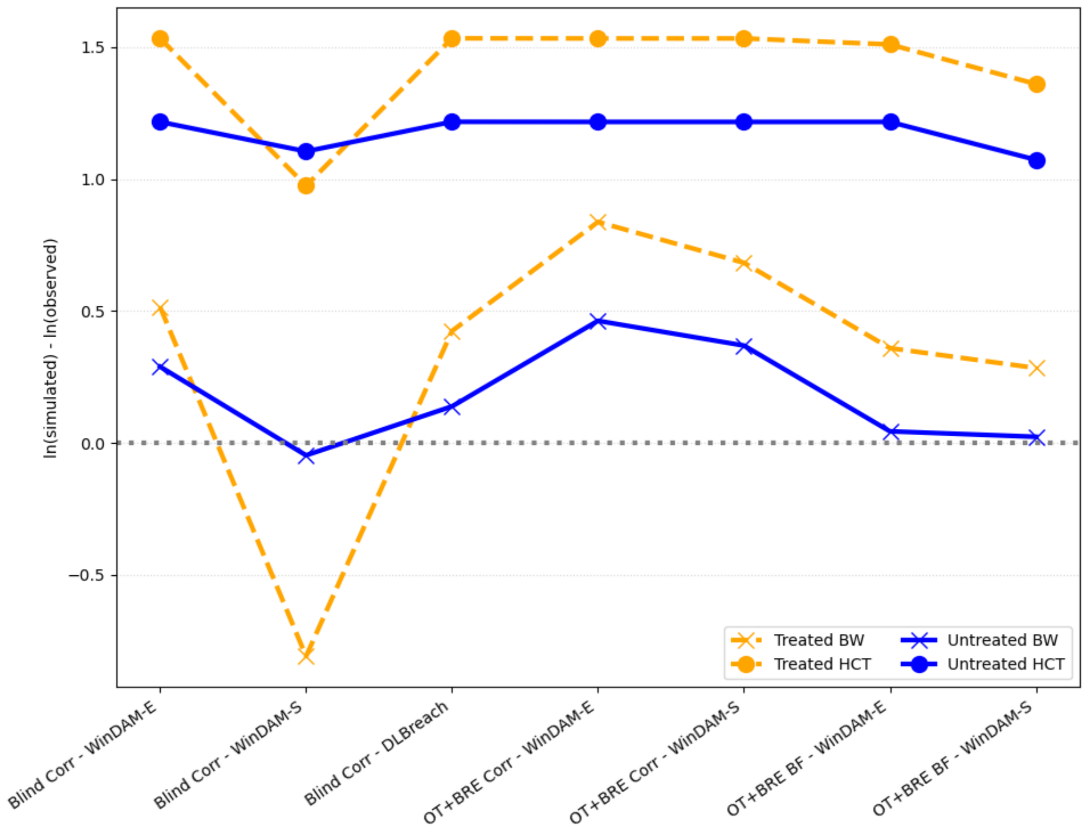

Figure 84. Final log-residual summary of simulated headcut progression and breach width for untreated and biopolymer-treated embankments across the correlated and best-fit simulation cases.

4.7 Sensitivity Analysis Using Dakota

Sensitivity analyses using Dakota were used to examine which model outputs were most strongly influenced by the input parameters. Pearson and Spearman correlation matrices (Table 10 and Table 11) were used to evaluate the relationships between model inputs and output responses. The heatmap in Figure 85 and lollipop charts in Figure 86 were then used to illustrate the relative change in each output between the lowest and highest tested values of each input parameter. As a result, the correlation matrices provide a measure of the overall linear and nonlinear association between inputs and outputs across all simulation runs, whereas the heatmap and lollipop charts emphasize low-versus-high sensitivity rather than full-range correlation.

Table 10. Linear correlation matrix between each model's input parameters and output response, with positive values indicating a direct relationship and negative values indicating an inverse relationship.

Model	Input Parameter	Final Breach Width	Final Hydraulic Control Elevation	Final Headcut Station
WinDAM C Energy	k_d	0.780	-0.605	-0.608
	τ_c	-0.028	0.019	0.025
	n	0.000	0.000	0.000
	AC	0.839	-0.889	-0.913
WinDAM C Stress	k_d	0.991	-0.752	-0.786
	τ_c	-0.307	0.151	0.134
	s_u	-0.423	0.593	0.643
	n	0.000	0.000	0.000
	γ_T	0.026	-0.082	-0.098
DLBreach	k_d	0.561	-0.160	0.000
	τ_c	-0.024	0.022	0.000
	n	0.909	-0.549	0.000
	K_h	-0.255	0.370	0.000

Note: Zero correlation indicates that all simulation runs advance across the full crest/embankment length, resulting in the same final value regardless of the input parameter values.

Table 11. Non-linear correlation matrix between each model's input parameters and output response, with positive values indicating a direct relationship and negative values indicating an inverse relationship.

Model	Input Parameter	Final Breach Width	Final Hydraulic Control Elevation	Final Headcut Station
WinDAM C Energy	k_d	0.766	-0.811	-0.706
	τ_c	-0.058	0.060	0.070
	n	0.000	0.000	0.000
	AC	0.874	-0.919	-0.915
WinDAM C Stress	k_d	0.986	-0.880	-0.972
	τ_c	-0.563	0.203	0.343
	s_u	-0.065	0.570	0.847
	n	0.000	0.000	0.000
	γ_T	-0.024	-0.087	-0.177
DLBreach	k_d	0.640	-0.177	0.000
	τ_c	-0.031	0.012	0.000
	n	0.911	-0.629	0.000
	K_h	-0.200	0.283	0.000

Note: Zero correlation indicates that all simulation runs advance across the full crest/embankment length, resulting in the same final value regardless of the input parameter values.

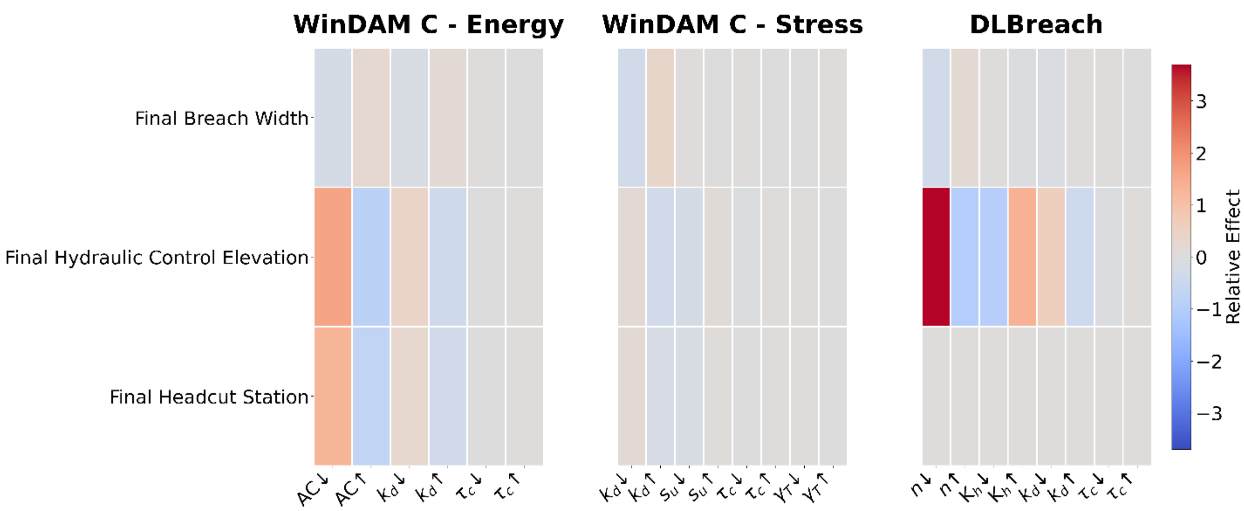

Figure 85. Heatmap of relative parameter sensitivity effects from the Dakota sensitivity analysis for the WinDAM C energy-based model, WinDAM C stress-based model, and DLBreach model, showing the relative response changes in breach metrics between the minimum and maximum tested parameter values.

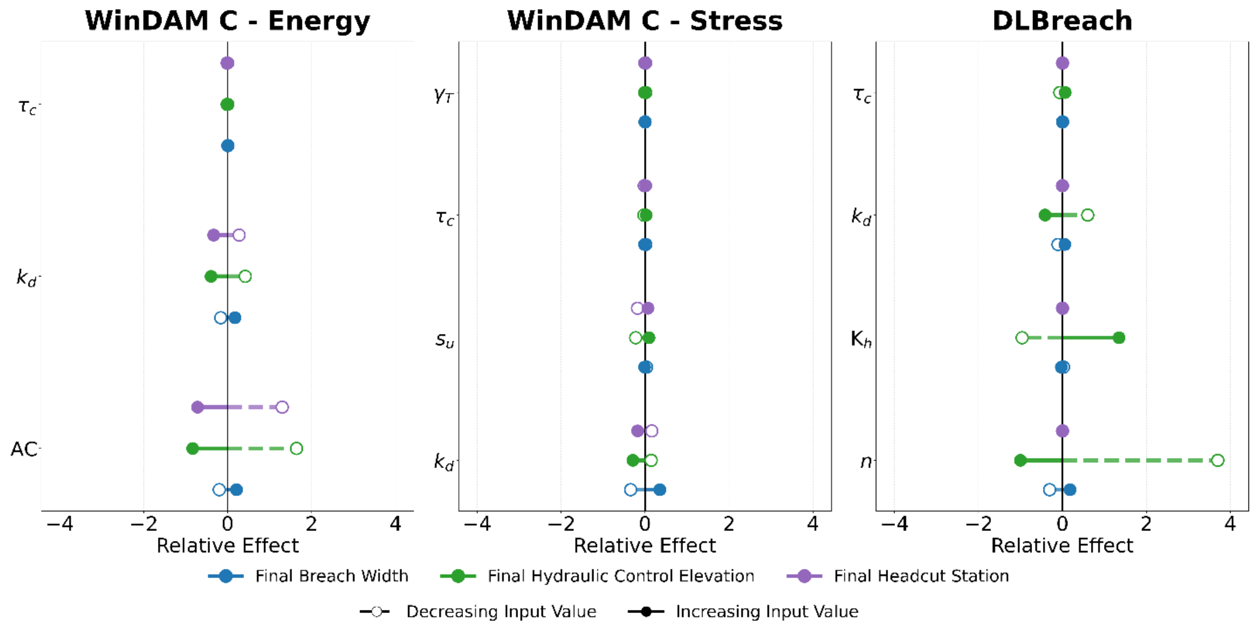

Figure 86. Lollipop plots of relative parameter sensitivity effects from the Dakota sensitivity analysis for the WinDAM C energy-based model, WinDAM C stress-based model, and DLBreach model, illustrating the magnitude and direction of output response changes associated with increasing and decreasing input parameter values.

For the WinDAM C energy-based model, AC showed positive correlation with final breach width and the strongest negative correlations with hydraulic control elevation and headcut distance, indicating that increases in AC were associated with wider breaches, lower final controlling elevations, and shorter headcut stations (Table 10; Table 11; Figure 85; Figure 86). k_d also showed a positive relationship with breach width and negative relationships with the other two responses, although its influence was weaker than AC's. τ_c had near-zero correlations with all outputs, suggesting little sensitivity to this input over the tested range.

In the WinDAM C stress-based model, k_d was the dominant parameter, showing the strongest positive correlation with final breach width and negative correlations with hydraulic control elevation and headcut station. The parameter s_u showed an inverse relationship with breach width and positive relationships with the other two responses, indicating that higher undrained shear strength tended to reduce breach enlargement while increasing the final elevations and headcut station metrics. By contrast, γ_T remained weakly correlated with all outputs, implying limited practical influence in this analysis.

For the DLBreach model, Manning's n produced the largest range of relative effects on final breach width and final hydraulic elevation. Additionally, K_h shows a notable effect on final hydraulic control elevation, whereas k_d shows smaller relative effects on hydraulic control and breach width. These visual measures identify n and K_h as the primary drivers of net change across the tested parameter ranges for DLBreach. Although the correlation matrices report only moderate coefficients for some of these parameters, the graphical results confirm that large net output changes occur between minimum and maximum parameter values and so should inform calibration priorities and uncertainty-reduction efforts for the DLBreach model.

4.8 Summary

This chapter presented simulation results from WinDAM C (energy- and stress-based) and DLBreach for the Kang et al. (2021) and Breland et al. (2025) overtopping experiments, covering both untreated and biopolymer-treated embankment conditions. Across all models and parameter sets, biopolymer treatment consistently delayed erosion initiation and reduced breach progression relative to untreated cases, though representing this behavior numerically required careful parameter adjustment through depth-weighted averaging and calibration. The final breach width was reproduced with reasonable accuracy in most calibrated simulations, whereas headcut migration and erosion timing were systematically overpredicted. The WinDAM C energy-based model showed the greatest difficulty, and DLBreach was limited by its inability to account for vegetation-controlled initiation. Dakota sensitivity analysis identified AC as the dominant parameter in the energy-based model, k_d in the stress-based model, and Manning's n in DLBreach, providing a clear hierarchy of parameter influence across all three modeling frameworks.

CHAPTER 5: Discussion

5.1 Parameter Selection and Calibration

This study tested whether existing overtopping breach models can represent the effects of biopolymer treatment on earthen embankment erosion and breach development. The experiments on treated embankments consistently showed delayed initiation and slower erosion than on untreated embankments, confirming that biopolymer stabilization improved near-surface erosion resistance in both field experiments. Overall, the results show that the models can capture some important aspects of the treated embankment response, especially final breach width in several cases, but they are not consistently able to reproduce the full sequence of overtopping failure, and they did a poor job of capturing the rate of headcut migration. The models generally required careful parameter adjustment to reflect that improvement and, even then, tended to overpredict the speed or severity of breach development.

A key finding is that the models reproduced end-state geometry better than transient erosion behavior. In other words, the final breach width was often matched reasonably well after calibration, but the rate and heterogeneous nature of the observed progression remained poorly represented. This distinction matters because two simulations may end with similar breach widths while following very different erosion pathways, which weakens confidence in the model's physics even when the final outputs appear acceptable. That pattern was especially clear in the Breland et al. cases, where some runs matched final width yet still overpredicted headcut distance and deepening by large margins.

5.2 Simulation Results

The models were validated by comparing predicted temporal and geometric breach responses against experimental observations, with emphasis on surface loss, upstream water level, headcut position, breach width, and breach bottom elevation. Across Breland et al. (2025) cases, blind-prediction simulations evaluated the overtopping phase, breach-only cases evaluated the breach phase, and combined simulations assessed the full sequence of overtopping and breach development. Because the Breland experiment was conducted over multiple days with intermittent daily overtopping periods, the observed water surface oscillations reflected the experimental test schedule rather than a continuous single-event hydrograph. The simulations, therefore, used the same intermittent forcing pattern to preserve the experimental timing structure.

Among the three models, the WinDAM C energy model required the most adjustment and was generally the least reliable predictor of erosion progression. It performed well in one untreated Kang et al. case, but that appears to be an isolated success rather than a generally robust behavior. The WinDAM C stress model and DLBreach were more consistent in reproducing final width and selected geometry outputs after calibration, but both still showed major errors in headcut-related metrics. DLBreach also has an important structural limitation: it does not explicitly represent vegetation-controlled initiation timing, which makes it less suitable for the Breland overtopping-plus-breach cases in which vegetation resistance was part of the observed response.

The treated embankments were harder to simulate than the untreated cases because the available breach tools were not designed to explicitly model a thin, strengthened surface layer over a weaker underlying soil. The depth-weighted averaging approach was a practical approximation, but it necessarily smoothed the vertical heterogeneity that likely controlled early headcut behavior. That helps explain why the treated simulations often showed larger scatter and why the models could match one aspect of the response, such as width, while missing another, such as headcut. In that sense, the difficulty in simulating the treated cases is not simply a calibration issue; it is evidence that the current model structure is not yet well-suited to layered biopolymer-treated embankments.

While the models generally reproduce the overall trend and can be calibrated to match a selected final metric (for example, final breach width), they consistently misrepresent the intermediate erosion sequence and phase transitions. These inconsistent responses are governed by structural process representations rather than by a single tunable parameter. In practice, calibration improved end-state agreement through parameter adjustments, but such adjustments sometimes moved parameters into ranges that are difficult to justify physically. Consequently, improved agreement on one output does not guarantee correct process representation across other outputs. Overall, agreement with observed breach behavior depended not only on parameter selection but also on the extent to which the model assumptions aligned with the experimental phase transitions, indicating that the primary limitation was structural representation of the breach process rather than numerical calibration alone.

5.3 Sensitivity Analysis

The Dakota sensitivity analysis reinforces this interpretation by showing that the dominant controlling parameters varied across models and output metrics. In the WinDAM C energy-based model, AC was the strongest control on the Final Headcut Station, indicating that headcut advance was primarily governed by the energy-based erosion formulation. In the WinDAM C stress-based model, k_d was the dominant parameter for Final Breach Width, indicating that breach widening was most sensitive to soil erodibility. For DLBreach, Manning's n was the strongest control on Final Breach Width, suggesting that hydraulic resistance had the greatest influence on the modeled breach geometry. Pearson and Spearman correlations were generally consistent in identifying these dominant trends, which indicates that the relationships were not artifacts of a single correlation measure. However, the relative strength of the correlations also indicated that some parameter effects were more linear, while others were better represented by nonlinear functions. This difference is important because it shows that each model emphasizes a different set of physical assumptions, so the parameters that control breach progression in one framework do not necessarily have the same influence in the other.

The sensitivity results also show that model calibration is not just a matter of fitting a single number; it is a means of compensating for different structural assumptions. In the energy model, AC was often adjusted substantially to match the treated case, and the implied parameter changes suggested that AC was absorbing processes not explicitly represented in the formulation. In the stress model, k_d had the greatest effect on the response, so changes in k_d had a much larger effect on width, headcut distance, and hydraulic control than the other inputs. Same in DLBreach, Manning's n dominated the response, meaning that roughness and flow resistance controlled much of the simulated behavior, while other inputs played secondary roles. This hierarchy helps explain why the same treated embankment could be approximated in more than one way, with different degrees of physical credibility.

5.4 Implications for Biopolymer-Treated Embankments

The Breland simulations add an especially useful methodological lesson. Having more observed information did not automatically produce better predictions when the model structure could not represent the governing processes. In some cases, the blind prediction was closer to the observed behavior than the more data-rich breach-only or combined cases, which suggests that model sensitivity and structural assumptions can dominate over the amount of input data. The fixed split-flow assumption between treated and untreated halves also introduced unavoidable uncertainty, because the untreated side likely experienced greater discharge as erosion progressed, yet the simulations held the inflow partition constant. That makes the Breland comparison valuable for showing that realistic boundary conditions and evolving flow partitioning matter as much as local soil parameters when predicting breach evolution.

Taken together, the experiments support the interpretation that biopolymer treatment strengthens the near-surface soil structure, reduces detachment, and slows breach development, but that effect is not represented by a single simple parameter in the models. The models can represent that improvement only approximately, mainly through adjusted soil and vegetation parameters rather than a direct mechanism for the biopolymer-soil system. The broader contribution of this work is therefore not only that it tests whether treated embankments can be modeled, but also that it identifies where existing overtopping breach tools fail to capture the treated response. Final breach width appears to be the most defensible output for practical prediction, while headcut migration and initiation timing remain highly uncertain and should be interpreted cautiously.

CHAPTER 6

Conclusions and Recommendations

This thesis investigated overtopping-induced breach development in cohesive earthen embankments treated with biopolymer amendment, with the goal of improving the ability to model and interpret erosion behavior in embankment dam design. The study was built around two full-scale experimental datasets, including the Kang et al. (2021) overtopping test and the ERDC Breland et al. experiment, and used two physically based breach models, WinDAM C and DLBreach, to simulate treated and untreated responses under overtopping conditions. The work also incorporated laboratory and field-based soil characterization, including erosion and strength relationships used to estimate model inputs such as erodibility, shear resistance, and related hydraulic parameters. In addition, a Dakota sensitivity framework was used to evaluate how uncertainty in key inputs influenced predicted breach behavior across the three model formulations.

6.1 Summary

Chapter 2 reviewed the background and literature relevant to overtopping erosion of earthen embankments, with particular attention to cohesive soil behavior, headcut migration, and available mitigation approaches. The review showed that overtopping failure is a progressive process controlled by both hydraulic forcing and soil resistance, and that cohesive erosion is strongly influenced by erodibility, critical shear stress, soil structure, vegetation, and consolidation state. The chapter also highlighted the growing interest in biopolymer stabilization as an erosion-reduction strategy, but it identified a lack of established methods for incorporating biopolymer effects into current breach prediction tools. These findings provided the basis for the modeling work carried out in the remainder of the thesis.

Chapter 3 described the modeling framework used to simulate the Kang et al. and Breland et al. overtopping experiments with WinDAM C and DLBreach. The chapter explained how each model was configured, what parameters were used, and how key soil, hydraulic, and vegetation inputs were selected or estimated when direct measurements were unavailable. It also described the calculation procedures used to derive important model parameters, such as AC, k_d, τ_c, and related soil resistance terms, as well as the Dakota sensitivity framework used later in the study. Overall, this chapter established the methodology for comparing each model's ability to reproduce observed breach development under both untreated and biopolymer-treated conditions.

Chapter 4 presented the simulation results for the Kang et al. and Breland et al. cases. In general, the simulations reproduced the broad sequence of erosion and breach formation, but the level of agreement varied across models, treatments, and response variables. The stress-based WinDAM C formulation generally performed better than the energy-based formulation, while DLBreach often provided reasonable comparisons for breach evolution but did not capture vegetation effects. Across simulations, the models tended to overpredict the rates of headcut progression and breach widening, although best-fit calibration improved agreement for selected outputs, such as breach width and erosion onset timing. The Breland et al. combined overtopping-plus-breach simulations showed that calibration could improve selected metrics, but it could not fully overcome the models' limitations in representing the observed progression of erosion.

Chapter 5 interpreted the simulation results and the Dakota sensitivity analysis in terms of model behavior and physical meaning. The sensitivity analysis showed that the controlling parameters differed by model, with AC governing Final Headcut Station in the WinDAM C energy model, k_d controlling Final Breach Width in the WinDAM C stress model, and Manning's n controlling Final Breach Width in DLBreach. These results demonstrated that each model responds most strongly to a different set of physical assumptions, which helps explain why the same embankment conditions did not produce identical results across programs. The chapter also showed that Pearson and Spearman correlations were generally consistent, but that some relationships were more linear than others, reinforcing the idea that model structure plays a major role in determining sensitivity and prediction accuracy.

6.2 Conclusions

The experimental results showed that biopolymer treatment improved erosion resistance by delaying initiation and slowing breach progression in both field datasets. In the Kang et al. case, treated embankments required more time to reach significant surface loss at a given overflow discharge, while the Breland et al. case also showed delayed and altered erosion behavior, though the response was more complicated due to vegetation, moisture variation, and split-embankment flow conditions. These findings confirm that biopolymer treatment strengthens near-surface soil structure and reduces detachment, but the effect is not represented by a single simple mechanism in the breach models.

The results showed that both WinDAM C and DLBreach reproduce some aspects of the observed behavior, especially the final breach width in selected cases, but neither consistently captured the full failure sequence with equal accuracy. Headcut migration was the weakest part of the predictions, particularly in treated embankments, where the near-surface response was more complex than the models could represent directly. This indicates that the current model formulations are useful for approximating end-state breach geometry, but they remain limited in their ability to represent the full temporal evolution of overtopping failure.

The results indicate that model behavior was strongly influenced by simplifying assumptions regarding embankment properties, surface treatment representation, and breach-process formulation. While calibration often improved agreement with the final breach width, especially in the untreated cases, this improvement did not always extend to the timing or sequence of breach-phase transitions. The WinDAM C stress-based model and DLBreach generally achieved reasonable agreement through physically defensible parameter adjustments, whereas the WinDAM C energy-based model sometimes required calibration to parameter values that were difficult to justify physically. These trends suggest that current breach models can reproduce selected end-state metrics, but their ability to capture the full progression of initiation, headcut migration, and lateral expansion remains limited by structural assumptions in the models themselves rather than by parameter tuning alone.

The sensitivity analysis showed that the dominant parameter changed by model: AC was most influential in the WinDAM C energy model, k_d was most influential in the WinDAM C stress model, and Manning's n was most influential in DLBreach. Pearson and Spearman results generally agreed, showing that the strongest relationships were consistently captured, while indicating that some inputs had more linear effects and others had more nonlinear effects. This model dependence means that uncertainty reduction and calibration must be tailored to the specific modeling framework, rather than assuming the same parameter priorities apply across all breach models.

6.3 Recommendations for Future Work

Based on the results of this study, future work should focus on improving how breach models represent biopolymer-treated embankments and on collecting the parameter data needed to reduce uncertainty in the most influential model inputs.

- Develop a layered soil representation that can distinguish a thin biopolymer surface zone from the underlying untreated embankment material.
- Improve headcut migration formulations so progression can be represented more realistically.
- Add or define vegetation and initiation timing effects in models used for treated embankments.
- Use targeted field and laboratory testing to better constrain the dominant parameters identified by sensitivity analysis, especially AC for the energy model, k_d for the stress model, and Manning's n for DLBreach.
- Expand future experiments to include additional treated embankment configurations, soil types, and biopolymer application depths or concentrations.
- Use final breach width as the most defensible model output for current applications but treat initiation timing and headcut-related metrics as highly uncertain until model structure improves.

REFERENCES

Abdel-Rahman, N. M. (1963). "The effect of flowing water on cohesive beds."

Abt, S. R., and Johnson, T. L. (1991). "RIPRAP DESIGN FOR OVERTOPPING FLOW." *J. Hydraul. Eng.*, 117 (8): 959–972.

Adams, B. M., Bohnhoff, W. J., Dalbey, K. R., Eddy, J. P., Eldred, M. S., Gay, D. M., Haskell, K., Hough, P. D., and Swiler, L. P. (2009). *Dakota, A multilevel parallel object-oriented framework for design optimization, parameter estimation, uncertainty quantification, and sensitivity analysis: Version 5.1 developers manual.* Sandia Tech. Rep. SAND2010-2185, Sandia Natl. Labs., Albuquerque, NM.

Adams, B. M., Bohnhoff, W. J., Dalbey, K. R., Ebeida, M. S., Eddy, J. P., Eldred, M. S., Hooper, R. W., Hough, P. D., Hu, K. T., Jakeman, J. D., Khalil, M., Maupin, K. A., Monschke, J. A., Ridgway, E. M., Rushdi, A. A., Seidl, D. T., Stephens, J. A., Swiler, L. P., and Winokur, J. G. (2022). *Dakota, A multilevel parallel object-oriented framework for design optimization, parameter estimation, uncertainty quantification, and sensitivity analysis: Version 6.16 user's manual.* Sandia Tech. Rep. SAND2022-6171, Sandia Natl. Labs., Albuquerque, NM.

Alcrudo, F., and Mulet, J. (2007). "Description of the Tous dam break case study (Spain)." *J. Hydraul. Res.* 45(1), 127–137.

Ali, T., and Setia, B. (2015). "Mechanism of erosion of cohesive sediment: A review." *J. Civ. Eng. Environ. Technol.* 2(2), 139–142.

Allen, P. M., Arnold, J. G., Auguste, L., White, J., and Dunbar, J. (2018). “Application of a simple headcut advance model for gullies.” *Earth Surface Processes and Landforms*, 43 (1): 202–217. John Wiley and Sons Ltd.

Amaral, S., Caldeira, L., Viseu, T., and Ferreira, R. M. L. (2020). “Designing experiments to study dam breach hydraulic phenomena.” *J. Hydraul. Res.* 146(4), 04020014.

Amos, C. L., Li, M. Z., and Sutherland, T. F. (1998). “The contribution of ballistic momentum flux to the erosion of cohesive beds by flowing water.” *J. Coast. Res.* 14(2), 564–569.

Amos, C. L., Droppo, I. G., Gomez, E. A., and Murphy, T. P. (2003). “The stability of a remediated bed in Hamilton Harbor, Lake Ontario, Canada.” *Sedimentology* 50(1), 149–168.

Arcement, G. J., and Schneider, V. R. (1989). *Guide for selecting Manning’s roughness coefficients for natural channels and flood plains.* U.S. Geol. Surv. Water-Supply Pap. 2339, U.S. Dept. of the Interior, Reston, VA.

Argüelles, C. A., Foppiani, N., and Hostert, M. (2023). “Efficiently exploring multidimensional parameter spaces beyond the Standard Model.” *Phys. Rev. D* 107(3), 035027.

Arulanandan, K., Gillogly, E., and Tully, R. (1980). *Development of a quantitative method to predict critical shear stress and erosion of natural undisturbed cohesive soils.* Tech. Rep. GL-805, U.S. Army Corps of Eng., Waterways Experiment Station, Vicksburg, MS.

ASTM International. (2016). *Standard test method for unconfined compressive strength of cohesive soil, ASTM D2166/D2166M-16.*

ASTM International. (2023). *Standard test methods for specific gravity of soil solids by the water displacement method, ASTM D854-23.*

Arabani, M., Shalchian, M., and Baghbani, A. (2024). “A state-of-the-art review on interactive mechanisms and multiscale application of biopolymers in geo-improvement and vegetation growth.” *J. Environ. Manage.* 358, 120905.

Ayeldeen, M., Negm, A., and El Sawwaf, M. (2016). “Evaluating the physical characteristics of biopolymer/soil mixtures.” *Arab. J. Geosci.* 9(5), 327.

Bach, E. (2021). “parasweep: A template-based utility for generating, dispatching, and post-processing of parameter sweeps.” *SoftwareX* 13, 100631.

Bagheri, P., Gratchev, I., Zolghadr, M., Son, S., and Kim, J. M. (2024). “Mitigation of soil erosion and enhancement of slope stability through the utilization of lignin biopolymer.” *Polymers* 16(9), 1300.

Bennett, S. J. (1999). “Effect of slope on the growth and migration of headcuts in rills.” *Geomorphology* 30(3–4), 273–290.

Bennett, S. J., and Casali, J. (2001). “Effect of initial step height on headcut development in upland concentrated flows.” *Water Resour. Res.* 37(6), 1475–1484.

Bennett, S. J., Alonso, C., Prasad, S., and Romkens, M. (2000). “A morphological study of headcut growth and migration in upland concentrated flows.” *Water Resour. Res.* 36(7), 1911–1922.

Bernhardt, M., Briaud, J.-L., Kim, D., Leclair, M., Storesund, R., Lim, S. G., Bea, R. G., and Rogers, J. D. (2011). “Mississippi River levee failures: June 2008 flood.” *Int. J. Geoeng. Case Histories* 2(3), 127–162.

Black, K. S., Tolhurst, T. J., Paterson, D. M., and Hagerthey, S. E. (2002). “Working with natural cohesive sediments.” *J. Hydraul. Eng.* 128(1), 2–8.

Bonilla, C., and Johnson, O. (2012). “Soil erodibility mapping and its correlation with soil properties in Central Chile.” *Geoderma* 189–190, 116–123.

Boudreau, B. P., and Jørgensen, B. B. (2000). *The benthic boundary layer: Transport processes and biogeochemistry.* Oxford Univ. Press, Oxford, UK.

Briaud, J.-L., Ting, F., Chen, H. C., Cao, Y., Han, S. W., and Kwak, K. W. (2001). “Erosion function apparatus for scour rate predictions.” *J. Geotech. Geoenviron. Eng.* 127(2), 105–113.

Calero, J., Ontiveros-Ortega, A., Aranda, V., and Plaza, I. (2017). “Humic acid adsorption and its role in colloidal-scale aggregation determined with the zeta potential, surface free energy and the extended-DLVO theory.” *Eur. J. Soil Sci.* 68(4), 491–503.

Casanova, H., Legrand, A., Zagorodnov, D., and Berman, F. (1999). “Heuristics for scheduling parameter sweep applications in grid environments.” Proc., 1999 ACM/IEEE Conf. on Supercomputing, San Diego, CA.

Çetin, M. Y., Bağrıaçık, B., Annagür, H. M., and Topoliński, S. (2024). “Improvement of geotechnical properties of clayey soil using biopolymer and ferrochromium slag additives.” *Polymers* 16(10), 1306.

Cestero, F. J. A., Imran, J., and Chaudhry, M. H. (2015). “Experimental investigation of the effects of soil properties on levee breach by overtopping.” *J. Hydraul. Eng.* 141(4), 04014085.

Chang, D. S., and Zhang, L. M. (2010). “Simulation of the erosion process of landslide dams due to overtopping considering variations in soil erodibility along depth.” *Nat. Hazards Earth Syst. Sci.* 10(4), 933–946.

Chang, I., Im, J., and Cho, G. (2016). “Geotechnical engineering behaviors of gellan gum biopolymer treated sand.” *Can. Geotech. J.* 53(10), 1658–1670.

Chang, I., Lee, M., Tran, A., Lee, S., Kwon, Y., Im, J., and Cho, G. (2020). “Review on biopolymer-based soil treatment (BPST) technology in geotechnical engineering practices.” *Transp. Geotech.* 24, 100385.

Chen, D., Wang, Y., Melville, B. W., Huang, H., and Zhang, W. (2018). “Unified formula for critical shear stress for erosion of sand, mud, and sand-mud mixtures.” *J. Hydraul. Eng.* 144(4), 04018008.

Chen, D., Zheng, J., Zhang, C., Guan, D., Li, Y., and Huang, H. (2022). “Threshold of surface erosion of cohesive sediments.” *Front. Mar. Sci.* 9, 847985.

Chenyi, M., Ming, P., Jiangtao, Y., Zhenming, S., and Limin, Z. (2025). “A breaching model for landslide dams involving size selective erosion and breach evolution.” *Engineering Geology*.

Cook, S., Timberlake, T., Murphy, D., and Stahl, J. (2015). “Selecting Dam Breach Inundation Software.” *The Journal of Dam Safety*, 13 (1): 41–52.

Cooper, C., Dewey, R., Fiedler, B., Frizell, K., Hepler, T., and Wahl, T. (2014). *Technical manual: Overtopping protection for dams.* FEMA Rep., Fed. Emergency Manage. Agency, Washington, DC.

Cubrinovski, M., and Ishihara, K. (1999). "Empirical correlation between SPT N-value and relative density for sandy soils." *Soils Found.* 39(5), 61–71.

Czapiga, M., Kotey, E., Elalfy, E., Nkiri, O., Viparelli, E., and Chaudhry, M. (2024). "Laboratory investigation on the breaching of biopolymer-treated dams and embankments." Proc., World Environ. Water Resour. Congr. 2024, ASCE, Reston, VA, 802–807.

di Nardi, J., Palermo, M., Pagliara, S., and Bombardelli, F. A. (2022). "Jet scour in cohesive and non-cohesive soil." Proc., 9th IAHR Int. Symp. on Hydraul. Struct., IAHR, 381–390.

de Baets, S., Denbigh, T. D. G., Smyth, K. M., Eldridge, B. M., Weldon, L., Higgins, B., Matyjaszkiewicz, A., Meersmans, J., Larson, E. R., Chenchiah, I. V., Liverpool, T. B., Quine, T. A., and Grierson, C. S. (2020). "Micro-scale interactions between Arabidopsis root hairs and soil particles influence soil erosion." *Commun. Biol.* 3(1), 186.

Dong, K., Li, Z., Lu, X., Chen, C., Sheng, J., Chen, J., and Wu, Z. (2021). "Analysis of dam overtopping failure risks caused by landslide-induced surges considering spatial variability of material parameters." *Front. Earth Sci.* 9, 675900.

De Ploey, J. (1989). "A model for headcut retreat in rills and gullies." *Catena* Suppl. 14, 81–86.

Dey, A. K., Tsujimoto, T., and Kitamuta, T. (2001). “Growth and migration of headcut in heterogeneous soil stratum.” Proc., Hydraul. Eng. 45(2), 823–828.

Evers, M., and Linsen, L. (2022). “Multi-dimensional parameter-space partitioning of spatio-temporal simulation ensembles.” *Comput. Graph.* 104, 140–151.

FEMA. (2012). *Assessing the consequences of dam failure.* M. P. P. Risk Assess., Ed., Fed. Emergency Manage. Agency, Washington, DC.

FERC. (2014). “Dam breach analysis.” *FERC engineering guidelines: Risk-informed decision making,* Fed. Energy Regul. Comm., Washington, DC.

Flores-Cervantes, J. H., Istanbulluoglu, E., and Bras, R. L. (2006). “Development of gullies on the landscape: A model of headcut retreat resulting from plunge pool erosion.” *J. Geophys. Res.* 111(F1), F01012.

Forsberg, P. L., Skinnebach, K. H., Becker, M., Ernstsen, V. B., Kroon, A., and Andersen, T. J. (2018). “The influence of aggregation on cohesive sediment erosion and settling.” *Cont. Shelf Res.* 171, 52–62.

Fread, D. L. (1988). *BREACH: An erosion model for earthen dam failures.* NWS Tech. Rep., Natl. Weather Serv., NOAA, Silver Spring, MD.

Frey, H. C., and Patil, S. R. (2002). “Identification and review of sensitivity analysis methods.” *Risk Anal.* 22(3), 553–578.

Froehlich, D. C. (2008). “Embankment Dam Breach Parameters and Their Uncertainties.” *Journal of Hydraulic Engineering*, (12): 1708–1721.

García-Asensio, J. M., and Ayuga, F. (2017). “Irrigation engineering in Spain and how it has changed the country’s landscapes.” *Eur. Countryside* 9(1), 211–229.

Grabowski, R. C., Droppo, I. G., and Wharton, G. (2011). “Erodibility of cohesive sediment: The importance of sediment properties.” *Earth-Sci. Rev.* 105(1–2), 101–120.

Guo, M., Wang, W., Shi, Q., Chen, T., Kang, H., and Li, J. (2019). “An experimental study on the effects of grass root density on gully headcut erosion in the gully region of China’s Loess Plateau.” *Land Degrad. Dev.* 30(15), 2107–2125.

Guo, M. M., Wang, W., Wang, T., Wang, W., and Kang, H. (2020). “Impacts of different vegetation restoration options on gully head soil resistance and soil erosion in loess tablelands.” *Earth Surf. Process. Landf.* 45(4), 1038–1050.

Guo, M., Chen, Z., Wang, W., Wang, T., Shi, Q., Kang, H., Zhao, M., and Feng, L. (2021). “Spatiotemporal changes in flow hydraulic characteristics and soil loss during gully headcut erosion under controlled conditions.” *Hydrol. Earth Syst. Sci.* 25(8), 4473–4494.

Gyssels, G., Poesen, J., Bochet, E., and Li, Y. (2005). “Impact of plant roots on the resistance of soils to erosion by water: A review.” *Prog. Phys. Geogr.* 29(2), 187–217.

Hansen, K. D., and Fitzgerald, T. J. (2016). “Performance of RCC used for overtopping protection and spillways.” *Dams Safety.* 30(1), 1–12.

Hanson, G. J., and Robinson, K. M. (1993). “The influence of soil moisture and compaction on spillway erosion.” *Trans. ASAE* 36(5), 1349–1352.

Hanson, G. J., Cook, K., and Hunt, S. (2005). “Physical modeling of overtopping erosion and breach formation of cohesive embankments.” *Trans. ASAE* 48(5), 1783–1794.

Hanson, G. J., and Hunt, S. L. (2007). “Lessons learned using laboratory jet method to measure soil erodibility of compaction soils.” *Appl. Eng. Agric.* 23(3), 305–312.

Hanson, G. J., Temple, D. M., Hunt, S. L., and Tejral, R. D. (2011). “Development and characterization of soil material parameters for embankment breach.” *Appl. Eng. Agric.* 27(4), 587–595.

Hepler, T., Fiedler, B., Vermeyen, T., Dewey, R., and Wahl, T. (2012). “Overtopping protection for dams – A technical manual overview.” *J. Dam Safety* 10(3), 1–14.

Hiller, P. (2017). *Riprap design on the downstream slopes of rockfill dams.* ICOLD Bull. 172, Int. Comm. on Large Dams, Paris.

Hu, F., Xu, C., Li, H., Li, S., Yu, Z., Li, Y., and He, X. (2015). “Particles interaction forces and their effects on soil aggregates breakdown.” *Soil Tillage Res.* 147, 1–9.

Huedo, E., Montero, R., and Llorente, I. M. (2004). “Experiences on adaptive grid scheduling of parameter sweep applications.” Proc., 12th Euromicro Conf. on Parallel, Distrib., and Network-Based Process., 222–229.

Hunt, S. L., Temple, D. M., Neilsen, M. L., Ali, A., and Tejral, R. D. (2021). “WinDAM C: Analysis tool for predicting breach erosion processes of embankment dams due to overtopping or internal erosion.” *Appl. Eng. Agric.* 37(3), 523–534.

Kamphuis, J. W., and Hall, K. (1983). “Cohesive material erosion by unidirectional current.” *J. Hydraul. Eng.* 109(1), 49–61.

Kang, W., Ko, D., and Kang, J. (2021). “Erosion resistance performance of surface-reinforced levees using novel biopolymers investigated via real-scale overtopping experiments.” *Water* 13(18), 2482.

Kulesza, S., and Karim, M. Z. (2021). *Critical shear stress of cohesive soils in Kansas.* KSU Transp. Res. Rep. KSU-18-5, Kansas Dept. of Transp., Topeka, KS.

Kumar, M. A., Moghal, A. A. B., Rasheed, R. M., and Rehman, A. U. (2025). "Enhancing durability and erosion resistance of soils with varying plasticity using crosslinked biopolymers." *Sci. Rep.* 15(1), 12572.

Kulesza, S. E., Mathis, M. A., Alarcon, V. J., and Sassenrath, G. F. (2024). "Critical shear stress variability in claypan soils with depth." *J. Soil Water Conserv.* 79(2), 66–77.

Kwon, Y., Ham, S., Kwon, T., Cho, G., and Chang, I. (2020). "Surface-erosion behaviour of biopolymer-treated soils assessed by EFA." *Géotech. Lett.* 10(2), 106–112.

Kwon, Y.-M., Lee, M., Chang, I., and Cho, G.-C. (2023a). "Biopolymers for erosion mitigation of soils observed by erosion function apparatus (EFA)." *Geo-Congr. 2023,* ASCE, Reston, VA, 462–469.

Kwon, Y., Moon, J., Cho, G., Kim, Y., and Chang, I. (2023b). "Xanthan gum biopolymer-based soil treatment as a construction material to mitigate internal erosion of earthen embankment: A field-scale study." *Constr. Build. Mater.* 389, 131716.

Larson, S., Corcoran, M. K., Gent, D. B., Butler, A. D., and Nestler, C. (2019). *Improved levee resilience through soil application of a natural organic polymer.* ERDC-TR-19-6, U.S. Army Engineer Res. and Dev. Ctr., Vicksburg, MS.

Leeder, M. R. (1999). *Sedimentology and sedimentary basins: From turbulence to tectonics.* Blackwell, Oxford, UK.

Li, S., Li, H., Xu, C.-Y., Huang, X.-R., Xie, D.-T., and Ni, J.-P. (2013). "Particle interaction forces induce soil particle transport during rainfall." *Soil Sci. Soc. Am. J.* 77(5), 1563–1571.

Li, Y., Zhang, C., Dai, W., Chen, D., Sui, T., Xie, M., and Chen, S. (2022). “Laboratory investigation on morphology response of submerged artificial sandbar and its impact on beach evolution under storm wave condition.” *Mar. Geol.* 443, 106668.

Liang, Y., Hilal, N., Langston, P., and Starov, V. (2007). “Interaction forces between colloidal particles in liquid: Theory and experiment.” *Adv. Colloid Interface Sci.* 134–135, 151–166.

Liu, W., Wang, B., and Guo, Y. (2021). “Numerical study of the dam-break waves and Favre waves down sloped wet rigid-bed at laboratory scale.” *J. Hydrol.* 602, 126752.

Low, P. F. (1987). “Structural component of the swelling pressure of clays.” *Langmuir* 3(1), 18–25.

Lucker, S., Walshire, L., Feng, K. C., Corcoran, M. K., and Larson, S. L. (2023). “Investigation of the biopolymer *Rhizobium tropici* for use in soil improvement.” *Geo-Congr. 2023,* ASCE, Reston, VA, 452–459.

Madsen, T. V., and Warncke, E. (1983). “Velocities of currents around and within submerged aquatic vegetation.” *Arch. Hydrobiol.* 97(3), 389–394.

Mashreghi, A., Elalfy, E., Goharian, E., and Chaudhry, M. H. (2025). “Laboratory modeling of biopolymer-treated embankment breach under overtopping.” *World Environ. Water Resour. Congr. 2025,* ASCE, Reston, VA.

Mehta, A. J., Hayter, E. J., Parker, W. R., Krone, R. B., and Teeter, A. M. (1989). “Cohesive sediment transport. I: Process description.” *J. Hydraul. Eng.* 115(8), 1076–1093.

Mehta, A. J., and Parchure, T. M. (2000). “Surface erosion of fine-grained sediment revisited.” In *Muddy coast dynamics and resource management,* B. W. Flemming, M. T. DeLaFontaine, and G. Liebezeit, eds., Elsevier, Oxford, UK, 55–74.

Moore, J. (1994). “Headcut advance threshold in earth spillways.” *Bull. Assoc. Eng. Geol.* 21(2), 277–280.

Moore, J. (1997). “Field procedures for the headcut erodibility index.” *Trans. ASAE* 40(2), 325–336.

Morán, R., Toledo, M. Á., and Caballero, F. J. (2026). *Overtopping Protection of Embankment Dams*. 1st ed. McGraw-Hill.

Morris, M. W., Kortenhaus, A., Visser, P. J., and Hassan, M. (2009). *Breaching processes: A state of the art review.* FLOODsite Rep. T06-06-03, FLOODsite Consortium, Wallingford, UK.

Mozer, A., Almström, B., Olsson, P. A., and Schüttrumpf, H. (2025). “Estimating erosion resistance of vegetated sea dike embankments through in situ experiments.” *Front. Built Environ.* 11, 1528863.

MDE. (2018). *Guidance for completing a dam breach analysis for small ponds and dams in Maryland.* Maryland Dept. of the Environ., Annapolis, MD.

Nazari Samani, A., Ahmadi, H., Mohammadi, A., Ghoddousi, J., Salajegheh, A., Boggs, G., and Pishyar, R. (2010). “Factors controlling gully advancement and models evaluation (Hableh Rood Basin, Iran).” *Water Resour. Manage.* 24(7), 1532–1549.

Neilsen, M. L., Kong, Q., Bulleigh, M., and Williams, G. (2015). “Coupled dam erosion analysis using DAKOTA and WinDAM.” Proc., Int. Conf. on Sci. Comput., 121–127.

Neilson, M., and Cao, C. (2019). *Sensitivity analysis of internal erosion models for dam safety.* Master's thesis, Kansas State Univ., Manhattan, KS.

Nepf, H. M., and Vivoni, E. R. (2000). "Flow structure in depth-limited, vegetated flow." *J. Geophys. Res. Oceans* 105(C12), 28547–28557.

Ni, J., Wang, Z.-T., and Geng, X. (2023). "Vegetation growth promotion and overall strength improvement using biopolymers in vegetated soils." *Can. Geotech. J.*, 10.1139/cgj-2022-0049.

Nicholson, J., and O'Connor, B. A. (1986). "Cohesive sediment transport model." *J. Hydraul. Eng.* 112(7), 621–639.

Nowell, A. R. M., and Jumars, P. A. (1984). "Flow environments of aquatic benthos." *Annu. Rev. Ecol. Syst.* 15, 303–328.

Owen, M. W. (1975). *"Erosion of Avonmouth mud."* Rep. No. INT 150, Hydraul. Res. Stn., Wallingford, UK.

Pearson, K. (1895). "Regression, heredity, and panmixia." *Philos. Trans. R. Soc. Lond. Ser. A* 186, 257–318.

Peck, R. B., Hanson, W. E., and Thornburn, T. H. (1974). *Foundation engineering.* 2nd Ed., Wiley, New York.

Peeters, P., van Hoestenberghe, T., Vincke, L., and Visser, P. (2011). "SWOT analysis of breach models for common dike failure mechanisms." *Engineers Australia*, 3936–3943. Brisbane, Australia.

Perkey, D. W., Smith, S. J., Fall, K. A., Massey, G. M., Friedrichs, C. T., and Hicks, E. M. (2020). “Impacts of muddy bed aggregates on sediment transport and management in the tidal James River, VA.” *J. Waterway Port Coastal Ocean Eng.* 146(5), 04020028.

Pianosi, F., Beven, K., Freer, J., Hall, J. W., Rougier, J., Stephenson, D. B., and Wagener, T. (2016). “Sensitivity analysis of environmental models: A systematic review with practical workflow.” *Environ. Model. Softw.* 79, 214–232.

Prasad, S. N., and Römkens, M. J. M. (2003). “Energy formulations of headcut dynamics.” *Catena* 50(2–4), 469–487.

Ralston, D. C. (1987). “Mechanisms of embankment erosion during overflow.” Proc., 1987 ASCE Nat. Conf. on Hydraul. Eng., 733–738.

Rasheed, R. M., Moghal, A. A. B., Rambabu, S., and Almajed, A. (2023). “Sustainable assessment and carbon footprint analysis of polysaccharide biopolymer-amended soft soil as an alternate material to canal lining.” *Front. Environ. Sci.* 11, 1214988.

Regazzoni, P. L., Hanson, G. J., Wahl, T., Marot, D., and Courivaud, J. R. (2008). “The influence of some engineering parameters on the erosion of soils.” Proc., 4th Int. Conf. on Scour and Erosion, Japanese Geotech. Soc., Tokyo, 541–546.

Rengers, F. K., and Tucker, G. E. (2014). “Analysis and modeling of gully headcut dynamics, North American high plains.” *Journal of Geophysical Research: Earth Surface*, 119 (5): 983–1003. Blackwell Publishing Ltd.

Righetti, M., and Lucarelli, C. (2007). “May the Shields theory be extended to cohesive and adhesive benthic sediments?” *J. Geophys. Res. Oceans* 112(C5), C05039.

Robinson, K. M. (1996). *Gully erosion and headcut advance.* Ph.D. thesis, Oklahoma State Univ., Stillwater, OK.

Rodgers, D., Watkins, C., and Chung, J.-W. (2010). “The 2005 Upper Taum Sauk dam failure: A case history.” *Environ. Eng. Geosci.* 16(3), 257–289.

Sacramento County. (2025). *Dam failure.* Sacramento County Flood Control and Water Conserv. Dist., Sacramento, CA.

Sanchis, M. P., Torri, D., Borselli, L., and Poesen, J. (2008). “Climate effects on soil erodibility.” *Earth Surf. Process. Landf.* 33(7), 1082–1097.

Sanford, L. P., and Maa, J. P.-Y. (2001). “A unified erosion formulation for fine sediments.” *Mar. Geol.* 179(1), 9–23.

Sanford, L. P. (2008). “Modeling dynamically varying mixed sediment beds with erosion, deposition, bioturbation, consolidation, and armoring.” *Comput. Geosci.* 34(10), 1263–1283.

Saltelli, A. (1999). “Sensitivity analysis. Could better methods be used?” *J. Geophys. Res. Atmos.* 104(D3), 3789–3793.

Saltelli, A., Tarantola, S., Campolongo, F., and Ratto, M. (2004). *Sensitivity analysis in practice: A guide to assessing scientific models.* Wiley, Chichester, UK.

Samples, M. E., Daida, J. M., Byom, M., and Pizzimenti, M. (2005). “Parameter sweeps for exploring GP parameters.” Proc., Genet. Evol. Comput. Conf., 212–219.

Shan, H., Shen, J., Kilgore, R., and Kerenyi, K. (2015). *Scour in cohesive soils.* Rep. No. FHWA-HRT-15-033, Fed. Highway Admin., McLean, VA.

Shan, Y., Zhong, Q., Chen, S., Wang, L., Chen, X., Mei, S., and Yang, M. (2023). “Experimental study on predicting head-cut migration rate of check dams.” *J. Hydrol.* 624, 129882.

Sharif, A. R. (2003). *Critical shear stress and erosion of cohesive soils.* Ph.D. thesis, State Univ. of New York at Buffalo, Buffalo, NY.

Sharma, R. P., Kumar, A., and Kumar, A. (2013). “Earthen dam failures.” Proc., Int. Conf. Case Hist. Geotech. Eng., Missouri Univ. Sci. Technol., Rolla, MO.

Smanchat, S., Indrawan, M., Ling, S., Enticott, C., and Abramson, D. (2013). “Scheduling parameter sweep workflow in the grid based on resource competition.” *Future Gener. Comput. Syst.* 29(5), 1164–1183.

Song, G., Zhao, T., Zhao, P., Fu, C., and Hu, X. (2024). “Simulation of landslide dam failure due to overtopping considering wide-graded soil erosion.” *Sci. Rep.* 14(1), 78649.

Song, X., Zhang, J., Zhan, C., Xuan, Y., Ye, M., and Xu, C. (2015). “Global sensitivity analysis in hydrological modeling: Review of concepts, methods, theoretical framework, and applications.” *J. Hydrol.* 523, 739–757.

Spearman, C. (1904). “The proof and measurement of the association between two things.” *Am. J. Psychol.* 15(1), 72–101.

Stein, O. R., and LaTray, D. A. (2002). “Experiments and modeling of head cut migration in stratified soils.” *Water Resour. Res.* 38(12), 20-1–20-12.

Stephens, T. (2010). *Manual on small earth dams.* Food and Agric. Org. of the U.N., Rome.

Sun, Y., Chang, H., Miao, Z., and Zhong, D. (2012). “Solution method of overtopping risk model for earth dams.” *Saf. Sci.* 50(9), 1906–1912.

Sunborg, A. (1956). “A study of fluvial processes.” *Geografiska Ann.* 38A(1–2), 18–42.

Temple, D. M. (1982). “Flow retardance of submerged grass channel linings.” *Trans. ASAE* 25(5), 1300–1303.

Temple, D. M., Robinson, K. M., Ahring, R. M., and Davis, A. G. (1987). *Stability design of grass-lined open channels.* USDA Agric. Handb. 667, U.S. Dept. of Agric., Washington, DC.

Temple, D. M. (1992). “Estimating flood damage to vegetated deep soil spillways.” *Appl. Eng. Agric.* 8(2), 237–242.

Temple, D. M., and Moore, J. (1994). “Headcut advance prediction for earth spillways.” *Trans. ASAE* 40(3), 557–562.

Temple, D. M., Hanson, G. J., Neilsen, M. L., and Cook, K. (2005). “Simplified breach analysis model for homogeneous embankments: Part 1, Background and model components.” Proc., 25th Annu. U.S. Soc. Dams Conf., 1–12.

Thomaz, E. L., Araujo-Junior, C. F., Vendrame, P. R. S., and de Melo, T. R. (2022). “Mechanisms of aggregate breakdown in (sub)tropical soils: Effects of the hierarchical resistance.” *Catena* 216, 106377.

Thomsen, L., and Gust, G. (2000). “Sediment erosion thresholds and characteristics of resuspended aggregates on the western European continental margin.” *Deep-Sea Res. Part I* 47(10), 1881–1897.

Thorn, M. F. C., and Parsons, J. G. (1980). “Erosion of cohesive sediments in estuaries: An engineering guide.” Proc., 3rd Int. Symp. on Dredging Technol., 349–358.

United States Army Corps of Engineers. (2004). *General design and construction considerations for earth and rock-fill dams.* U.S. Army Corps of Eng., Washington, DC.

U.S. Dept. of Agric., Nat. Resour. Conserv. Serv. (2001). *Chapter 52: Field procedures guide for the headcut erodibility index.* National Eng. Handb.

U.S. Dept. of Agric., Nat. Resour. Conserv. Serv. (2014). *Part 628: Dams national engineering handbook. Chapter 51: Earth spillway erosion model.* http://www.ascr.usda.gov.

U.S. Dept. of Agric., Nat. Resour. Conserv. Serv. (2021). *Chapter 9: Diversions.* Nat. Eng. Handb.

U.S. Dept. of the Interior. (2012). *Embankment design.* Reclam. Manage. Water in the West, 13th Ed., W. Engemoen, ed., U.S. Dept. of the Interior, Denver, CO.

Ursic, M., and Langendoen, E. (2021). *Comparison of test methods for erodibility of bank materials on the lower American and Sacramento Rivers, adjacent to the City of Sacramento, California.* U.S. Dept. of Agric., Nat. Resour. Conserv. Serv., Washington, DC.

Vanmaercke, M., Poesen, J., Mele, B. V., Demuzere, M., Bruynseels, A., Golosov, V., Bezerra, J. F. R., Bolysov, S., Dvinskih, A., Frankl, A., Fuseina, Y., Guerra, A. J. T., Haregeweyn, N., Ionita, I., Imwangana, F. M., Moeyersons, J., Moshe, I., Samani, A. N., Niacsu, L., Nyssen, J., Otsuki, Y., Radoane, M., Rysin, I., Ryzhov, Y. V., and Yermolaev, O. (2016). "How fast do gully headcuts retreat?" *Earth-Sci. Rev.* 154, 336–355.

Van Oss, C. J. (2006). *Interfacial forces in aqueous media.* 2nd Ed., CRC Press, Boca Raton, FL.

Visser, K., Wang, H., Hall, A., and Hudson, G. (2024). *WinDAM C software.* WinDAM Techn. Doc., U.S. Dept. of Agric., Nat. Resour. Conserv. Serv., Washington, DC.

Wahl, T. L. (1998). *Prediction of embankment dam breach parameters.* M.S. thesis, Utah State Univ., Logan, UT.

Wahl, T. L. (2001). "The uncertainty of embankment dam breach parameter predictions based on dam failure case studies." In *Issues, resolutions, and research needs related to dam failure analysis,* USDA/FEMA, Oklahoma City, OK, 1–12.

Wahl, T. L. (2016). *Embankment overtopping protection by riprap considering interstitial flow.* USBR Tech. Mem., U.S. Dept. of the Interior, Bureau of Reclamation, Denver, CO.

Walder, J. S., and J. E. O'Connor. (1997). "Methods for predicting peak discharge of floods caused by failure of natural and constructed earthen dams." *Water Resources Research*, 33 (10): 2337–2348.

Walshire, L., Breland, B., Vroman, T., and Larson, S. L. (2024). "Multiscale assessment of biopolymer soil amendment for earthen embankments." *J. Dam Safety* 21(4), 34–49.

Wang, S., Zhao, X., Zhang, J., Jiang, T., Wang, S., Zhao, J., and Meng, Z. (2023). "Water retention characteristics and vegetation growth of biopolymer-treated silt soils." *Soil Tillage Res.* 225, 105544.

West, M., Morris, M., and Hassan, M. (2018). *A guide to breach prediction.* Human Res. Prot. Program, HR Wallingford, Wallingford, UK.

Winterwerp, J. C., and van Kesteren, W. G. M. (2004). *Introduction to the physics of cohesive sediment in the marine environment.* Elsevier, Amsterdam, Netherlands.

Wu, W.-M., and Wang, S. S. Y. (2005). “Empirical-numerical analysis of headcut migration.” *Int. J. Sediment Res.* 20(3), 233–243.

Wu, W. (2011). “Earthen embankment breaching.” *J. Hydraul. Eng.* 137(12), 1549–1564.

Wu, W. (2013). “Simplified physically based model of earthen embankment breaching.” *J. Hydraul. Eng.* 139(8), 837–851.

Wu, W., and Perera, C. (2015). “Erosion of mixed cohesive and noncohesive sediments.” *J. Hydraul. Eng.* 141(8), 04015013.

Wu, W. (2016). *Introduction to DLBreach – A simplified physically-based dam/levee breach model.* Clarkson Univ., Potsdam, NY.

Xu, C.-Y., Yu, Z.-H., and Li, H. (2015). “The coupling effects of electric field and clay mineralogy on clay aggregate stability.” *J. Soils Sediments* 15(5), 1159–1168.

Yu, Z., Zhang, J., Zhang, C., Xin, X., and Li, H. (2017). “The coupling effects of soil organic matter and particle interaction forces on soil aggregate stability.” *Soil Tillage Res.* 174, 251–260.

Yu, Z., Zheng, Y., Zhang, J., Zhang, C., Ma, D., Chen, L., and Cai, T. (2020). “Importance of soil interparticle forces and organic matter for aggregate stability in a temperate soil and a subtropical soil.” *Geoderma* 362, 114088.

Zhao, G., Visser, P. J., Peeters, P., and Vrijling. H. K. (2012). “Prediction of Headcut Erosion Development on the Breach Slope.” In: *ICSE6*, 1257–1264. Paris.

Zhao, G., Visser, P. J., Peeters, P., and Vrijling, J. K. (2013). “Headcut migration prediction of the cohesive embankment breach.” *Eng. Geol.* 164, 18–25.

Zhao, G., Visser, P. J., Peeters, P., and Vrijling, J. K. (2015). “Hydrodynamic erosion in cohesive embankment breach.” Proc., 7th Int. Conf. Scour and Erosion, CRC Press, London, 441–445.

Zhang, B. J., Xiong, D. H., Zhang, G. H., Zhang, S., Wu, H., Yang, D., Xiao, L., Dong, Y. F., Su, Z. A., and Lu, X. N. (2018). “Impacts of headcut height on flow energy, sediment yield and surface landform during bank gully erosion processes in the Yuanmou Dry Hot Valley region, southwest China.” *Earth Surf. Process. Landf.* 43(11), 2271–2282.

Zhang, F., Jia, S., Zhou, X., Wang, L., and Zhu, Y. (2025). “Modeling flood and breach evolution of the landslide dam due to overtopping.” *J. Hydrol.* 647, 132303.

Zhang, J., Li, Y., Xuan, G., Wang, X., and Li, J. (2009). “Overtopping breaching of cohesive homogeneous earth dam with different cohesive strength.” *Sci. China, Ser. E* 52(10), 3024–3029.

Zhang, J., and Liu, J. (2023). “A review on soils treated with biopolymers based on unsaturated soil theory.” *Polymers* 15(22), 4431.

Zhou, S., Li, P., Zhang, X., Wang, Y., Yu, K., Shi, P., Xiao, L., Wang, T., and Chang, E. (2024). “Runoff and erosion reduction benefits of vegetation during natural succession on fallow grassland slopes.” *Sci. Total Environ.* 954, 176211.

Zhong, Q. M., Chen, S. S., Deng, Z., and Mei, S. A. (2019). “Prediction of overtopping-induced breach process of cohesive dams.” *J. Geotech. Geoenviron. Eng.* 145(5), 04019012.

Zhu, Y., Visser, P. J., and Vrijling, J. K. (2004). “Review on embankment dam breach modeling.” Proc., 4th Int. Conf. Dam Eng., 18–20 Oct., Nanjing, China.

Zhu, Y. H., Visser, P. J., and Vrijling, J. K. (2005). “A model for headcut erosion during embankment breaching.” Proc., 4th IAHR Symp. River Coastal and Estuar. Morphodyn., 1183–1190.

APPENDIX

(a)

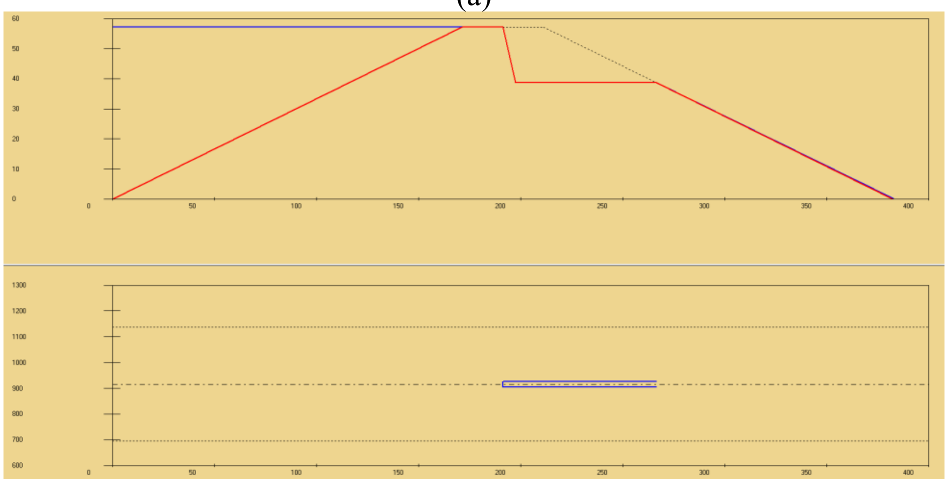

(b)

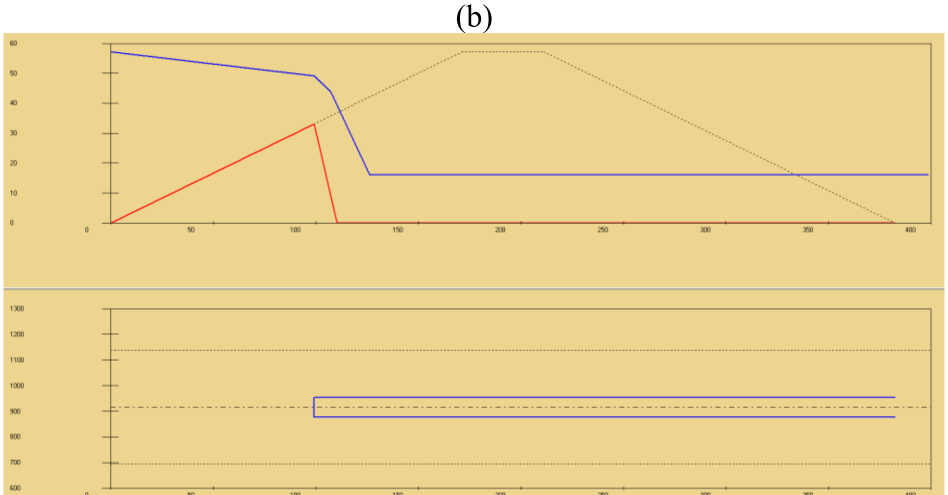

(c)

Figure 87. WinDAM C overtopping erosion progression: (a) erosion initiation starting with headcut advance, (b) headcut progression coincident with slight widening, (c) mature stage with headcut migration and gradual lateral expansion (blue = overtopping/widening, red = headcut, dashed = removed embankment).